MEASUREMENT OF THE MUONIC BRANCHING RATIO OF THE τ LEPTON USING THE OPAL DETECTOR AT LEP

David Alan Rigby

Thesis submitted for the degree of
Doctor of Philosophy

School of Physics and Space Research
Faculty of Science
University of Birmingham

December 1996

Synopsis

Using the data collected by the OPAL detector at LEP during 1991 - 1994 physics runs, a sample of $e^+e^- \rightarrow \mathrm{Z}^0 \rightarrow \tau^+\tau^-$ decays was isolated. Treating each year separately, further selections isolated samples of $\tau \rightarrow \mu\nu\bar{\nu}$ decays. The backgrounds of these selections, estimated initially from Monte Carlo, were checked using control samples formed from the data, and the efficiency of the $\tau \rightarrow \mu\nu\bar{\nu}$ selection was checked with an independent control sample of $\tau \rightarrow \mu\nu\bar{\nu}$ decays, taken from data and Monte Carlo. The overall muonic branching fraction was measured to be:

$$\begin{aligned} B(\tau \rightarrow \mu\nu\bar{\nu}) &= (17.453 \pm 0.121 \pm 0.039)\% \\ &= (17.453 \pm 0.127)\% \end{aligned}$$

where the first error derives from data-variables, and the second part of the error from all other sources. This result is consistent and very competitive with the results obtained by other collaborations, having one of the lowest systematic uncertainties. It is also in good agreement with the current World average value. This work has been released as an OPAL technical note [1] and will shortly be released as an OPAL physics note.

This branching ratio was then used to test lepton universality. The measured ratio for g_μ/g_e, obtained by comparing the muonic and electronic tau branching fractions, was found to be:

$$\left|\frac{g_\mu}{g_e}\right| = 1.0046 \pm 0.0059 \quad ,$$

which is clearly consistent with unity. Assuming lepton universality, a further calculation was made to determine an upper limit on the mass of the τ neutrino, which was found to be:

$$m_{\nu_\tau} < 130\mathrm{MeV/c^2} \quad , \quad \text{at } 95\% \text{ confidence level.}$$

Finally, the relation between the tau lifetime, tau mass, and tau branching ratio was tested by plotting the tau lifetime as a function of branching ratio and mass, and checking for consistency with the branching ratio measured in this analysis. The agreement was found to be very good.

These results serve to confirm Standard Model predictions, and are in agreement with other published results.

Acknowledgements

Right! Time for some acknowledgements then!

Let me first thank the staff at Brum for allowing me into the inner sanctum, and for giving me money and things - very much appreciated. Particular thanks to Alan Watson whose 'non-interference' method of supervision was, er, refreshing! Many thanks also to Pete Watkins, Dave Charlton, John Wilson and Hal Evans who helped a great deal to get this *beast* ship-shape.

Now to catalogue everyone I've ever known. Bear with me...

First of all my fellow Bham students: Paul Davies (cheers for the Welsh luurve spoon!), Scandie-man (still Scandying - give England another go sometime), Chris Dod (Personity Insanified - may your liver be forgiving), James (fellow purple-hater and web-meister), Andy Bayes, Steve Clewer, Jim Clayton, Keith Normal (cheers for the rug and cushions), Vicki (finish soon!), Tim, Neil (party!), Lee, Bellend (cpu-man), Scott..... then the CERN blokes: Ollie (Show young girls your large PUPPIES), Clive (no man is ruder), Jim (drink less *please*), Nick (I have to say it, 'The Prodder'), Gareth (M-hairs), Mike (cheers for the flat), Doug (Smokin' Joe)..... then grate mates from Oxford who helped me along the way: Poth (there is *only* one - never change), Clare (don't break him, there's only one remember), Chris (remain un'cided - and make more money!), Shaun (finish your PhD, stay in touch and leave Wales at some point), Gerard (cheers for web-photos, good luck with the PhD).......puis mes gentils amis de Genève: Chantal (thanks for all your generous help), Pascal & Aline (nice flat!), Carlos (my new 'twin' brother (I wish!)), Alexandre, Rosa and Dylan (super famille!)......and finally me mates from home: Pud (cheers for everything, nice to hit married life together! Congrat's to yourself and Justine for procreating Charlotte!), Jon (use that *force* wisely, Satan!), Alun (take care, you big bear!)...... I'd like to say that you were all absolutely smashing absolutely *all* of the time and there was never even a lull, not one; every moment sizzled and crackled with pulsing wonderfulness. I thank you.

Now to my families. Note the plural there, because last August I got married in Geneva! A beautiful Swiss/Spanish brunette called Marie-Josée consented to be my wife, and has ruthlessly trapped me in a prison of wedded bliss ever since. Joking aside, I love you very much indeed and still cannot quite believe my luck. I see a very bright future ahead of us...

I'd like to thank my new family, 'Les Fariñas' (José, Michèle, Annemarie, Carlos, Stéphanie, Christine and Fiona) for making me feel so very welcome and for all your kind generosity. Of course, enormous thanks must also go to my parents for their continued love, support and understanding - I couldn't have come this far without you, and you're more appreciated than you know. Also, since I'm trying quite shamelessly to squeeze in names here, a big hi to John, Susie and Heather, although I'm not sure when you'll get to read this exactly - stay in touch.

Well, that about wraps up this thinly-disguised cast list. The fact that I'm writing these acknowledgements means, I suppose, that I'm about to leave the cocoon of academia and try to make a life for myself *out there*. It's a fearsome cut-throat dog-eat-dog World and so I'd like to direct my final words to my future self. As you read this, David, no matter where you are or what you're doing, no matter how wretchedly awful things might seem to be, just mutter the word 'thesis' to yourself and all will seem much brighter.

David, 3rd December 1996, CERN.

Contents

List of Figures

List of Tables

Chapter 1

The Standard Model and the Tau Lepton

In persistent efforts to quench his thirst for knowledge, man has probed into space, into the oceans, and even into himself, but it is perhaps his studies into the realms of the very tiny that strike most clearly at the heart of this need to explain and rationalize physical phenomena. Particle physics is a relatively young branch of science, having only really begun in 1911 when Rutherford's alpha-particle-scattering experiment demonstrated that the neutral atoms of chemistry had a positively charged nucleus. Since then, our understanding of the subatomic world has increased enormously, culminating in a very successful set of theories known collectively as The Standard Model [2]. This chapter describes this Standard Model in some detail, and focuses particularly on the importance of tau physics in testing the current experimental boundaries.

1.1 The Standard Model

Within the Standard Model there are fermions which compose 'matter', and there are bosons which mediate the forces between particles. This appears to be all that is required to form the universe as we see it, although there are aspects of the theory that are not yet satisfactory. For instance, there are four recognized forces in nature, but only three have been incorporated into the quantum framework:

General Relativity will remain a 'classical' theory until the concept of space-time can be appreciated from a quantum mechanical standpoint. However, for experimental particle physics the effects of gravity can be safely neglected, since the gravitational interaction for such small masses is negligible compared with the magnitude of the other forces involved.

1.1.1 The Elementary Fermions

Fermions are particles with half integral spin ($\frac{1}{2}\hbar$, $\frac{3}{2}\hbar$, etc). Spin $\frac{1}{2}$ for instance, means that the particle has an intrinsic angular momentum of magnitude $S = \sqrt{\frac{1}{2}(\frac{1}{2}+1)}\hbar$ and can exist in only two states with angular momentum component, $S_z = \pm\frac{1}{2}\hbar$. These point-like elementary fermions are divided into two types called quarks and leptons. There are six *flavours* of quark, three with charge $+\frac{2}{3}$e (up (u), charm (c) and top (t)) and three with charge $-\frac{1}{3}$e (down (d), strange (s) and bottom (b)). The leptons also come in six flavours, three having one unit of electrical charge (e^-, μ^- and τ^-) and three which are electrically neutral, (ν_e, ν_μ and ν_τ). There is slightly more multiplicity than this however. Each of the quarks and leptons mentioned have *anti*-particles, denoted by $\bar{q}$ or $\bar{l}$, and the quarks also have a *'colour'* charge which might be red (or anti-red), blue (or anti-blue) or green (or anti-green). This colour-assignment, which is the basis of a gauge invariant theory called Quantum Chromodynamics [2], is experimentally-supported most clearly by measurements of the multihadron cross-section in electron-positron colliders, which is three times larger than it would be if there were no colour charges.

It is interesting to note that the six flavours of quarks and of leptons can be organized into pairs of particles that fit into a hierarchy of masses. It is very tempting then, to group the fermions according to ad hoc *generations* (see table 1.1).

Each fermion can appear in nature as either right-handed or left-handed [1] apart from the neutrinos which, because they are believed to be massless and hence travel at the speed of light, are constrained to be left-handed only.

All of these particles have now been observed in nature, the top quark having

[1] A right-handed particle has its spin and momentum vectors aligned in parallel. They are anti-parallel for left-handed particles. Nature appears to favour left-handedness.

Generations		
I	II	III
$\begin{pmatrix} u \\ d \end{pmatrix}$	$\begin{pmatrix} c \\ s \end{pmatrix}$	$\begin{pmatrix} t \\ b \end{pmatrix}$
$\begin{pmatrix} \nu_e \\ e^- \end{pmatrix}$	$\begin{pmatrix} \nu_\mu \\ \mu^- \end{pmatrix}$	$\begin{pmatrix} \nu_\tau \\ \tau^- \end{pmatrix}$

Table 1.1: The fermion generations.

been identified only very recently [3]. The leptons appear as free particles, but because of color confinement free quarks are never observed, but form colourless bound states known as baryons (qqq) and mesons ($q\bar{q}$).

The quark doublets shown in table 1.1 are slightly incorrect, as the weak mixing of the flavour eigenstates has been ignored. The doublets are more correctly written as

$$\begin{pmatrix} u \\ d' \end{pmatrix} \begin{pmatrix} c \\ s' \end{pmatrix} \begin{pmatrix} t \\ b' \end{pmatrix} ,$$

where the dashed weak eigenstates are related to the flavour eigenstates by the Cabibbo Kobayashi Maskawa (CKM) matrix, which is a unitary rotation matrix and produces a linear mix of the three flavours:

$$\begin{pmatrix} d' \\ s' \\ b' \end{pmatrix} = V_{\mathrm{CKM}} \begin{pmatrix} d \\ s \\ b \end{pmatrix}$$

where the experimentally measured CKM matrix elements take the following values:

$$\begin{pmatrix} |V_{ud}| & |V_{us}| & |V_{ub}| \\ |V_{cd}| & |V_{cs}| & |V_{cb}| \\ |V_{td}| & |V_{ts}| & |V_{tb}| \end{pmatrix} = \begin{pmatrix} 0.9745 \text{ to } 0.9757 & 0.218 \text{ to } 0.224 & 0.004 \text{ to } 0.014 \\ 0.219 \text{ to } 0.224 & 0.9736 \text{ to } 0.9750 & 0.034 \text{ to } 0.046 \\ 0.002 \text{ to } 0.005 & 0.036 \text{ to } 0.046 & 0.9989 \text{ to } 0.9993 \end{pmatrix},$$

and the ranges given for the matrix elements represent the 90% confidence level limits. The dominant diagonal elements indicate the preference for sequential decays (i.e. top quarks decay preferentially to bottom quarks which decay mainly to charm quarks which decay mostly to strange quarks), and explain why for instance, the branching ratio of the tau lepton into pions ($u\bar{d}$) is greater than the branching ratio into kaons ($u\bar{s}$), as the matrix entry linking 'up' and 'down' is around five times the entry linking 'up' and 'strange'.

1.1.2 Gauge Bosons

Bosons are particles with integral spin ($0\hbar$, $1\hbar$, $2\hbar$, etc) so, for example, a spin 1 particle has a total angular momentum of magnitude $S = \sqrt{2}\hbar$ and can exist in three states with $S_z = +\hbar$, 0, $-\hbar$. The exchange of *virtual* bosons is the mechanism through which particles interact, the nature of the virtual boson determining which force is propagated. There are four fundamental forces: the electromagnetic force is mediated by the photon (γ); the strong force is propagated by gluons; the weak force manifests itself via the massive vector bosons, Z^0 and $W^{\pm}$; and the gravitational interaction is assumed to arise through the exchange of gravitons, but no experimental evidence has been found to confirm or refute this assumption. To 'feel' a force, a particle must possess the relevant quantum numbers, so the electromagnetic force then, will only act upon electrically charged particles; the strong force only couples to colour-charged particles (quarks and gluons); the weak force interacts with all fermions, and gravitation is felt by all particles.

1.1.3 Gauge Field Theories

Any system of interacting particles can be represented by a Lagrangian density [5], the symmetries of which will correspond to conserved quantities in Nature.

For a quantum mechanical system of fermions, mediated by virtual bosons, the phase of the descriptive wavefunction is unobservable and thus can be varied without changing the physical characteristics of the system. Demanding invariance under a global change in this phase (or gauge) produces charge conservation. The more stringent requirement of *local* gauge invariance (for which we require an invariant Lagrangian after arbitrary phase changes at each point in space-time) necessitates the introduction of compensating gauge fields, which correspond to the gauge bosons mentioned in the previous section.

The aesthetic appeal of the symmetry approach is very encouraging, but to produce a successful description of a particular type of interaction, it seems that a further requirement is necessary: the field theory must be renormalizable.

1.1.4 Renormalization

Renormalization [6] is a slightly controversial mathematical technique that amounts to subtracting infinity. To understand this, consider the Feynman diagram for electronic photon-emission shown in figure 1.1. The probability for such a process is obtained using perturbation theory, where each term in the expansion is calculated using one or more unique Feynman diagrams as necessary, and the total amplitude is the sum of the amplitudes from all the possible Feynman diagrams that have incoming and outgoing lines representing the interacting particles. The problems arise when one attempts to incorporate the diagrams that have 'loop corrections' (or vacuum polarisation diagrams), where a fermion line is internal to another line of the diagram (examples of which are shown in 'c' and 'd' in figure 1.1). This is because the calculation process involves summing over the momentum of the particles which, for the internal lines, are completely free and so are integrated over an infinite range, producing an infinite result. Renormalization then, involves simply incorporating these loop diagrams into the fermion lines, and using the experimentally measured values of charge, mass, etc, to continue with the calculation. This means that our picture of particles in QED (Quantum ElectroDynamics [7]) is considerably modified. For an electron, for example, we must now consider that there is some sort of 'bare charge' that is shielded by the higher-order processes, and furthermore, the

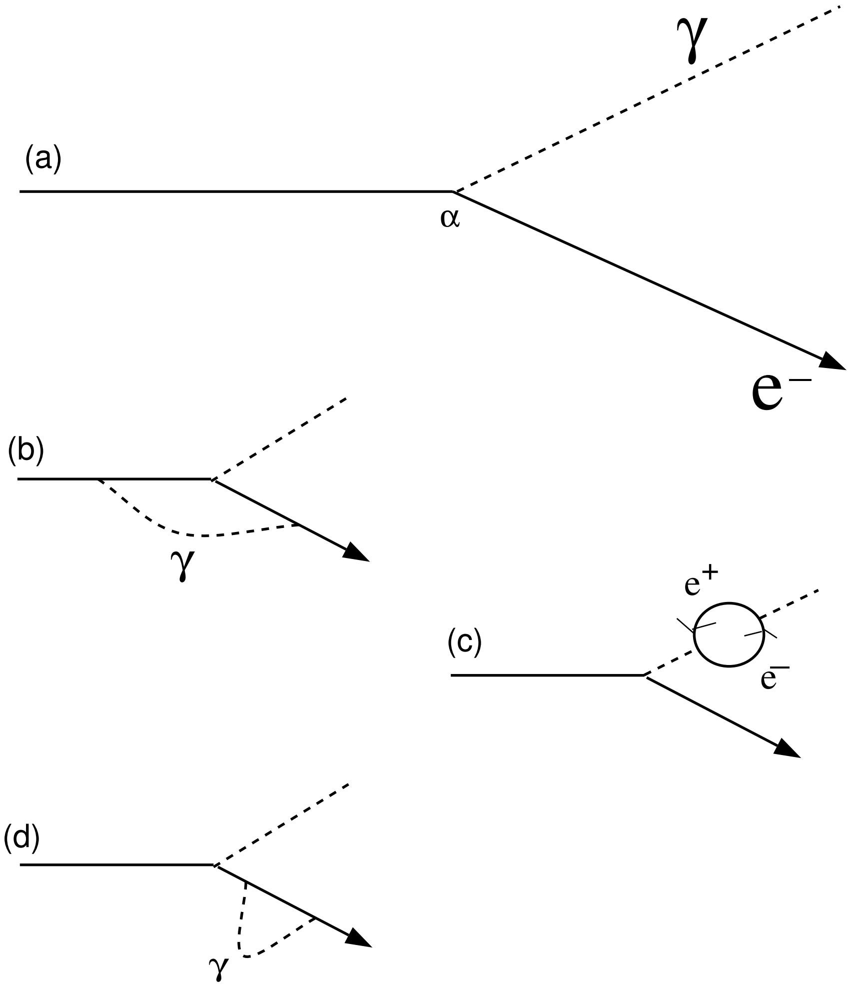

Figure 1.1: Some Feynman diagrams representing electronic photo-emission.

higher the energy of the probe used to examine the electron, the closer it gets to this 'bare charge' and the stronger is the apparent electromagnetic force. This is exactly what is seen in nature, and it is the reason for the 'running' of the electromagnetic coupling constant, α [2], which increases with energy, from $\approx 1/137$ at $Q^2 = M_e^2$ to $\approx 1/128$ at $Q^2 = M_Z^2$.

1.1.5 The Electroweak Theory

The electromagnetic and weak interactions were first unified by Glashow in 1961 [8]. Some years later Weinberg and Salam reformulated this work [9] in terms of a renormalizable gauge field theory that incorporated the (in)famous Higgs boson. In this theory, the two left-handed fermions in each generation are considered to be the two z-projections of a 'weak isospin' system ($I^W = \frac{1}{2}$), and the right-handed fermions are singlet states ($I^W = 0$). Rotations in weak isospin space map each of the left-handed fermions onto its generation partner, this transformation being part of the $\mathrm{SU(2)_L}$ group. The left-handed bias means that the maximal parity violation [10] observed in weak interactions is automatically included, and the change in the sign of the charge means that the rotation is describing charged-current processes. In nature however, there are neutral-current processes that take place with both left-handed and right-handed particles and so the transformation must be modified with $\mathrm{U(1)_Y}$, a further gauge transformation. The subscript 'Y' refers to 'weak hypercharge', which is constructed from the electric charge, Q, and the third component of weak isospin, I_3^W:

$$Y \;=\; 2(Q - I_3^W) \;\; . \tag{1.1}$$

To achieve local gauge invariance under the combined transformation $\mathrm{SU(2)_L} \times \mathrm{U(1)_Y}$, it is necessary to introduce four extra fields: a triplet, W_i, that couples to weak isospin; and a neutral field, B, that couples to weak hypercharge. The physical particles after symmetry breaking (below), are linear combinations of these fields, so that the $W^\pm$ are given by

$$W^\pm = \frac{1}{\sqrt{2}}(W_1 \mp W_2) \;\; . \tag{1.2}$$

and the Z^0 and γ (A) are given by:

$$Z^0 = W_3 \cos\theta_W - B \sin\theta_W \tag{1.3}$$

$$A = W_3 \sin\theta_W + B \cos\theta_W \quad , \tag{1.4}$$

where θ_W is the weak mixing angle (or Weinberg angle) that describes the degree of mixing between the weak and electromagnetic interactions. This Weinberg angle is not predicted by the theory and must take its value from experiment alone, the best value currently given by $\sin^2\theta_W = 0.2315(4)$ [22] at the Z^0 mass.

1.1.6 Broken Symmetry

The theory thus described is not consistent with nature since all the weak gauge bosons produced are so far massless whereas three of them are very massive in nature. This discrepancy is remedied by the introduction of a complex scalar Higgs field with non-zero vacuum expectation value. This field spontaneously destroys the symmetry [11] of the gauge theory, but imbues the three weak gauge bosons with mass and - in the simplest model - leaves one scalar Higgs field uncoupled, and this is the elusive Higgs boson (H^0). The theory allows no absolute fermion masses to be calculated (the photon mass and gluon mass are both required to be zero however, and the W and Z masses can be calculated from the measured weak and electromagnetic coupling constants), and so they have to be experimentally determined. The Higgs boson has not yet been found, but lower and upper bounds for the mass can be determined from other measured parameters and results. The current limits from LEP studies [12] set the Higgs mass between 58.4GeV/c^2 at 95% confidence, and approximately 500GeV/c^2. The next generation of experiments - particularly the LHC [13] - will be able to widen the search into the multi-TeV region where Higgs hypothesis will either stand or fall.

1.2 The Tau Lepton

The tau is the heaviest known lepton and is the only lepton to decay into hadrons. The tau is a sensitive probe of physics beyond the Standard Model because it is a member of the third generation of quarks and leptons, and participates in every aspect of Standard Model physics: it is produced in pairs via the electromagnetic and weak neutral currents in electron-positron collisions, it can decay via the weak charged current, and its hadronic decays probe the strong interaction at low values of momentum transfer where perturbative QCD becomes unreliable. Measurements of the leptonic decays of the τ allow a very accurate determination of α_s at M_z, and the accessible hadronic resonances ($a_1(1260)$, $\rho'(1450)$ and perhaps $\pi'(1300)$) may be probed in a relatively clean environment, free from a lot of the uncertainty associated with purely hadronic production measurements.

1.2.1 Early Tau Work

The tau lepton was first identified in 1975 by the Mark I collaboration [14], using the e^+e^- collider SPEAR. Their method operated on the assumption that if another lepton existed then it would decay into either of the two already existing leptons, and also into hadrons if it were sufficiently massive. The new-lepton search, then, relied upon finding '$e - \mu$' events, since it was believed that lepton number was conserved, and so the presence of these products would signify the pair production and decay of a higher-generation lepton. This conclusion would be further supported by the observation of 'missing energy' as this would be attributable to the four neutrinos which would be undetectable. These $e - \mu$ events were seen in 1974 [15], the maximum total energy being around 4GeV, thus indicating - if lepton number conservation were to be believed - that pair-production of a new particle of approximate mass 2GeV had occurred. Subsequently other events (known at the time as 'anomalous μ events') were seen, in which an emergent muon was accompanied by hadrons and some energy was left unaccounted for. This was taken as further evidence of having produced a pair of new and massive leptons, one of the pair having produced a muon and neutrinos, the other having decayed into hadrons and a neutrino. The tau neutrino, ν_τ, has yet to be observed in the laboratory but its existence is supported by a wealth of indirect evidence. Comparison of the observed decay spectra with that expected for the three-body leptonic decay and a two-body tau decay strongly indicate the neutrino's presence, and all searches for neutrino-less tau decays or two-body leptonic tau decays have proved fruitless. The distinctness of the ν_τ is well-demonstrated too, the Fermilab neutrino-beam experiment [16] determining low upper limits (0.002 and 0.073) for the direct coupling of the tau to ν_μ and ν_e respectively. Coupling with $\bar{\nu_\mu}$ and $\bar{\nu_e}$ is also ruled out by the non-observation of $\tau \rightarrow l\bar{\nu_l}\bar{\nu_l}$ (where l represents an electon or a muon) whose identical particles would alter the energy distribution of the charged lepton in a way not observed.

1.3 Leptonic Branching Ratios

The generic leptonic tau decay is shown in figure 1.2 below where p, $p^{'}$, k and $k^{'}$ are

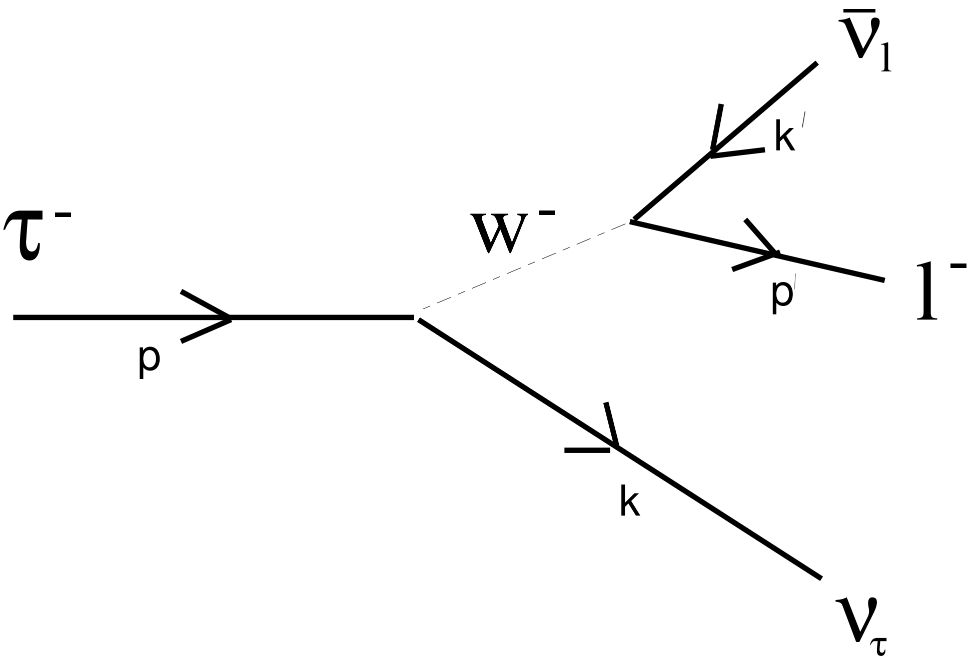

Figure 1.2: Leptonic tau decay.

the four-momenta of the particles. Using the standard Feynman rules, the invariant amplitude, $\mathcal{M}$, for the above process is written as:

$$\mathcal{M} = \frac{g_\tau}{\sqrt{2}}\left[\bar{u}(k)\gamma^\mu\frac{1}{2}(1-\gamma^5)u(p)\right]\frac{1}{(M_W^2-q^2)}\frac{g_l}{\sqrt{2}}\left[\bar{u}(p^{'})\gamma_\mu\frac{1}{2}(1-\gamma^5)u(k^{'})\right] \quad , \quad (1.5)$$

where g_τ and g_l are the electroweak couplings of the tau and lepton flavour l to the weak charged current; the u functions are Dirac spinors [2], the γ^μs are the standard gamma matrices, M_W is the W mass, and q is the propagated four-momentum (i.e. $q = p - k$).

From Fermi's Golden Rule, the rate of decay is given by

$$d\Gamma(\tau \to l\nu\bar{\nu}) = \frac{1}{2E}\overline{|\mathcal{M}|^2} dQ \quad , \tag{1.6}$$

Where dQ is the invariant phase space element given by

$$dQ = \frac{d^3p'}{(2\pi)^3 2p'^0}\frac{d^3k}{(2\pi)^3 2k^0}\frac{d^3k'}{(2\pi)^3 2k'^0}(2\pi)^4\delta^{(4)}(p - p' - k - k') \quad , \tag{1.7}$$

Following the usual convention, we substitute $p^0 = E$, $p'^0 = E'$, $k^0 = \omega$ and $k'^0 = \omega'$, and then integrate with respect to d^3k, using the equality

$$\int \frac{d^3k}{2\omega} = \int d^4k S(\omega)\delta(k^2) \tag{1.8}$$

where $S(\omega)$ is a step function, equal to unity for positive omega, and zero otherwise. The equation becomes:

$$dQ = \frac{1}{(2\pi)^5}\frac{d^3p'}{2E'}\frac{d^3k'}{2\omega'}S(E - E' - \omega')\delta\left((p - p' - k')^2\right) \tag{1.9}$$

where θ is the angle between the product lepton and its neutrino.

Now, it is necessary to average the invariant amplitude over the possible spins of the participating particles. If this is done and the propagated energy, q, is neglected (since $M_W^2 >> q^2$ usually), then this average, $\overline{|\mathcal{M}|^2}$, is given by:

$$\begin{aligned} \overline{|\mathcal{M}|^2} &\equiv \frac{1}{2}\sum_{\text{spins}} |\mathcal{M}|^2 && (1.10) \\ &= 64G^2\,(k.p')(k'.p) \quad . && (1.11) \end{aligned}$$

Where the Fermi coupling constant, G, has been introduced. G is given by

$$G = \frac{g_\tau g_l}{4\sqrt{2}M_W^2} \quad . \tag{1.12}$$

If we operate in the rest frame of the τ so that only the mass component of the four vector is non-zero, and if we assume that the masses of the products can reasonably be approximated to zero (since the tau mass is so much greater), then it can be shown that

$$2(k.p')(k'.p) = m_\tau \omega'(m_\tau^2 - 2m_\tau\omega') \ . \tag{1.13}$$

By substitution of (1.10), (1.12) and (1.8) into (1.6), the decay rate becomes:

$$\begin{aligned} d\Gamma(\tau \to l\nu\bar{\nu}) &= \frac{G^2}{2m_\tau\pi^5}\frac{d^3p'}{2E'}\frac{d^3k'}{2\omega'}m_\tau\omega'(m_\tau^2 - 2m_\tau\omega') \\ &\quad\times\delta(m_\tau^2 - 2m_\tau E' - 2m_\tau\omega' + 2E'\omega'(1-\cos\theta)) \\ &= \frac{G^2}{2m_\tau\pi^5}\frac{d^3p'}{2E'}\frac{d^3k'}{2\omega'}m_\tau\omega'(m_\tau^2 - 2m_\tau\omega') \\ &\quad\times\frac{1}{2E'\omega'}\delta(2E'\omega'(m_\tau^2 - 2m_\tau E' - 2m_\tau\omega') + 1 - \cos\theta) \ . \end{aligned} \tag{1.14}$$

Completing the change of variables, we replace $d^3p'd^3k'$ by $4\pi E'^2 dE' 2\pi\omega'^2 d\omega' d\cos\theta$ and integrate over θ giving

$$d\Gamma(\tau \to l\nu\bar{\nu}) = \frac{G^2}{2\pi^5}dE'd\omega' m_\tau\omega'(m_\tau - 2\omega') \ . \tag{1.15}$$

The argument of the delta function then, determines the energy of the decay products. A range of energies are possible, depending upon the value of $\cos\theta$ (which can only lie between -1 and +1), and these are:

$$\frac{1}{2}m_\tau - E' \leq \ \omega' \ \leq \frac{1}{2}m_\tau \tag{1.16}$$

$$0 \leq \ E' \ \leq \frac{1}{2}m_\tau \tag{1.17}$$

where E' is the energy of the 'daughter' lepton, and ω' is the energy of the corresponding neutrino. Integrating between these limits then, the energy spectrum of the daughter lepton is

$$\begin{aligned} \frac{d\Gamma(\tau \to l\nu\bar{\nu})}{dE'} &= \frac{m_\tau G^2}{2\pi^3}\int_{\frac{1}{2}m_\tau - E'}^{\frac{1}{2}m_\tau} d\omega' \ \omega'(m_\tau - 2\omega') \\ &= \frac{G^2}{12\pi^3}m_\tau^2 E'^2\left(3 - \frac{4E'}{m_\tau}\right) \ . \end{aligned} \tag{1.18}$$

and thus with one more integration we can obtain the decay rate:

$$\begin{aligned} \Gamma(\tau \to l\nu\bar{\nu}) &= \int_0^{m_\tau/2} dE' \frac{d\Gamma}{dE'} \\ &= \frac{G^2 m_\tau^5}{192\pi^3} \ . \end{aligned} \tag{1.19}$$

This expression is not quite accurate however, since in deriving it both the masses of the final state leptons, and the exchanged four-momentum were neglected. To correct for these approximations, two factors must be included: F_W adjusts for the finite nature of the W mass, and is given by

$$F_W = 1 + \frac{3M_\tau^2}{5M_W^2}; \tag{1.20}$$

and F_l [17] allows the final state lepton masses to be included, the required expression being

$$F_l(x) = 1 - 8x + 8x^3 - x^4 - 12x^2 ln(x) \tag{1.21}$$

where

$$x = M_l^2/M_\tau^2. \tag{1.22}$$

with M_l and M_τ representing the (heaviest) final lepton and tau masses respectively. It is found that an additional factor is necessary to model fully the process under discussion, since no consideration has yet been given to the effects of electromagnetic radiation. This further factor is given by

$$F_{rad} = 1 + \frac{\alpha(M_\tau)}{2\pi}\left(\frac{25}{4} - \pi^2\right) \quad , \tag{1.23}$$

where $\alpha(M_\tau)$ is the fine structure constant calculated at the tau mass. The given factor, F_{rad}, represents the adjustment necessary when the effect of the emission of real photons and fermion pairs, as well as virtual photons, are considered. The final corrected partial width for the leptonic τ decay is given, then, by the following expression:

$$\begin{aligned} \Gamma(\tau \to l\nu\bar{\nu}) &= \frac{G^2 m_\tau^5}{192\pi^3} F_l(x) F_W F_{rad} \\ &= \frac{g_\tau^2 g_l^2}{(8M_W^2)^2} \frac{m_\tau^5}{96\pi^3} F_l(x) F_W F_{rad} \quad . \end{aligned} \tag{1.24}$$

As we can see, the partial width is dependent upon (the fifth power of) the τ mass, a relationship that allows the partial width, the branching fraction and the lifetime to be linked and tested for consistency. This is explored later in Section 7.5.

1.3.1 Other Branching Ratios.

The τ is unique amongst leptons in that it has sufficient mass to decay hadronically. The level of statistics is now such that branching fractions can be obtained for a great many of the possible decay channels. The best figures so far obtained are given in table 1.2.

Decay Mode	Branching Ratio (%)
$1-$prong	
particle$^-$(≥ 0 neutrals)ν_τ	84.96 ± 0.14
$e^-\bar{\nu}_e\nu_\tau$	17.83 ± 0.08
$\mu^-\bar{\nu}_\mu\nu_\tau$	17.35 ± 0.10
$h^-(\geq 0$ neutrals$)\nu_\tau$	49.78 ± 0.17
$\pi^-\nu_\tau$	11.31 ± 0.15
$\mathrm{K}^-\nu_\tau$	0.71 ± 0.05
$\rho^-\nu_\tau$	25.24 ± 0.16
$h^-2\pi^0\nu_\tau$	9.50 ± 0.14
$h^-3\pi^0\nu_\tau$	1.28 ± 0.10
$h^-4\pi^0\nu_\tau$	0.18 ± 0.06
$3-$prong	
$2h^-h^+(\geq 0$ neutrals$)\nu_\tau$	14.91 ± 0.14
$2h^-h^+\nu_\tau$	9.80 ± 0.10
$2h^-h^+(\geq 1$ neutrals$)\nu_\tau$	5.08 ± 0.11
$5-$prong	
$3h^-2h^+(\geq 0$ neutrals$)\nu_\tau$	0.097 ± 0.007
$\mathrm{K}^*(892)^-\nu_\tau$	1.28 ± 0.08

Table 1.2: Shown are the PDG96 branching ratio values for the most common decay modes of the τ^-. The '$h^\pm$' represents a pion or a kaon, and a 'neutral' signifies a neutral hadron (that subsequently decays to some combination of π^0's and γ's).

1.3.2 The τ Mass

Particle masses are not predicted by the Standard Model, and so have to be determined purely experimentally. It appears to be the masses alone that create the difference between the generations, and so an accurate measurement is of fundamental importance. Of course, the mass is also of great practical importance since it enters the calculations of the rates for processes, and is an argument of the running coupling constants. In the branching ratio formula calculated previously, the mass enters in the fifth power, and so the uncertainty on this quantity is very significant, especially when performing the universality check (see Section 7.5).

The most precise measurement to date of the τ mass was made using the Beijing Spectrometer (BES) at the Beijing Electron-Positron Collider (BEPC) [18]. To make this measurement, the $e^+e^- \to \tau^+\tau^-$ cross-section was determined for a range of energies within a few MeV of the threshold for τ production.

Originally, tau decays were selected by requiring each τ to decay leptonically, but with one producing a muon and the other producing an electron. This produced a highly pure di-tau sample, but had low statistics. In a recent re-analysis of the whole data sample, dilepton and lepton-hadron events were also allowed to contribute, thus yielding a much more accurate result:

$$M_\tau = 1776.96^{+0.18+0.20}_{-0.19-0.16}\,\mathrm{MeV} \tag{1.25}$$

The other approach to determining the τ mass is from a consideration of hadronic decay kinematics. Pursued by the ARGUS [19] and CLEO [20] collaborations, this involves the reconstruction of three-charged-pion τ decays, in which the τ direction is approximated by the direction of the charged decay products, and a pseudomass, m^*_τ, is defined as:

$$m^*_\tau = 2(E_\tau - E_{3\pi})(E_{3\pi} - p_{3\pi}) + m^2_{3\pi} \tag{1.26}$$

where $E_\tau \approx E_b$ is the τ energy, and $E_{3\pi}$, $p_{3\pi}$ and $m_{3\pi}$ are the energy, momentum and mass of the three-pion system. This pseudomass tends towards the real τ mass as the energy taken away by the neutrino tends to zero, and the earlier direction approximation becomes more valid. The pseudomass spectrum then, exhibits an abrupt cut-off at the upper limit (see figure 1.3), the position of which is directly related to m_τ. The results from this method are

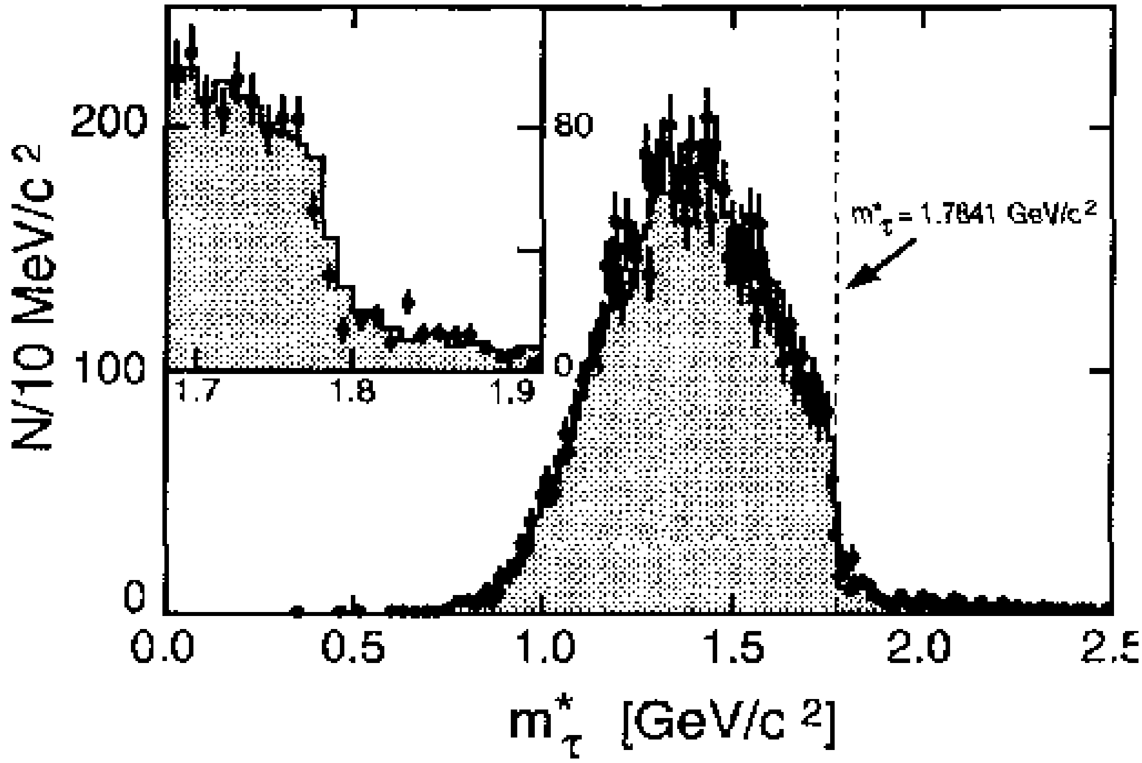

Figure 1.3: Pseudomass distribution from $\tau \to \pi^-\pi^-\pi^+\nu_\tau$ showing data (points with error bars) and Monte Carlo (shaded histogram) [19].

$$M_\tau = 1776.3 \pm 2.4 \pm 1.4\,\mathrm{MeV} \quad \text{for ARGUS} \tag{1.27}$$

$$M_\tau = 1777.8 \pm 0.7 \pm 1.7\,\mathrm{MeV} \quad \text{for CLEO} \tag{1.28}$$

which are in good agreement with the BES measurement.

1.3.3 The τ Lifetime

The first measurement of the τ lifetime was made by the MARK II collaboration in 1983 [21], when it was found to be 320$\pm$54 fs. Currently the LEP experiments, with their excellent tracking capabilities and almost ideal τ-pair production environments, have reduced the uncertainty enormously, the current world average being 291.0$\pm$1.5 fs [22].

The techniques of measuring the lifetime fall into two broad categories: the 'traditional' methods which look at each τ individually, and the more recent 'correlation' methods which utilise simultaneously the information from both of the taus. The 'decay length method' [23] is an example from the first category, and uses three-prong tau decays to determine directly the tau's flight distance, and hence it's Lorentz-boosted lifetime. The 'impact parameter method' [24] is from the latter category, and involves consideration of the 'miss distance' of each tau in events of 1-1 topology. The decay length method is the most powerful of these techniques, since it uses directly the flight distance of the tau, and so could theoretically give an error related simply to the number of three-prong events selected. However, since only 15% of taus decay in the three-prong channel, and since quite stringent vertex quality cuts are often necessary, the statistics involved in this approach are generally quite low. A schematic diagram in figure 1.4 shows the decay length method for a typical three-prong event. The best OPAL measurement using this method gives

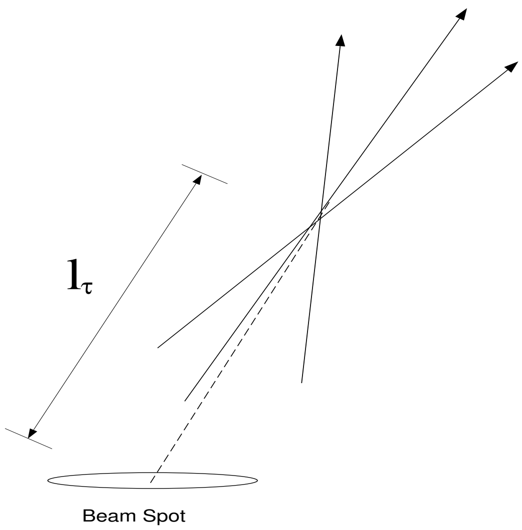

Figure 1.4: Schematic diagram of the decay length method.

the result

$$\tau_{dl} = 289.0 \pm 3.6\,(\mathrm{stat}) \pm 1.8\,(\mathrm{syst})\ \mathrm{fs} \quad [25]$$

The impact parameter method is an indirect measure of the decay length and so has a higher associated uncertainty, but can be used with the 'other' 85% of tau decays, so is a complementary and statistically independent method. In the simplest case, the impact parameter is defined as the smallest distance in the $r - \phi$ plane between the extrapolated track and the assumed production point, as shown in figure 1.5 below. The dashed line in the figure represents the event (or thrust) axis, which

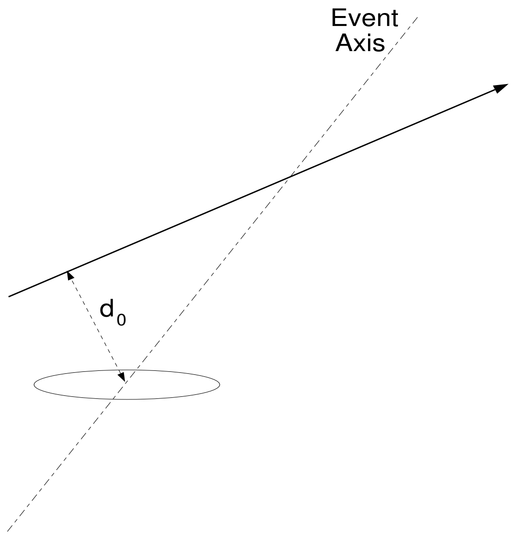

Figure 1.5: Schematic diagram of the impact parameter method.

is defined as the average polar angle, θ, of the two τ cones. If the reconstructed track does not cross the thrust axis on the same side of the beam-spot as the cone, then the impact parameter is assigned a negative value. This does not compromise the lifetime measurement however, which is obtained through comparison with smeared Monte Carlo so that the lifetime, τ_τ , is given by

$$\tau_\tau = \tau_{MC} \frac{x_{data}}{x_{MC}} ,$$

where τ_{MC} is the Monte Carlo lifetime and x_{data}, x_{MC} are the mean impact parameters of the data and Monte Carlo respectively. The best OPAL measurement gives

$$\tau_{ip} = 290.4 \pm 3.5(\text{stat}) \pm 2.2(\text{syst}) \text{ fs} \quad [25]$$

However, since the two described methods are statistically independent, their results can be simply combined to yield an overall lifetime of:

$$\tau_{ave} = 289.2 \pm 1.7(\text{stat}) \pm 1.2(\text{syst}) \text{ fs}$$

This compares with the current world average of

$$\tau_{ave} = 290.21 \pm 1.15 \text{ fs} \quad [60]$$

Chapter 2

The Detector

2.1 The LEP Collider

The Large Electron Positron Collider [26] is an underground ring, lying at a mean depth of 100m, and straddling the French-Swiss border near Geneva.

Bunches of electrons and positrons circulate in opposite directions, and are made to collide within a range of centre-of-mass energies, centred upon the mass of the Z^0. This 'scanning' around the Z^0 resonance allows mass, decay widths and fermionic couplings to be measured [27]. At the end of the 1995 run however, some much higher energy runs were made to help facilitate the transition to LEP2 [28], which began in earnest with the 1996 run and will operate at a centre of mass energy above the W^+W^- threshold. The electrons and positrons are allowed to make contact at four points on the 26.7 km circumference, about which the detectors ALEPH [29], DELPHI [30], L3 [31] and OPAL [32] have been constructed.

2.1.1 The Injection System

Thermionic emission produces the electrons which are accelerated by the LEP Injector Linac (LIL) to 200 MeV, and are channelled towards a tungsten target. The consequent deceleration of the impinging electrons produces bremsstrahlung photons which can convert into e^+e^- pairs. These are separated with a magnetic field and stored in the Electron-Positron Accumulator (EPA) at an energy of 600MeV.

This process continues until the particle populations are high enough, at which point the electrons and positrons are injected into the Proton Synchrotron (PS) and accelerated to 3.5GeV. Once this energy is reached the particles are passed to the Super Proton Synchrotron (SPS) and further accelerated to 20GeV when they are injected into LEP. The accelerating apparatus is shown schematically in figure 2.1.

2.1.2 The Accelerating System

The electrons and positrons move in a (roughly) circular orbit, and are thus under (almost) constant centripetal acceleration. An accelerated charge emits synchrotron radiation, and loses energy at a rate roughly proportional to the fourth power of its momentum (in the relativistic approximation). Since the particles in LEP are moving extremely rapidly, this energy loss is significant and must be compensated if the desired collision energy is to be maintained. This energy maintenance is achieved with 128 copper radio frequency (RF) cavities, which are powered by sixteen 1 MW klystrons and are also the means by which the particles are accelerated.

The radiated energy of each particle per cycle is given by:

$$\Delta E = \frac{4\pi}{3}\,\frac{e^2\beta^2\gamma^4}{R} \tag{2.1}$$

where R is the radius of the ring, β is the particle velocity as a fraction of the speed of light, and $\gamma = (1-\beta^2)^{-1/2}$.

At the Z^0 mass, this energy loss is around 250MeV per particle so with bunch numbers of around 10^{11} the overall power consumption is very large. The power consumption can be reduced by decreasing the centripetal acceleration (by having a larger-radius ring) or by simply using more efficient devices such as the superconducting cavities used in LEP2.

2.1.3 The Beam Transport System

It is clearly advantageous for the particle bunches to survive as long as possible in the experimental environment. To this end, the beam pipe is evacuated to something less than 3×10^{-9} torr; and there are some 3000 dipole magnets (for bending) and nearly 2000 quadrupole, sextupole or octupole focusing magnets which serve to maintain the beam's integrity and prevent 'evaporation'.

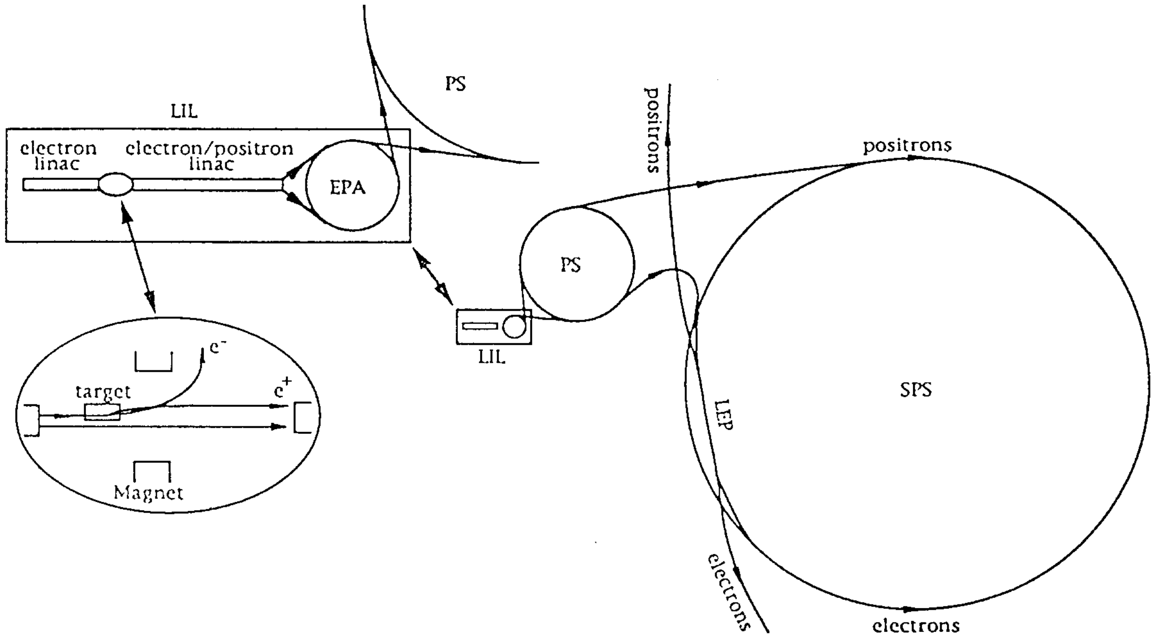

Figure 2.1: The LEP injection system

2.2 The OPAL Detector

As mentioned before, the OPAL (Omni-Purpose Apparatus for LEP) detector is situated at one of the four interaction points of the LEP ring. Its purpose is to envelop the vertex as completely as possible, and to record the characteristics of any emergent particle, so that the most detailed reconstruction can be obtained.

To achieve this, the detector comprises several specialised elements, each tailored and positioned such that all known final-state particles (barring neutrinos) can be detected with good overall efficiency. With this in mind, OPAL was assembled as a set of concentric cylindrical subdetectors, centred upon the interaction point and sealed at either end by the endcap detectors. Near the beam pipe are the vertex detectors which help to identify short-lived particles that decay within a small distance. Around these are the tracking chambers which measure particle trajectories and, with the applied magnetic field, allow the charge and momentum to be ascertained. Without this central volume lie the calorimeters which absorb and measure the energy of electrons, photons and hadrons. The electromagnetic calorimeter is first, and is designed to detect photons and electrons via electromagnetic showering. Particles emerging from here enter the hadron calorimeters which effectively absorb everything but energetic ($p > 3$ GeV/c) muons and neutrinos. These pass through to the muon chambers where the muons are detected and track reconstruction is possible.

The next section describes these subdetectors in more detail, and diagrams are included to show more clearly the nature of the assembly and its co-ordinate system (see figures 2.2 and 2.3). The main co-ordinate system in OPAL is the standard right-handed Cartesian system, the origin of which is defined by the centre of the jet chamber (which is close to the beam interaction point). The z-axis is defined by the direction of the electron beam through OPAL; the x-axis points towards the centre of the LEP ring; and the y-axis is then almost vertical (not exactly because LEP is tilted at 0.8° to the horizontal). The coordinate system shown in figures 2.2 and 2.3 uses spherical polar co-ordinates (r, θ, ϕ). The angle of azimuth, ϕ, is measured about the z-axis with the positive x-axis defining $\phi = 0$. The polar angle, θ, is measured from the positive z-axis, and the spherical radius from the origin is denoted by r.

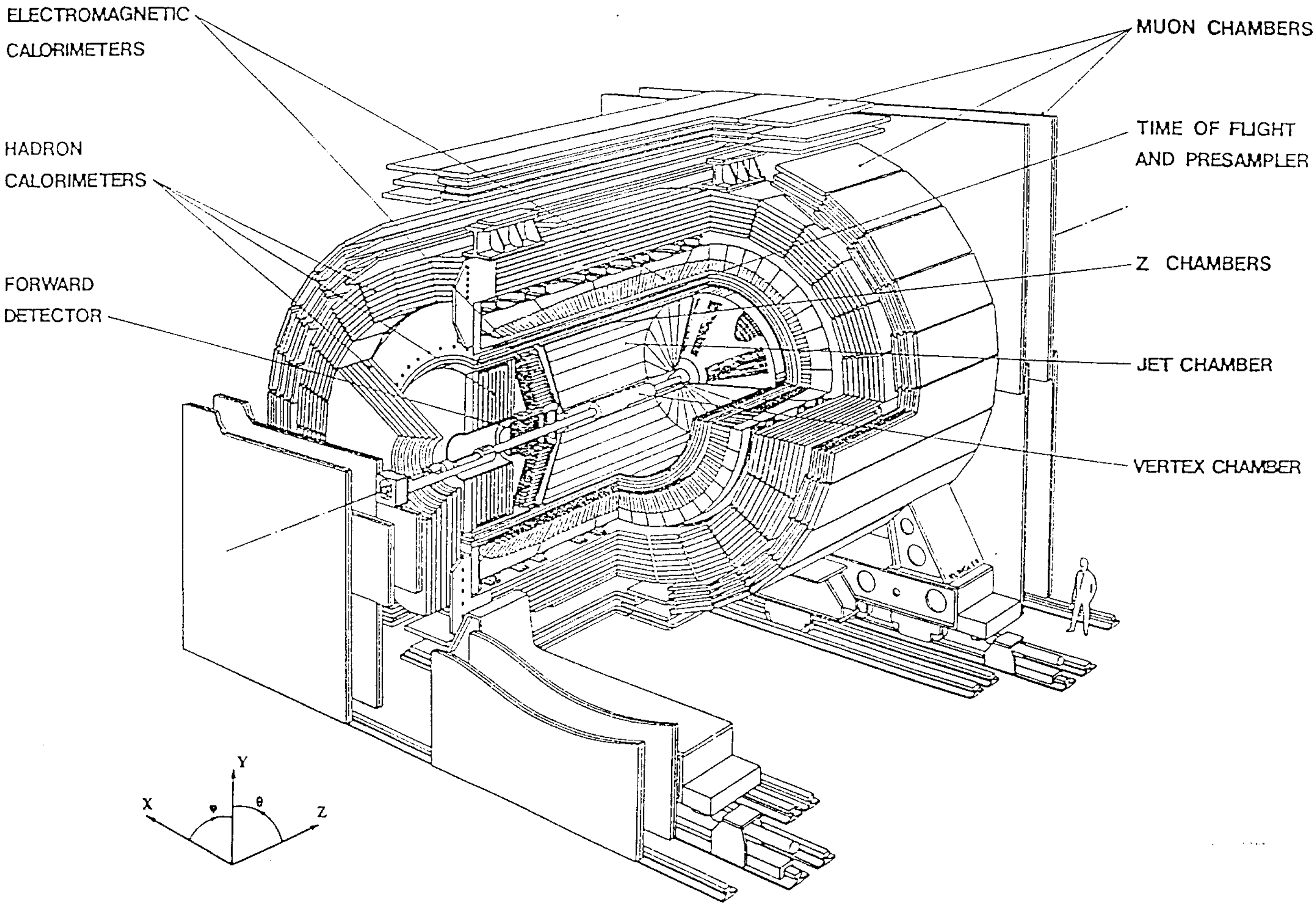

Figure 2.2: The OPAL Detector

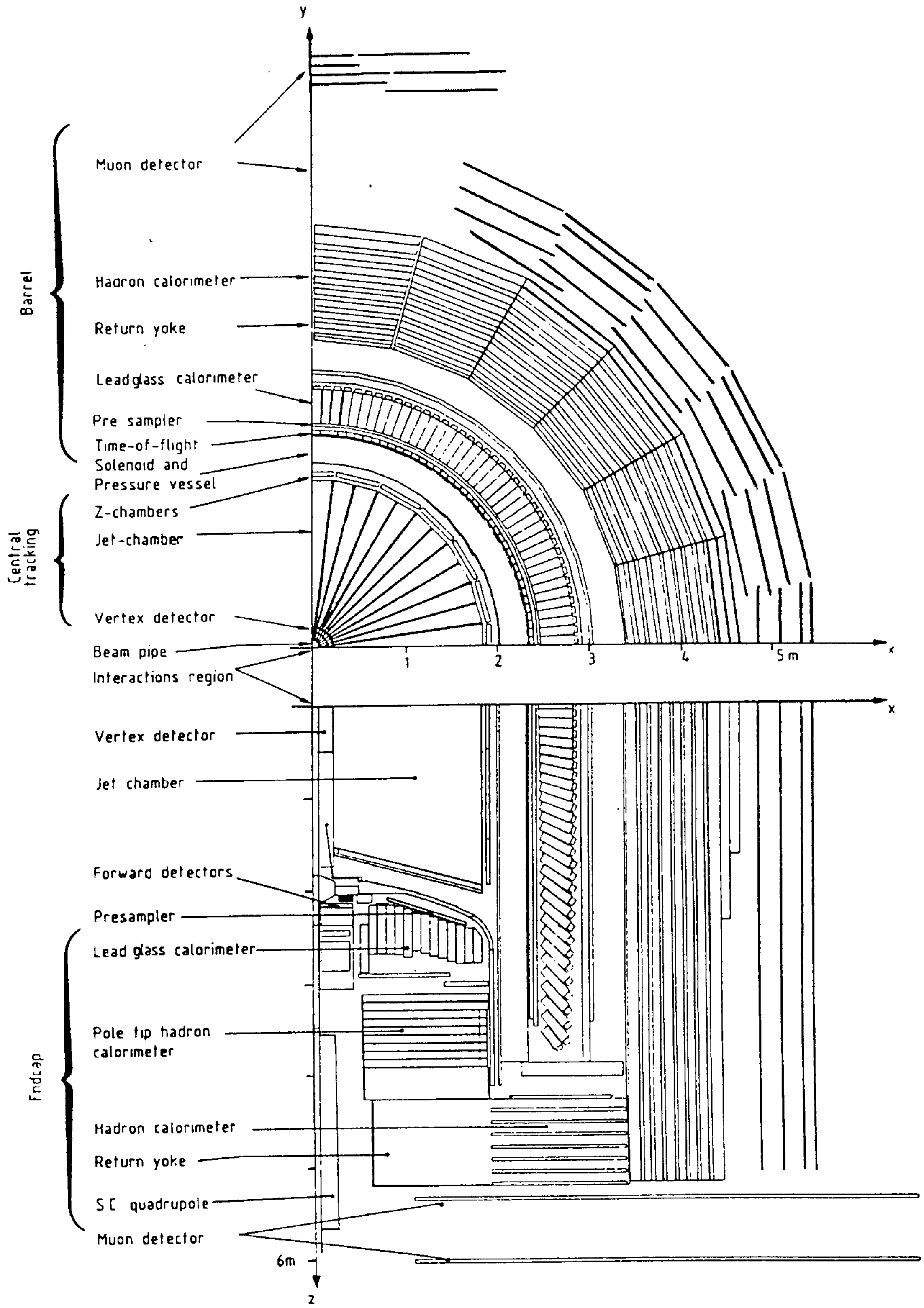

Figure 2.3: Cross-section of the detector

2.3 The OPAL Subdetectors

2.3.1 The Central Detector

Most of the central detector, silicon excepted, lies inside a pressure vessel whose pressure is maintained at 4 bar, and is positioned between the beam pipe and the magnet coil. This detector comprises three drift chamber devices - the vertex detector, the jet chamber and the Z chambers - along with the silicon microvertex detector. Each of these are described below.

The Silicon Microvertex Detector

Installed in the middle of the 1991 physics run and subsequently upgraded, the microvertex detector [33] is made from two concentric cylinders of double-sided silicon with diameters 12cm and 15cm, centred upon the beam pipe. The spatial resolution is very fine, allowing a precision of some $5-10$ μm which is necessary as the main function of this subdetector is to reconstruct vertices and determine the track impact parameter.

The Vertex Detector (CV)

This 470mm diameter, metre-long barrel surrounds the microvertex detector [34], and functions as a drift chamber. Twelve wire layers lie parallel to the beam axis in the smaller of the two concentric cylinders (so these are called *axial wires*), and are used for determining azimuthal co-ordinates. Surrounding them are the six layers of *stereo wires* which are inclined at four degrees to the beam axis, thus improving the z-resolution. Overall, the detector achieves a precision of 55μm in $r-\phi$, and 700μm in r-z

The Jet Chamber (CJ)

This, the second of the drift chambers, is a large multiwire device [35], stretching from 25cm from the beampipe to 185cm. In azimuth, each fifteen degrees of this volume contains a plane of 159 sense wires, spaced at 10mm intervals and lying parallel to the beampipe. The multitude of sense wires allow much about the nature of a passing charged particle to be gleaned, particularly since it is a *multihit* chamber and does not, as with earlier designs, record only the nearest ionisation site to the wire. The chamber works by ionisation, so the time taken for electrons to drift to the wires fixes the position in $r-\phi$. The quantity of charge reaching each end of the sense wire determines the z coordinate; and the *total* charge received by the wire allows the rate of loss of energy, dE/dx, to be computed. This quantity is a very important discriminator, particularly between charged hadrons, and is enhanced by the high pressure of the chamber. A higher pressure would be beneficial in terms of more ionisation and a lower Lorentz angle, but is not used because of the detrimental effect upon the electrons' drift time, and hence the two-track resolution.

If particles pass parallel and close to the wire planes of the anode, reconstruction problems occur, causing incorrect track positions and curvatures to be assigned. Section 3.3 discusses this in more detail.

The Z Chambers (CZ)

CZ [36] is the last of the subdetectors to lie within the magnet. Twenty-four 4m long chambers are arranged symmetrically in azimuth, each being split lengthwise into eight sections. Each section has six anode wires which are at right-angles to the beam axis. Thus the z coordinate can be resolved to an accuracy of around 300μm, and the degree of charge-sharing will give ϕ with a resolution in $r-\phi$ of 15mm.

2.3.2 The Magnet

The OPAL magnet is designed to produce a uniform field throughout the central detector. The water-cooled solenoid inside an iron yoke (whose other function is to act as showering material for the subsequent hadron calorimeter) produces a uniform field of 0.435 T, parallel to the Z-axis.

2.3.3 The Time of Flight Counters (TOF)

The time of flight system comprises 160 scintillation counters, 6.84m in length, that are arranged around the solenoid to provide data for triggering, to aid in the identification of low-momentum (0.6 - 2.5 GeV/c) charged particles, and to help in discriminating against cosmic rays.

2.3.4 The Electromagnetic Detector

This part of the detector comprises a presampler and a lead-glass calorimeter.

The Electromagnetic Presampler

The fact that there are roughly 2 radiation lengths of material before the calorimeter is reached means that some sort of presampling of the position and energy of any showers is necessary [37]. Approximately three-quarters of the electrons and photons will have interacted in this material, so the spatial resolution would be very poor if the calorimeter alone were relied upon. In the barrel region, the presampler comprises two layers of streamer tubes, whereas a thin-gap multiwire proportional chamber does the presampling in the endcap region.

The Electromagnetic Calorimeter (ECAL)

Some 9440 lead glass blocks, each subtending a solid angle of about 40mrad^2 and covering $|\cos\theta| < 0.82$ make up the barrel region of the calorimeter, and 1132 lead glass blocks arranged in a dome shape at each end extend the acceptance to $|\cos\theta| = 0.98$. Both barrel and endcap are equipped with photodetectors to measure the Čerenkov radiation produced by electron-positron pairs in the showers within the lead-glass. In the barrel photomultipliers are used, whereas the endcap uses vacuum photo-triodes. The calorimeter's 24.6 radiation lengths effectively provide complete absorption of electrons and photons with reasonable energy resolution, giving $\sigma_E/E \simeq 15\% /\sqrt{E}$ in the barrel, and $\sigma_E/E \simeq 20\% /\sqrt{E}$ in the endcap [38] for the electron energy measurement.

2.3.5 The Hadron Calorimeter (HCAL)

The energy of charged and neutral hadrons that have passed through the ECAL is measured by the hadron calorimeter [39]. Detectors are positioned between the layers of the magnet return yoke and altogether provide an extra 4 interaction-lengths of coverage over a solid angle of 97% of 4π. This ensures that the vast majority of particles passing through to the muon chambers will indeed be muons. The HCAL is divided into three regions. The barrel comprises eight iron slabs, each 10cm in thickness, which are sandwiched by nine layers of streamer tubes. This portion of the HCAL accounts for the region for which $|\cos\theta| < 0.81$. The hadron endcap also has an alternate iron slab/streamer-tube arrangement, but there is one fewer of each layer here. The endcaps extend the coverage over $0.81 < |\cos\theta| < 0.91$. Lastly, ten thin multiwire proportional chamber layers in the pole-tip of the magnet are interspersed with ten 8cm-thick iron plates. These chambers comprise the hadron pole-tip calorimeter, and they extend the acceptance to $|\cos\theta| = 0.99$. The typical energy resolution for a 10GeV hadron is around $\sigma_E/E \simeq 120\% / \sqrt{E}$ and, depending upon the number of detector layers involved, the muon detection efficiency lies between 60 and 90%. The hadron calorimeter can be used very effectively to separate hadrons from muons, and this is discussed in more detail in Chapter 6.

2.3.6 The Muon Detector

Once outside the hadron calorimeter, any particles present have had to pass through the equivalent of 1.3m of iron, which constitutes more than seven interaction lengths for a pion, and so they will be depleted to less than 0.1% of their initial numbers, meaning that the majority of particles emerging from the hadron calorimeter are muons. The coverage of the muon chambers extends over approximately 93% of the solid angle, and the efficiency for detecting emergent muons (those with energy greater than around 2.3GeV) is close to 100%. The advantages of using such a simple and efficient system for identifying muons is evident in the low systematic error associated with this analysis.

The Muon Barrel (MB)

The muon barrel [40] contains 110 drift chambers, each 1.2 m wide and 90 mm thick. Most of these chambers are 10.4 m long (some are shorter because of the magnet's support structures) and cover the region in which $|\cos\theta| < 0.72$. The arrangement of wires within these units allows charge-drifting of up to 30cm with the drift time providing the $r - \phi$ measurement to an accuracy of 1.5 mm. An array of diamond-shaped cathode pads across from the anodes allows the z coordinate to be calculated, positional ambiguities being prevented by the diamond shape of the cathode. This innovative system gives a resolution of around 1.5 mm.

The Muon Endcap (ME)

The muon endcap detectors [41] extend the acceptance to $|\cos\theta| = 0.98$, and are composite bodies themselves: there are four 'quadrant' chambers, which are approximately 6m square; and two 'patch' chambers of dimensions 4m by 2.5m at each end of the detector. These chambers are arranged so as to provide maximum coverage, given the physical restrictions of the beam pipe, the power and gas supplies, and the structural supports.

Each of the chambers are made from two double-layers of streamer-tubes, 67cm apart (in z). The gas flowing through the chambers is a composition of argon (which is ionized by the muons) and isobutane (which is also ionised but is present because its many degrees of kinetic freedom absorb photons and thus quench the charge avalanche caused by the initial ionisation in the streamer-tube). The mutually-orthogonal arrangement of the readout strips on either side of the streamer tubes allows position measurement in two projections. The spatial resolution achieved is around 3 mm (parallel to wires) and 1 mm (perpendicular to wires).

2.3.7 The Forward Detector and SiW Luminometer

The forward detector [42] detects particles that emerge at very small angles (40mrad to 200mrad) to the beam, so it is particularly useful for picking up Bhabha-scattered electrons, from which the beam luminosity can be calculated to an accuracy of 0.6%. The detectors themselves lie 2.6m either side of the interaction point, and are composed of an electromagnetic calorimeter (24 radiation lengths of lead-glass scintillator) and some drift chambers [43] to measure the shower positions.

In 1993 a silicon-tungsten luminometer comprising nineteen layers of silicon interspersed with tungsten wafers, improved the accuracy of the luminosity measurement to 0.07% [44].

2.4 The Trigger System

Since the bunch-crossing rate at LEP is around 45 kHz (in the 4×4 running mode (4 bunches of electrons against 4 bunches of positrons)), there is a possible collision every 22μs, so to avoid dead time, the previous collision has to be processed within this very short time interval. The full digitisation of such a collision requires roughly 20ms and so some faster method of discrimination between real physics interactions and spurious background signals (such as detector noise, collisions of beam particles with the gas or the beam pipe, cosmic rays, etc.) must be employed.

Data volume is reduced to an acceptable level (without sacrificing physics events) by having each contributing subdetector (the presampler subdetector and SI do not participate) provide two kinds of output to the central triggering system [45]. There are 'stand-alone' triggers, like energy sums in the calorimeters or track counts; and there is a second trigger in which the solid angle covered by OPAL is divided into a matrix of overlapping volumes, with 6 divisions in theta and 24 divisions in phi. The subdetectors provide data for the theta-phi trigger elements, and these are quickly analysed in parallel with the stand-alone triggers for 'evidence' of a genuine physics interaction having occurred. If this is found not to be the case, the whole detector is reset in time for the next bunch-crossing. With the advent of 8×8 running, the beam-crossing frequency was doubled (to 90kHz) and so a pre-triggering system [46] was introduced. This worked upon the same principles as the solid angle matrix output described above, but the subdetectors were divided into only six ϕ segments and so the whole process functioned much more rapidly.

2.5 The Data Acquisition System

If the characteristics of an event meet the selection criteria of the central trigger, a signal with an event number is sent to each subdetector. The subdetector hardware is then read out, and this raw data is processed by the Local System Crate (LSC - a VME crate) to reformat it and reduce the data size so that it can be handled by another VME crate called the OPAL Event Builder [47]. This crate combines all the available information and produces a set of data for the whole event, which it passes on to the filter [48].

The filter is the final selective stage, and it uses complex but inclusive signatures to reduce the volume of data that is written to tape. The event is rapidly classified as a multihadron, a dilepton, etc., by analysis of the data from each subdetector, so that it is suitable for further physics analysis, and so software flags can be set into the data structure. Simultaneously, the filter discriminates against background events, thus reducing the volume of data that has to be processed in a more detailed manner. The filter is also used for monitoring the output, particularly in the form of event displays.

Finally, the data is processed by ROPE [49] (Reconstruction of OPal Events) which uses OPCAL [50], a calibration database. ROPE is an event reconstruction package which operates either on the raw data from OPAL, or on the data from the simulation program GOPAL [51](discussed later). ROPE's output contains all the information about the event. The reconstruction of tracks, clusters, etc. from the raw subdetector readouts are used to produce usable physics quantities like particle energy, momentum, particle identity, and so on. This data is then written onto the Data Summary Tapes (DST), and is available for physics analysis.

2.6 Simulation of the OPAL Detector

The characteristics of the detector, which include its dimensions and other properties, are used as inputs to the modelling package, GEANT [52]. Packages such as JETSET [53], KORALZ [54], and TAUOLA [55] create the various interaction products in the 'correct' proportions, and these particles are propagated through the detector with some local-environment probability of interaction. The signals from each detector are then simulated and incorporate the effects of resolution, noise and inefficiency.

This Monte Carlo simulation of OPAL events is known as GOPAL (Geant at OPAL), and the data produced is ROPE'd in the same way as genuine data. However, the Monte Carlo output incorporates information about the ‘true’ nature of the particles - i.e. one can later ‘cheat’ and check the efficiency and purity of the analysis.

Chapter 3

Selection of Geometrical Region

All of the analysis in this thesis occurs within a well-defined region of the barrel of the detector. The main selection of $\tau \to \mu\nu\bar{\nu}$ cones is made using the muon chambers, and so a region of the barrel is first defined in which the muon chambers are functioning well. For this analysis, a second $\tau \to \mu\nu\bar{\nu}$ sample is required, and this is obtained using primarily the hadron calorimeter. Thus, to keep systematic errors to a minimum, further cuts are made on this good muon chamber area to select the good acceptance region of the hadron calorimeter. After these considerations, the geometric region used for the whole analysis is defined, and it is a region in which both the muon chambers and the hadron calorimeter have high efficiency for muon detection. The details of the cuts involved in producing the acceptance region are given in the following sections. One further cut applied here is that upon the x_μ value of the track in each cone, where x_μ is given by

$$x_\mu \quad \equiv \quad \frac{(p_{trk} + E_{cls} - 0.5\mathrm{GeV})}{\mathrm{E_{beam}}}$$

where p_{trk} is the momentum of the track, E_{cls} is the energy of the E_{CAL} cluster associated to the track, E_{beam} is the beam energy, and the 0.5GeV is subtracted to account for the average deposition made by a minimum-ionising particle in the E_{CAL}. This quantity, x_μ, is required to be above 0.05 for all cones so that the ranging out of particles within the detector is not a problem.

3.1 Good Muon Chamber Region

The muon chambers provide good coverage throughout the barrel region, but the precise position of the detector supports requires investigation. To do this, the muon chamber algorithm (described in chapter 5) is used to select candidates both in data and Monte Carlo, and the geometric cut is made just inside any fall-off in efficiency. The geometric region chosen is slightly smaller than the default [56], since the acceptance was conservatively defined so as to minimize edge effects, but is basically very similar to the standard region used in the tau platform [56]. The geometric boundaries imposed then, are:

$$
\begin{aligned}
0^\circ \leq \phi_{mb} < 60^\circ &\quad and \quad |\cos\theta_{mb}| < 0.67 \\
60^\circ \leq \phi_{mb} < 125^\circ &\quad and \quad |\cos\theta_{mb}| < 0.48 \\
125^\circ \leq \phi_{mb} < 205^\circ &\quad and \quad |\cos\theta_{mb}| < 0.67 \\
205^\circ \leq \phi_{mb} < 237^\circ &\quad and \quad |\cos\theta_{mb}| < 0.61 \\
237^\circ \leq \phi_{mb} < 303^\circ &\quad and \quad |\cos\theta_{mb}| < 0.43 \\
303^\circ \leq \phi_{mb} < 342^\circ &\quad and \quad |\cos\theta_{mb}| < 0.61 \\
342^\circ \leq \phi_{mb} < 360^\circ &\quad and \quad |\cos\theta_{mb}| < 0.67
\end{aligned}
$$

where ϕ_{mb} and θ_{mb} are the extrapolated phi and theta of the charged track at the muon chambers

The main modification here is in the region $60^\circ \leq \phi_{mb} < 125^\circ$, where a relatively large contamination of mu-pairs was found. A plot of this is given in figure 3.1 below. The relatively high population of mu-pairs in this region is due to the nature of the mu-pair antiselection in the tau platform. The muon identification has to be made in each of the two cones for the event to be antiselected, and this region is 180° from the large lower support, which is equipped with neither hadron calorimetry nor muon chambers, and so registers the presence of muons with much reduced efficiency.

3.2 Good Hadron Calorimeter Region

The good hadron calorimeter region was defined in a similar way to that described above, this time using the H_{CAL} algorithm to determine the positions of reduced efficiency. Again, the exact locations of the detector supports were confirmed but additionally, two strips in phi had to be removed. This is because in these well-defined regions there are somewhat fewer (between three and six) H_{CAL} layers than the normal seven, and so detection efficiency is reduced. Also, efficiency is lower at the edges of each of the calorimeter sectors, so the outer degree of each of the fifteen-degrees-wide sectors is also removed. The cuts around the detector supports fall in the same place for the H_{CAL}, but the extra sector cuts applied are summarised as follows, the given regions being omitted from the acceptance:

$$0.06 < |\cos\theta_{hc}| < 0.15$$

$$|(\phi_{sec} - 15^\circ)| \leq 1^\circ$$

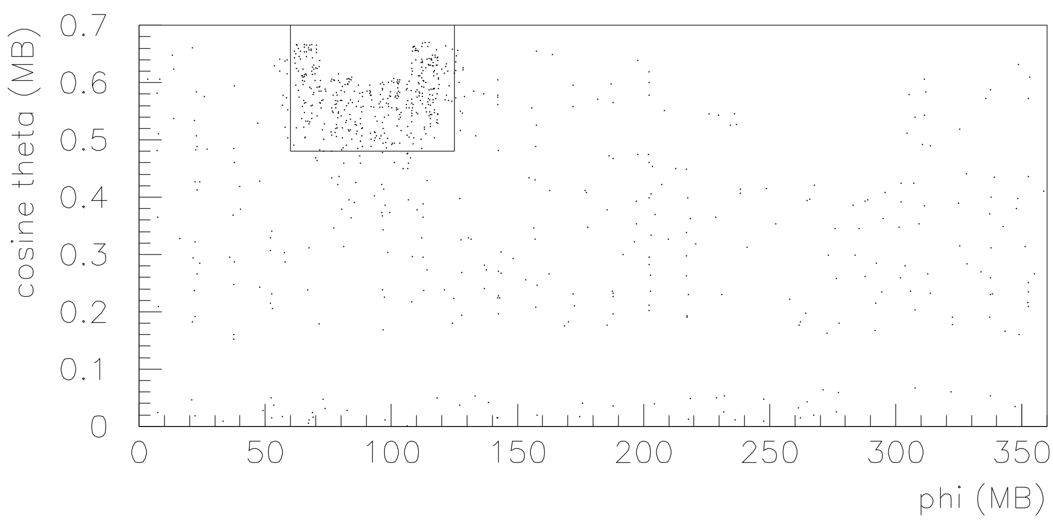

Figure 3.1: The plot shows cosine theta against phi (measured at the muon chambers, MB) for Monte Carlo mu-pairs, the outlined region being removed from the acceptance.

Where ϕ_{hc} and θ_{hc} are the phi and theta of the track at the hadron calorimeter, and ϕ_{sec} is mod $(\phi_{HC}, 15°)$.

3.3 Anode Planes

Straight tracks that pass near a CJ anode plane can sometimes be assigned a momentum that is too small, and a ϕ value that is incorrect. These effects are particularly significant for the mu-pair background in the tau-pair sample, because of the nature of one of the cuts used to separate out these mu-pairs. The lower reconstructed momentum for these 'anode plane' mu-pair events means that they are not rejected by the $0.6E_{\mathrm{CM}}$ energy cut described in section 4.3.2, and so the mu-pair contamination is very much higher in these regions. The Monte Carlo models this effect to some extent, but falls short of the required accuracy and so the anode plane regions are removed for this analysis.

As shown in figure 3.2, the effect of the anode planes in the data (shown as crosses) is far more pronounced than in the Monte carlo (represented by the shaded histogram). The very localised nature of the phenomenon allows the affected regions to be removed with the following cut:

$$|(\mathrm{mod}(\phi_{origin}, 15) - 7.5°)| < 0.3° \quad ,$$

where ϕ_{origin} is the value of phi at the origin of coordinates (defined in Section 2.2).

After all these geometric cuts are made, the final region in which all the analysis of this thesis occurs is shown in figure 3.3.

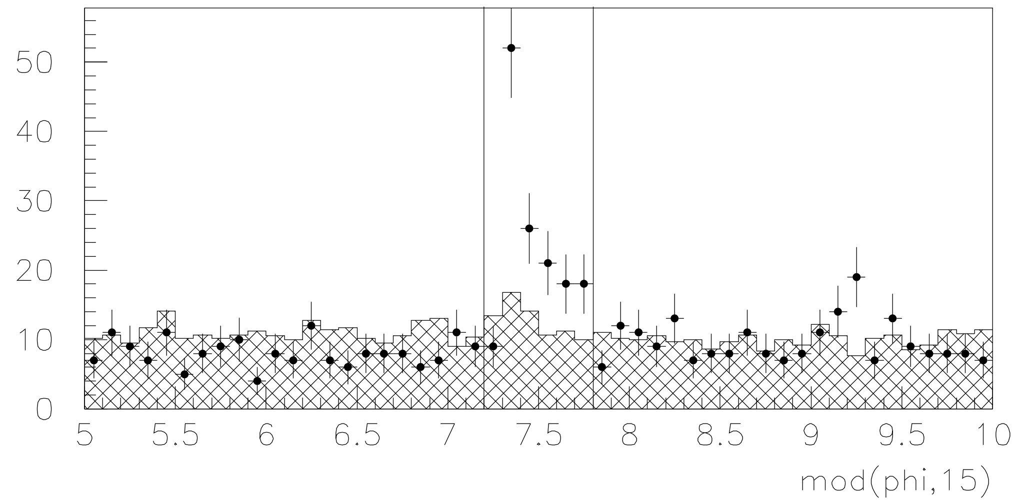

Figure 3.2: Mu-pairs around the anode plane, the x-axis labelled in units of mod $(\phi_{origin}, 15^{\circ})$ The points with error bars represent the data, and the mu-pair and tau-pair Monte Carlo samples are shown by the shaded histogram.

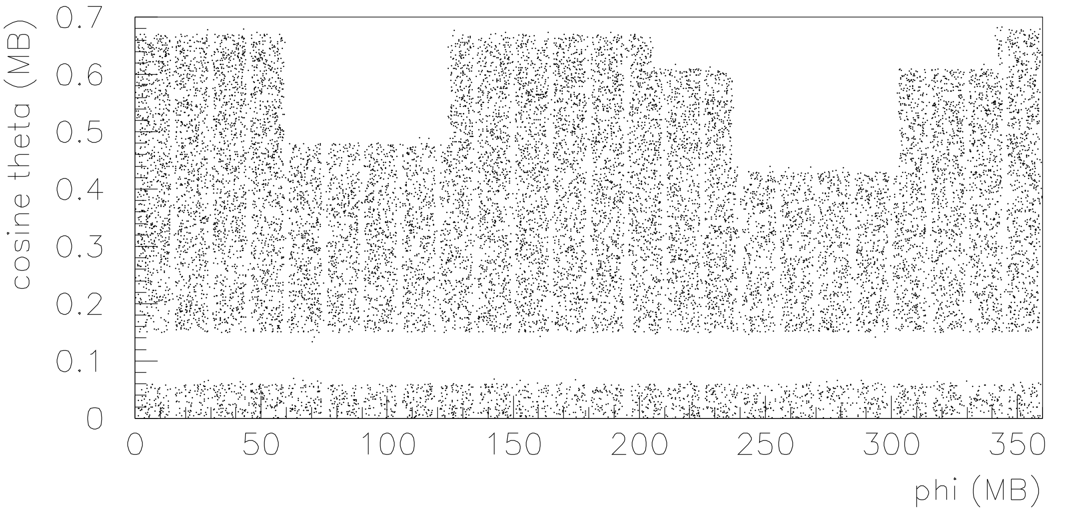

Figure 3.3: The fiducial region after all cuts. The phi and cosine theta used in this plot are measured at the muon chambers (MB).

Chapter 4

Selection of $e^+e^- \rightarrow \tau^+\tau^-$ Events

The selection of taupairs is done in three stages. Firstly, a broad requirement on the event having low multiplicity reduces the data volume considerably. Then, cuts are applied to suppress non-lepton pair background, and finally the mu-pair and bhabha events are antiselected, thus producing an unbiassed and reasonably pure sample of tau-pairs. Each of these stages are described in the following sections.

4.1 Low Multiplicity Selection

The multiplicity of an event is defined simply by the number of charged tracks therein, and is hence a very good discriminator between multihadronic events and lepton pair events, since the multiplicities of the multihadronic events are relatively very high at LEP energies. Between 1991 and 1994 inclusive (which is the range of data used for the analysis in this thesis), LEP was operated at approximately the Z^0 mass, and so the predicted proportions of each fermion-antifermion pair were as given in table 4.1.

The neutrino decays are essentially undetectable, and so the low multiplicity lepton pairs and the high multiplicity multihadron events are all that remain, and these are relatively simple to separate. The low-multiplicity sample is obtained by requiring that the number of tracks added to the number of electromagnetic calorimeter clusters is fewer than 18.

In addition to this low multiplicity requirement, demands are made upon the status of each of the subdetectors that play a role in this analysis, so that the data quality is consistent. Table 4.2 shows broadly how the data volume is reduced with the application of each selection.

4.2 Selection of lepton pairs

Because of the low multiplicity selection, most of the Z^0 products now present will be di-leptons. However, the high energies used at LEP mean that other less-favoured processes (such as two-photon lepton production described later) might still contribute significantly to the sample, and of course cosmic and beam-associated background events too will make a contribution and have to be excluded as much as possible. This 'fine tuning' of the low multiplicity sample is referred to as the *preselection* [56], and is now described in detail.

4.2.1 Good tracks and clusters

For this analysis, only good charged tracks and good electromagnetic clusters are used. A good charged track is defined by the following conditions:

- number of jet chamber wires hit, $N_{hit}^{CJ} \geq 20$
- transverse track momentum $p_t \geq 0.1$GeV
- distance of closest approach in xy plane $|d_0| \leq 2$cm

Decay	Proportion (%)
$Z^0 \rightarrow q\bar{q}$	69.90±0.15
$Z^0 \rightarrow \nu\bar{\nu}$	20.01±0.16
$Z^0 \rightarrow e^+e^-$	3.366±0.008
$Z^0 \rightarrow \mu^+\mu^-$	3.367±0.013
$Z^0 \rightarrow \tau^+\tau^-$	3.360±0.015

Table 4.1: Breakdown of Z^0 decays

- minimum separation in z between track and vertex, $|z_0| \leq 75$cm
- radius of innermost wire hit in jet chamber, $R_{min} \leq 75$cm

and a good cluster must satisfy:

- number of blocks within the cluster, $N_{blk} \geq 1$
- uncorrected electromagnetic cluster energy, $E_{cls}(raw) \geq 0.1$GeV

Only 'good' tracks and clusters are used in this analysis, and so in any further reference to tracks and clusters, these cuts are implicitly assumed.

4.2.2 Cone definition

The tau platform environment [56], in which this analysis was made, operates using structures called *cones*. Each cone is defined using a jet-finding algorithm which associates charged tracks and clusters that lie inside a cone of half-angle 35°. The cone is constructed by first considering the highest momentum track or highest energy cluster that is available, and searching outwards from this within the prescribed half-angle. If other tracks or clusters are found, then the direction of the one with the highest momentum or energy is added vectorially to the direction defined by the initial track or cluster, and this process of searching and adding is repeated from the new cone direction until no further activity is found. The highest energy track or cluster still unassociated with a cone is then the starting point for the next cone, and so on until all the tracks and clusters are associated to cones. If a cone contains no charged tracks then it is labelled a neutral cone, otherwise it is called a charged cone. If a cone contains more than 1% of the beam energy then it is additionally labelled as a good cone. For this analysis, each event must contain exactly two good charged cones.

4.2.3 Further multihadron rejection

Since the typical multiplicity of a tau event is so much lower than that of multihadronic events, it is worthwhile increasing the severity of the multiplicity cut that was applied initially. The multihadron background is reduced by demanding that

$$2 \leq N_{chrg}^{Tot} \leq 6 \tag{4.1}$$

$$N_{clust}^{Tot} \leq 10. \tag{4.2}$$

4.2.4 Two-photon event rejection

Two-photon events are so called because they occur when a photon is emitted from both the incident electron and incident positron, and these photons interact to form, for example, a pair of leptons. A schematic diagram of this process is shown in figure 4.1. The production rate of these two-photon events is inversely proportional to the

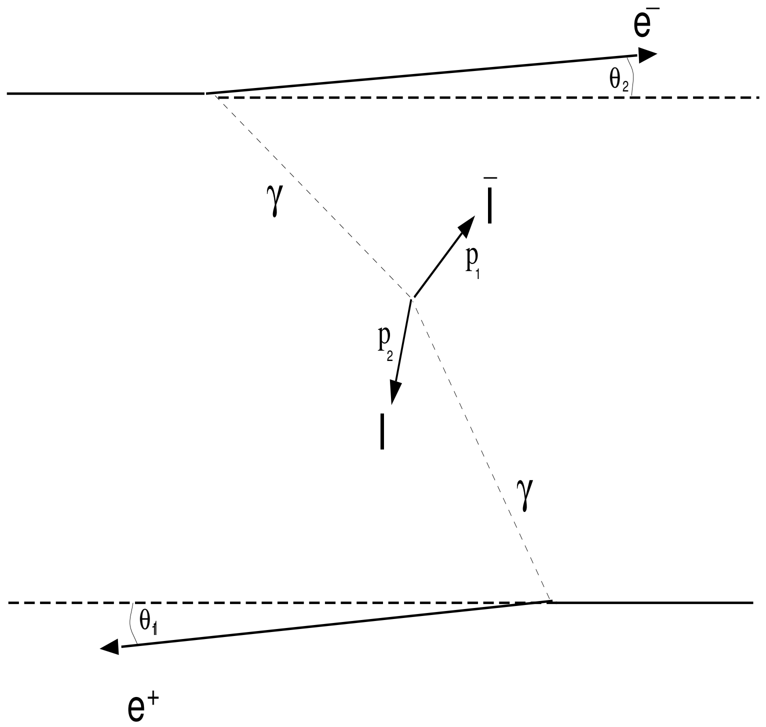

Figure 4.1: Schematic diagram showing a two-photon event.

angles θ_1 and θ_2, and so for the majority of the events of this type that are seen in the detector, the electron and positron are deviated only slightly and continue down the beam pipe. The photons produced are not usually of equal momentum, and so the resulting reaction products are not constrained to be back-to-back and will often be highly acollinear. This fact is exploited to discriminate against two-photon events because, of course, the lepton pairs produced from the Z^0 decay are for the most part collinear. The cut applied then, is an upper limit on the acollinearity of the two cone directions, θ_{acol}. Using the labels from the diagram (figure 4.1), this is:

$$\theta_{acol} \equiv \cos^{-1}\left(-\frac{\mathbf{p_1}\cdot\mathbf{p_2}}{|\mathbf{p_1}||\mathbf{p_2}|}\right) < 15^\circ$$

Another characteristic of these events is that the visible energy of both cones will be small. The visible energy is defined to be the maximum of either the scalar sum of the track momenta, summed over both cones, or the total cluster energy, summed over both cones. To further reduce two-photon background then, it is required that

$$E_{vis} \equiv \sum_{cone} Max(E_{cls}, p_{trk}) \geq 0.03\ E_{\mathrm{CM}}$$

If the visible energy is above this threshold, but still quite low (less than 20% of the centre of mass energy) then a cut is made on the net transverse momentum of the charged tracks and clusters in the cones. Thus, if

$$E_{vis} \leq 0.20 E_{\mathrm{CM}}$$

then events are only accepted if

$$p_t(cls) \geq 2\mathrm{GeV} \quad \mathrm{OR} \quad p_t(trk) \geq 2\mathrm{GeV}$$

where $p_t(cls)$ is the total transverse cluster energy in the event, and $p_t(trk)$ is the total transverse track momentum in the event.

4.2.5 Rejection of Cosmic Ray Background

The distinguishing feature of cosmic ray events is their position within the detector. Events resulting from e^+e^- collisions usually possess characteristics that strongly indicate that they originated from a point very close to the interaction region. Cosmic events however, occur uniformly throughout the detector, and can be heavily suppressed by applying constraints on the reconstructed position of each event's point of origin. It is required that an event satisfies:

$$\begin{aligned} |d_0|_{min} &\leq 0.5\mathrm{cm} \\ |z_0|_{min} &\leq 20\mathrm{cm} \\ |z_{0,ave}| &\leq 20\mathrm{cm} \end{aligned}$$

where $|d_0|_{min}$ is the minimum $|d_0|$, $|z_0|_{min}$ is the minimum $|z_0|$ of tracks in the event, and $|z_{0,ave}|$ is the mean z_0 of tracks with $|z_0|_{min} \leq 20$cm.

In addition to this, it is required that at least one of the TOF (Time Of Flight) counters receives a signal within 10ns of the time a signal would be expected if the event took place at the origin. Similarly, the event is only accepted if at least one pair of TOF counters that are separated by at least 165°, receive a signal within 10ns of each other.

4.3 Isolating the Tau-pairs

The majority of the events passing the preselection will be tau-pairs, mu-pairs, or bhabha events. These three behave sufficiently differently that they can be fairly cleanly separated, and the desired tau sample can be obtained with reasonable purity. This process of isolation is described in the following sections.

4.3.1 Antiselecting Bhabhas

The electromagnetic calorimeter is very effective at absorbing electrons, and so we expect that the energy deposited by bhabha events will be very much greater than that deposited by either tau-pairs or mu-pairs. If we look at the cluster energy (normalised to the centre of mass energy) summed over all the E_{CAL} clusters in the event, E^{clus}_{sum}, then it is very clear that bhabha events can be cleanly distinguished from mu-pair events. However, if we also use the fact that mu-pairs and bhabhas will generally comprise two back-to-back tracks in CJ whose momenta sum to approximately the beam energy, then separation between bhabhas and tau-pairs may also be achieved. This is because the tau decays very close to the collision point, into one, three, or five charged particles, each having different total track momentum and total E_{CAL} cluster characteristics, but generally having less extreme values than either the mu-pairs or the bhabhas. The normalised track momentum, summed over all the tracks in the event, E^{trak}_{sum}, is also defined then, so that

$$E^{clus}_{sum} \equiv \sum_i E_i^{\mathrm{CLUST}} / E_{\mathrm{CM}}$$

$$E_{sum}^{trak} \equiv \sum_j E_j^{\mathrm{TRACK}} / E_{\mathrm{CM}}$$

and events are classified as bhabhas and rejected if

$$E_{sum}^{clus} > 0.8 \quad \mathbf{AND} \quad E_{sum}^{clus} + 0.3 E_{sum}^{trak} > 1.0 \ ,$$

This bhabha cut is shown in figure 4.2.

4.3.2 Antiselecting Mu-pairs

As seen in figure 4.2, mupairs are characterised by a high momentum track in each cone, and by low energy-deposition in the electromagnetic calorimeter. The anti-selection of mu-pairs then, begins with the identification of a muon in both of the cones. In order to retain a very high efficiency, this identification can be made by either the E_{CAL} or the H_{CAL} or the muon chambers, and so requires that both cones satisfy at least one of the following requirements, designated ECAL, HCAL and MUON:

- Identification by the electromagnetic calorimeter [ECAL]:

  $$E_{cls} < 2.0\mathrm{GeV}$$

  where E_{cls} is the total electromagnetic cluster energy in the cone.

- Identification by the hadron calorimeter [HCAL]:

  $$N_{\mathrm{hits/layer}}^{\mathrm{HCAL}} < 2.0 \quad \mathbf{AND} \quad N_{layers}^{\mathrm{HCAL}} \geq 4 \quad \mathbf{AND} \quad N_{last3}^{\mathrm{HCAL}} \geq 1$$

  where $N_{\mathrm{hits/layer}}^{\mathrm{HCAL}}$ is the number of hits per hit layer in the HCAL, $N_{layers}^{\mathrm{HCAL}}$ is the number of HCAL layers hit and $N_{last3}^{\mathrm{HCAL}}$ is the number of layers hit in the last three active layers of the HCAL.

- Identification by the four muon chamber layers [MUON]:

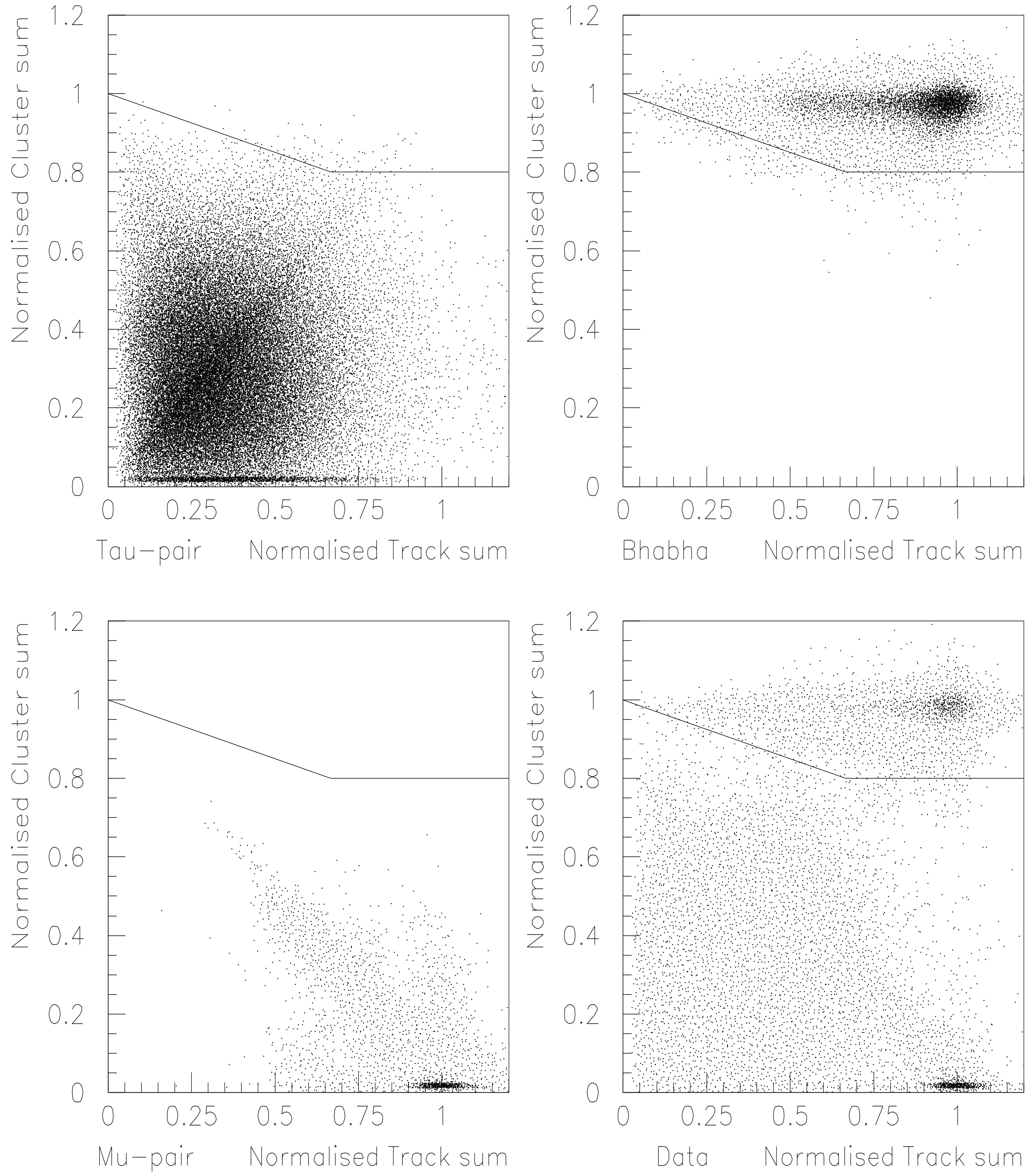

Figure 4.2: The three 1994 di-lepton Monte Carlo samples are shown, along with the that for the 1994 data. The solid line indicates where the bhabha cut (described in the text) is applied.

Data Year	Initial Number of Events	No. events passing Low Muliplicity Selection	No. events passing preselection	Number of taus in my geometry region
94	2447143	1474899	72183	48782
93	1007043	692974	30928	20759
91-92	1591242	1102675	47285	31201

Table 4.2: Table showing the number of events in each year at each stage of the selection process

$$N^{\mathrm{MU}}_{layers} \geq 2$$

where N^{MU}_{layers} is the number of layers hit in the muon chambers (MB and ME).

In addition to this muon-identification requirement on both cones, it is necessary to apply a cut that will retain events in which both taus have decayed to muons, but still reject mu-pair events. This is achieved by cutting on the sum of the highest momentum track (normalised to the centre of mass energy) and the normalised highest energy cluster, summed over both cones and labelled E_{total}. The double $\tau \to \mu\nu\bar{\nu}$ decay will generally have a lower value of E_{total}, since some proportion of the energy of the event is carried away by the four neutrinos. The threshold is set at 0.6, and events with E_{total} greater than this, that have a muon identified in each cone, are classed as mu-pair events and are rejected from the sample. As we can see from figure 4.3, the tau-pairs and mu-pairs can be well-separated with a cut on this variable.

The events remaining in the sample after all of these cuts should predominantly be tau-pairs. There is, of course, some contamination from the other sources mentioned, and the determination of the extent of this contamination is the subject of section 4.5. Table 4.2 shows the for each year the number of data events at each stage of the tau selection process used in this thesis.

4.4 Smearing of the Monte Carlo

In this thesis, all of the Monte Carlo used is smeared using the standard tau platform smearing routines, described in [59]. The smearing parameters vary according to Monte Carlo run number, and are dependent upon the reciprocal of the track momentum (normalised to the beam energy), and upon the electromagnetic cluster energy (determined using electrons). In the previous OPAL muonic branching fraction analysis [58] different smearing was used which depended directly upon the track momentum, and applied simply a numerical correction factor to the electromagnetic cluster energies.

4.5 Background in the Taupair Sample

The level of contamination in the τ pair sample is first estimated from Monte Carlo, then adjusted using data control samples. The data control samples are chosen to represent as faithfully as possible the background events present in the tau sample. This optimisation involves simply using data from kinematic regions either within or adjacent to the discriminatory tau platform cuts, so that the resultant events have properties similar to the actual background. One large difference between this study and previous ones [57] [58] is that regions close to the CJ anode planes are excluded from the final acceptance, and so the mu-pair contamination is very much lower, and is better modelled by Monte Carlo. This was discussed in detail in section 3.3.

In the following sections, each of the main tau sample backgrounds are assessed first by Monte Carlo, and then this prediction is tested using data control samples. The tables in Appendix B show the method employed for drawing these comparisons. Each Monte Carlo sample (e.g. muon pairs) is passed through the selection described, and then scaled to match the integrated luminosity of the data. The predicted number of events that are not mu-pairs are then subtracted from the data control sample, and the final number of candidates in the data is compared with the Monte Carlo prediction for the number of mu-pairs. The ratio of these two quantities is taken as the scaling factor for the particular source of tau sample background, and this factor is then multiplied into the predicted background level to give the final estimate. The error on the multiplicative factor is taken as either the statistical error on the ratio, or as half the deviation from unity of the ratio, whichever is the greater.

The taupair background is assessed separately for each year, but only the 1994 samples are discussed here in the text. The uncorrected and data-corrected background compositions for each year are given in table 4.3, and are discussed later in this section.

$e^+e^- \rightarrow \mu^+\mu^-$

The selection cuts used to study this background are very similar to those used to anti-select mu-pairs in the preselection. A muon has to be identified in both cones by at least one of the E_{CAL} or the H_{CAL} or the muon chamber selections, and E_{total} has to lie between 0.6 and 0.75 E_{CM}. The upper limit on this variable is applied in order to ensure that the mu-pair candidates selected are as similar as possible to those that form the mupair background in the tau sample. The background predicted by Monte Carlo is (0.105 $\pm$0.007)%. A comparison of Monte Carlo with data control sample (see table B.1 in Appendix B, and figure 4.3) yields

$$\frac{\mathrm{DATA}(\mathrm{e}^+\mathrm{e}^- \rightarrow \mu^+\mu^-)}{\mathrm{MC}(\mathrm{e}^+\mathrm{e}^- \rightarrow \mu^+\mu^-)} = 1.651 \pm 0.239$$

So the mu-pair background becomes:

$$(0.105 \pm 0.007)(1.651 \pm 0.326) \quad = \quad (0.175 \pm 0.036)\%.$$

$e^+e^- \rightarrow q\bar{q}$

The modelling of the multihadronic background was tested with a study of higher-multiplicity events, since there are more multihadrons than taus in this category. The multiplicity cut in the preselection (see section 4.2.3) was increased from six charged tracks to eight, and the events with topologies of 2-4, 2-6, 3-4 or 4-4 were selected from the tau-pair sample in order to enhance the multihadron content and suppress the tau-pairs). The predicted background is (1.128 $\pm$0.006)%. Comparing data and Monte Carlo (see table B.2 in Appendix B) gives:

$$\frac{\mathrm{DATA}(\mathrm{e}^+\mathrm{e}^- \rightarrow \mathrm{q}\bar{\mathrm{q}})}{\mathrm{MC}(\mathrm{e}^+\mathrm{e}^- \rightarrow \mathrm{q}\bar{\mathrm{q}})} = 0.489 \pm 0.048$$

And so the final background estimate is:

$$(1.128 \pm 0.006)(0.489 \pm 0.256) \quad = \quad (0.554 \pm 0.291)\%.$$

$\boldsymbol{e^+e^- \longrightarrow (e^+e^-)\mu^+\mu^-}$

A sample of two-photon muons is isolated by first rejecting events identified as lepton-pairs by the preselection, and then requiring the following:

- The acollinearity of the two cones lies between 15° and 25°.
- $x_\mu \; < \; 0.2$ in each cone.
- $dE/dx \; < \; 8.5keV/cm$ for the track in each cone.

From Monte Carlo, the background is (0.057 ±0.005)%. The correction factor from comparison with data (see table B.3 in Appendix B) and figure 4.4) is:

$$\frac{\mathrm{DATA}(\mathrm{e^+e^-} \rightarrow (\mathrm{e^+e^-})\mu^+\mu^-)}{\mathrm{MC}(\mathrm{e^+e^-} \rightarrow (\mathrm{e^+e^-})\mu^+\mu^-)} = 1.251 \pm 0.090$$

and so the background estimate becomes:

$$(0.057 \pm 0.005)(1.251 \pm 0.126)\% \quad = \quad (0.072 \pm 0.009)\%.$$

$\boldsymbol{e^+e^- \longrightarrow (e^+e^-)e^+e^-}$

A sample of two-photon electrons is obtained in a similar manner, but this time the rate of energy loss is assigned a minimum rather than a maximum value:

$dE/dx \; > \; 9.5keV/cm$ for the track in each cone.

From Monte Carlo, the background is (0.094 ±0.007)%. The correction factor from comparison with data (see table B.4 in Appendix B and figure 4.5) is:

$$\frac{\mathrm{DATA}(\mathrm{e^+e^-} \rightarrow (\mathrm{e^+e^-})\mathrm{e^+e^-})}{\mathrm{MC}(\mathrm{e^+e^-} \rightarrow (\mathrm{e^+e^-})\mathrm{e^+e^-})} = 0.928 \pm 0.053$$

and so the background estimate becomes:

$$(0.094 \pm 0.007)(0.928 \pm 0.053)\% \quad = \quad (0.088 \pm 0.008)\%.$$

$e^+e^- \rightarrow e^+e^-$

The bhabha background was studied using a sample very similar to that selected as electron pairs by the preselection. In this case however, the normalised total cluster energy, E^{clus}_{sum} (see section 4.3.1), is constrained to lie between 0.7 and 0.9, thus straddling the tau pair cut-off, and representing the bhabha events that are present in the tau sample.

From Monte Carlo, the background is (0.221 ±0.014)%. The correction factor from comparison with data (see table B.5 in Appendix B and figure 4.6) is:

$$\frac{\mathrm{DATA}(\mathrm{e^+e^-} \rightarrow \mathrm{e^+e^-})}{\mathrm{MC}(\mathrm{e^+e^-} \rightarrow \mathrm{e^+e^-})} = 0.899 \pm 0.028$$

and so the background estimate becomes:

$$(0.221 \pm 0.014)(0.899 \pm 0.051)\% \quad = \quad (0.120 \pm 0.017)\%.$$

After all of these adjustments, the overall background in the τ pair sample changes from $(1.605 \pm 0.061)\%$ to $(1.088 \pm 0.294)\%$ for the 1994 data. The predicted and corrected measurements of the tau sample composition are summarised for each year in table 4.3. The main backgrounds are the mu-pairs, the bhabhas and the multihadrons, each prediction showing fluctuations between the years but remaining broadly consistent. The one exception is in the case of the 1994 multihadron prediction, which is very much higher than in other years. The reason for this is not precisely known, but the root cause is at generator level and so not easily correctable. The correction factors for each of the backgrounds vary considerably for each year, but are within approximately 2σ of each other and so are considered to be consistent. There are variations in the predicted and corrected background levels from year to year, but the data corrections bring them closer into agreement. The data-corrected tau sample backgrounds for 1993 and 1994 are consistent, but they differ from the 1991-92 figure by 1.6σ and 3.9σ respectively. The reason for these discrepancies must lie with the different decay-modelling used to generate each year's Monte Carlo samples, as the analysis for each year was performed using exactly the same code. Since for each year, these Monte Carlo samples are used not only in assessing the tau-pair background, but also to calculate other quantities used in finding the branching fraction, it is only a comparison of each year's final branching ratio that will indicate the true effect of yearly differences. This is discussed further in chapter 7.

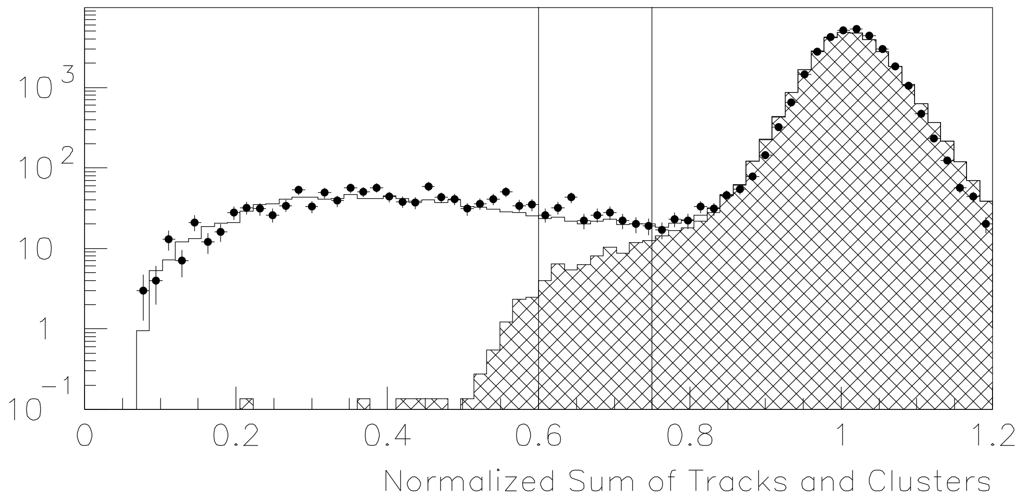

Figure 4.3: Control sample for checking mupair background in 1994 tau sample. In this plot and in the following plots, the same code is used for the shading of the histograms. The data is represented by points with error bars, the tau-pair Monte Carlo is given by an unshaded region, and all other Monte Carlos (predominantly the one under study) are represented by the shaded histogram

Background	Monte Carlo Predicted Contamination(%)	Correction Factor	Corrected Contamination(%)
	1991-92		
$e^+e^- \to \mu^+\mu^-$	0.085 $\pm$0.009	0.930 $\pm$0.282	0.079 $\pm$0.025
$e^+e^- \to q\bar{q}$	0.192 $\pm$0.026	1.381 $\pm$0.248	0.265 $\pm$0.060
$e^+e^- \to (e^+e^-)\mu^+\mu^-$	0.035 $\pm$0.009	1.158 $\pm$0.122	0.041 $\pm$0.011
$e^+e^- \to (e^+e^-)e^+e^-$	0.050 $\pm$0.016	1.118 $\pm$0.103	0.055 $\pm$0.014
$e^+e^- \to e^+e^-$	0.099 $\pm$0.022	1.600 $\pm$0.300	0.158 $\pm$0.046
Total	0.460 $\pm$ 0.038		0.597 $\pm$ 0.082
	1993		
$e^+e^- \to \mu^+\mu^-$	0.121 $\pm$0.012	2.615 $\pm$0.807	0.315 $\pm$0.102
$e^+e^- \to q\bar{q}$	0.189 $\pm$0.038	1.579 $\pm$0.309	0.296 $\pm$0.083
$e^+e^- \to (e^+e^-)\mu^+\mu^-$	0.051 $\pm$0.004	1.294 $\pm$0.149	0.066 $\pm$0.009
$e^+e^- \to (e^+e^-)e^+e^-$	0.091 $\pm$0.006	1.335 $\pm$0.168	0.121 $\pm$0.017
$e^+e^- \to e^+e^-$	0.204 $\pm$0.019	2.074 $\pm$0.537	0.420 $\pm$0.116
Total	0.655 $\pm$ 0.045		1.217 $\pm$ 0.176
	1994		
$e^+e^- \to \mu^+\mu^-$	0.105 $\pm$0.007	1.651 $\pm$0.326	0.175 $\pm$0.036
$e^+e^- \to q\bar{q}$	1.128 $\pm$0.058	0.489 $\pm$0.256	0.554 $\pm$0.291
$e^+e^- \to (e^+e^-)\mu^+\mu^-$	0.057 $\pm$0.005	1.251 $\pm$0.126	0.072 $\pm$0.009
$e^+e^- \to (e^+e^-)e^+e^-$	0.094 $\pm$0.007	0.928 $\pm$0.053	0.088 $\pm$0.008
$e^+e^- \to e^+e^-$	0.221 $\pm$0.014	0.899 $\pm$0.050	0.120 $\pm$0.017
Total	1.605 $\pm$ 0.061		1.088 $\pm$ 0.294

Table 4.3: Estimated background fractions in the selected τ pair candidate events before and after applying corrections using systematic studies discussed in the text.

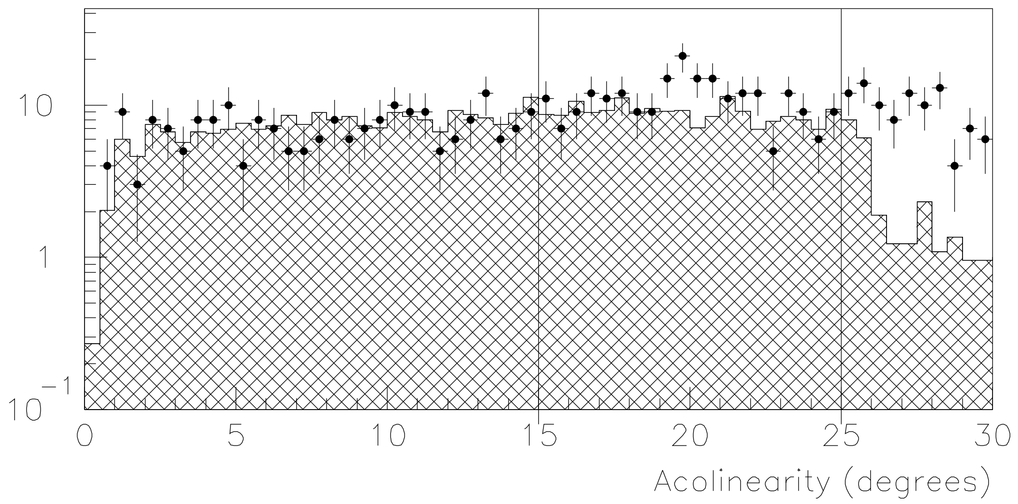

Figure 4.4: Control sample for checking two-photon muon-pair background in 1994 tau sample. The fall-off in Monte Carlo after 26 degrees in this figure and in figure 4.5 is due to a cut applied in generation.

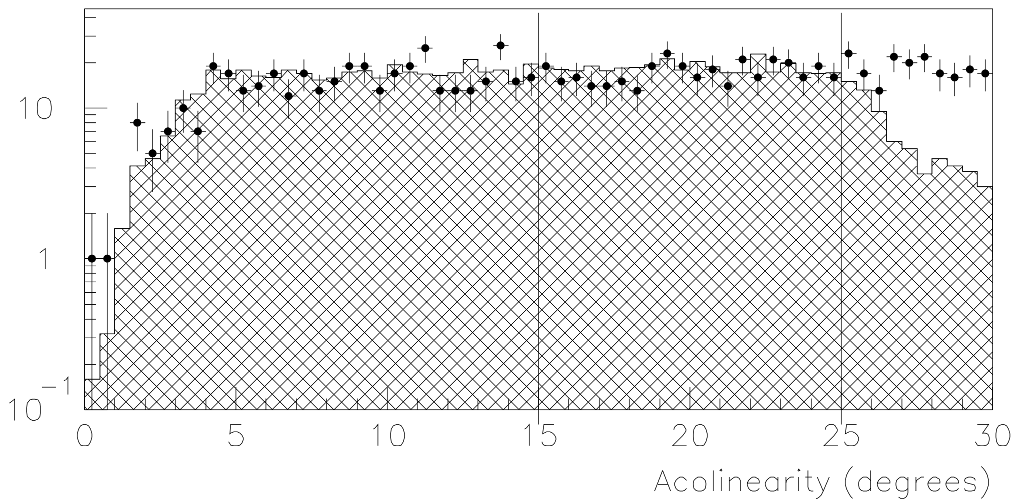

Figure 4.5: Control sample for checking two-photon electron-pair background in 1994 tau sample.

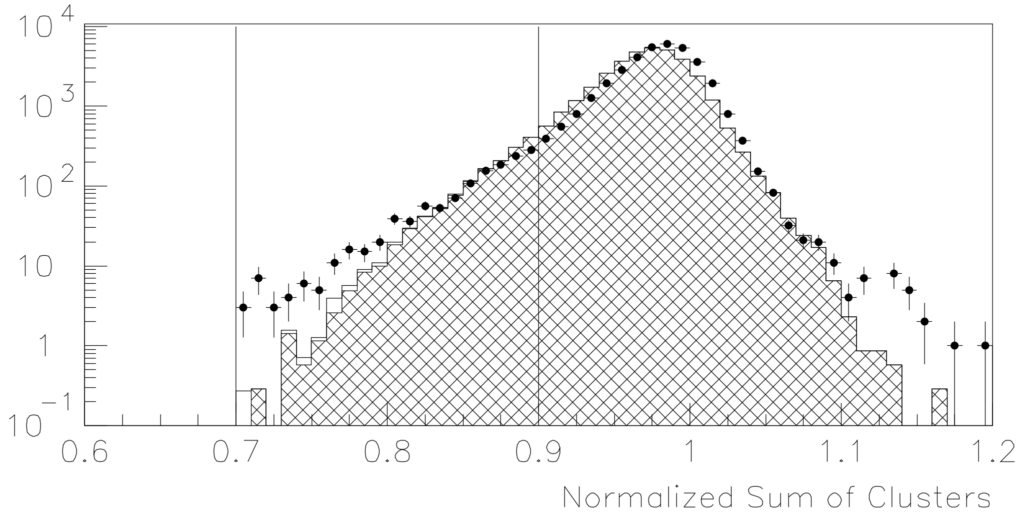

Figure 4.6: Control sample for checking bhabha background in 1994 tau sample.

Chapter 5

Selection of $\tau \to \mu\nu\bar{\nu}$

Once the fiducial region is defined, it is necessary to make further cuts to isolate the $\tau \to \mu\nu\bar{\nu}$ decay from other tau decays and from background in the tau sample. In this chapter, the $\tau \to \mu\nu\bar{\nu}$ selection is described in detail, and plots are shown of all the variables upon which cuts are made, all the other selection cuts having been applied. For each plot, the following code is employed: the data are represented as points with error bars; the $\tau \to \mu\nu\bar{\nu}$ Monte Carlo signal is represented by a solid, unshaded region; and the sum of the Monte Carlo backgrounds are represented by a cross-hatched histogram. All the Monte Carlo samples are normalised to the integrated data luminosity, and all the data (1991-1994) and all the Monte Carlo (1992, 1993 and 1994 runs) are used in the formation of the plots, and for the analysis overall. Exactly the same code was used to process the samples from each year, thus ensuring equal treatment. Table 5.1 shows the Monte Carlos used, along with the number of events in each sample.

5.1 The selection

After the geometrical acceptance is defined, further cuts are made to isolate the $\tau \to \mu\nu\bar{\nu}$ decays and these are detailed below. Much use is made of the tau platform 'cones', which are used to associate tracks and clusters. The formation of these cones is described in Section 4.2.2 and in the Tau Platform Manual [56]. This analysis requires that all events have exactly two good charged cones.

Monte Carlo	Run Number	Number of Events
	1992	
Tau-pair	1508	200K
Mu-pair	1602	200K
Bhabha	1308	100K
Two-photon muon	1703	50K
Two-photon electron	1702	50K
multihadron	1108	1000K
	1993	
Tau-pair	1513	300K
Mu-pair	1607	200K
Bhabha	1311	394K
Two-photon muon	1716	400K
Two-photon electron	1717	400K
multihadron	2291	1000K
	1994	
Tau-pair	1520	600K
Mu-pair	1620	600K
Bhabha	1320	400K
Two-photon muon	1745	400K
Two-photon electron	1746	400K
multihadron	2790/1	2000K

Table 5.1: Run numbers and number of events for all the Monte Carlo samples used in this analysis.

- The number N_{chrg} of charged tracks assigned to the candidate cone must satisfy:

$$N_{chrg} = 1$$

Figure 5.1 shows that this is a reasonable cut, a large fraction of the rejected material being background.

- The chi-squared value of the matching between the position of muon chamber hits and extrapolated jet-chamber tracks must satisfy:

$$\chi^2 \leq 3.0$$

The χ^2 distributions for data and Monte Carlo are shown in figure 5.2. There is reasonable agreement between these distributions and the branching ratio measurement is very stable with respect to changes in this cut.

- In order to suppress mu-pair background, a cut on a momentum variable is included. It is required that both cones in the event must satisfy $x_\mu < 0.9$, where x_μ is defined in chapter 3. Figure 5.3 shows the x_μ distribution of the nearside cone when the farside cone has $x_\mu < 0.9$.

5.2 Estimate of Background Contamination in $\tau \to \mu\nu\bar{\nu}$ sample

The background level of around 2% predicted by Monte Carlo changes slightly with each year's samples but is very consistent from year to year (see table 5.2). The dominant contribution to this background is from hadronic τ decays, but mu-pairs and two-photon muons are also present at a lower level. Again, this initial Monte Carlo estimate has to be checked with control samples from the data, and this procedure is described in the following sections. Plots are shown for each of the control samples in which the data are represented as points with error bars; the $\tau \to \mu\nu\bar{\nu}$ Monte Carlo signal is represented by a solid, unshaded region; and the sum of all the Monte Carlo backgrounds is represented by a cross-hatched histogram. In each case, the Monte Carlo samples are normalised to the integrated data luminosity.

Background	Monte Carlo Predicted Contamination (%)	Data-Corrected Contamination (%)
	1991-92	
$\tau \to \pi(\mathrm{K})\nu$	0.84	1.12
$\tau \to \rho\nu$	0.80	1.07
$e^+e^- \to \mu^+\mu^-$	0.17	0.17
$e^+e^- \to (e^+e^-)\mu^+\mu^-$	0.282	0.285
Total	2.101 ± 0.082	2.654 ± 0.144
	1993	
$\tau \to \pi(\mathrm{K})\nu$	0.70	0.90
$\tau \to \rho\nu$	0.77	1.00
$e^+e^- \to \mu^+\mu^-$	0.13	0.13
$e^+e^- \to (e^+e^-)\mu^+\mu^-$	0.275	0.284
Total	1.876 ± 0.078	2.315 ± 0.449
	1994	
$\tau \to \pi(\mathrm{K})\nu$	0.87	1.14
$\tau \to \rho\nu$	0.74	0.98
$e^+e^- \to \mu^+\mu^-$	0.13	0.12
$e^+e^- \to (e^+e^-)\mu^+\mu^-$	0.257	0.253
Total	1.98 ± 0.04	2.481 ± 0.273

Table 5.2: Estimated backgrounds in the selected $\tau \to \mu\nu\bar{\nu}$ candidate events before and after applying corrections using systematic studies discussed in the text.

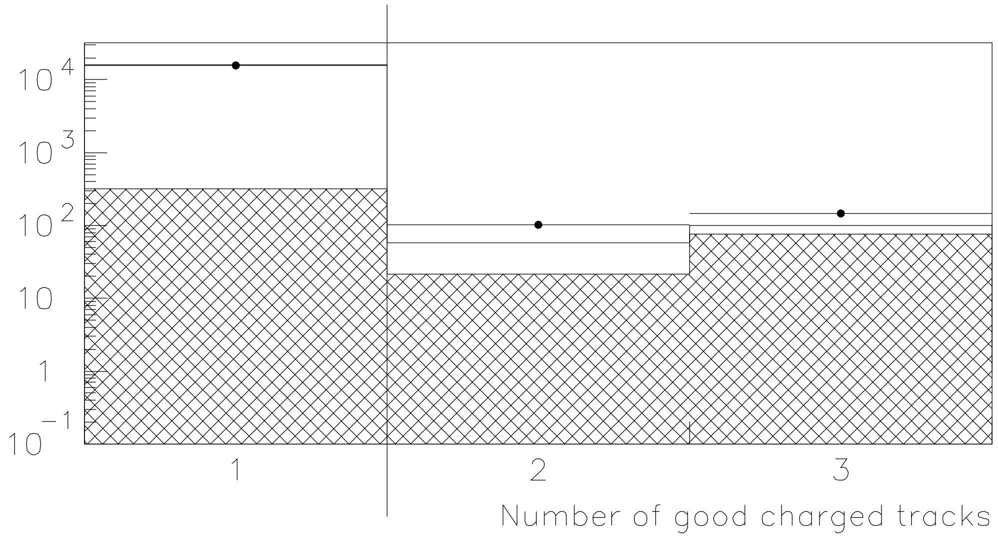

Figure 5.1: Number of charged tracks for cones that pass the muon chamber selection (logarithmic scale). As usual, the data is represented by points with error bars, the tau-pair Monte Carlo is shown by the unshaded region, and the sum of the Monte Carlo backgrounds are represented by the shaded histogram.

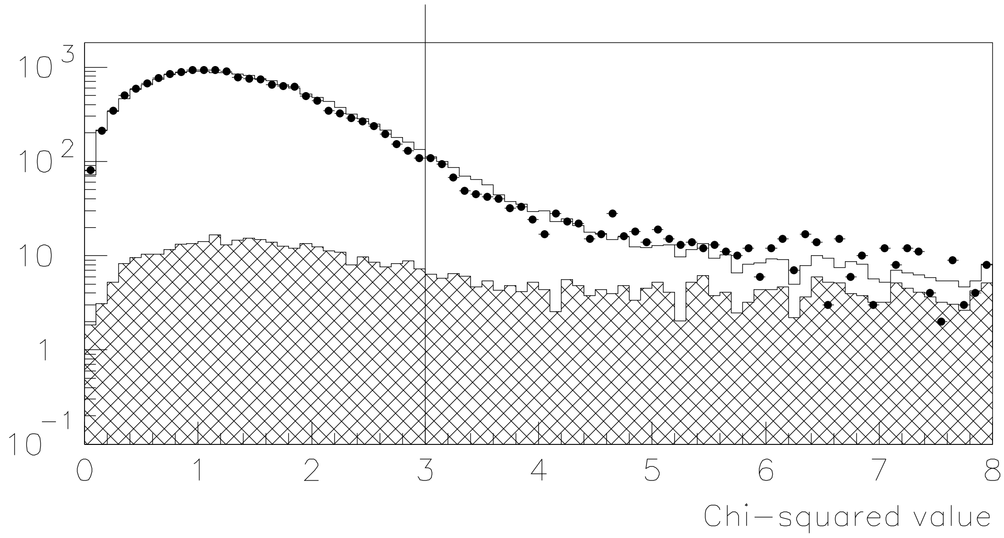

Figure 5.2: The χ^2 value of the position match between extrapolated tracks and hits in the muon chambers (logarithmic scale).

5.2.1 Hadronic Tau Decays

To evaluate the contribution to the background of this type of tau decay, the tau platform rho-recognition algorithm, TPROID [56] is used, together with a requirement on the minimum number of E_{CAL} blocks in the highest-energy cluster in the cone (there must be more than ten). This algorithm is based upon H_{CAL} and E_{CAL} variables and so is independent of the muon-chamber-based $\tau \rightarrow \mu\nu\bar{\nu}$ selection. The additional requirement on the primary electromagnetic cluster further reduces the very small muon background in the $\tau \rightarrow$ hadrons sample. The predicted composition of the selected sample is shown in table 5.3, and is fairly consistent year-to-year. The sample mainly consists of pions, the decays into kaons being present at the level of a few percent. This reflects the background obtained by applying the muon chamber selection, as the hadronic decay background is dominated by pions, with kaons contributing less than 10%.

A comparison of each year's data and Monte Carlo rho samples in terms of the ratio of cones passed by the muon chamber algorithm yields:

$$\frac{\mathrm{DATA}(\tau \rightarrow \mathrm{hadrons})}{\mathrm{MC}(\tau \rightarrow \mathrm{hadrons})} = 1.33 \pm 0.23 \qquad \text{for 1994 data}$$

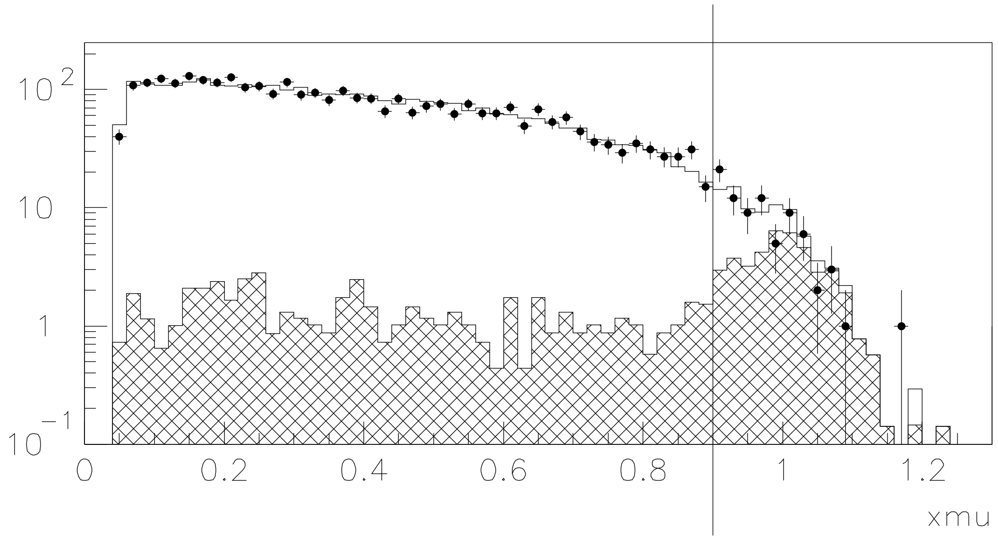

Figure 5.3: The distribution of x_μ for the near-side cones passing the muon chamber selection, given that the opposite cone has $x_\mu > 0.9$ (logarithmic scale).

Background	Monte Carlo proportions(%)		
	1991-2	1993	1994
$\tau \to \mu\nu\bar{\nu}$	0.10±0.02	0.08±0.02	0.12±0.02
$\tau \to \pi\nu$	22.32±0.29	19.70±0.28	20.14±0.20
$\tau \to \rho\nu$	72.81±0.31	75.36±0.30	74.92±0.22
$\tau \to \mathrm{K}\nu$	0.25±0.04	0.17± 0.03	0.19± 0.02
$\tau \to \mathrm{K}^*\nu$	2.43±0.04	1.94± 0.10	1.98± 0.07
$\tau \to$ *other*	2.09 ±0.10	2.75 ±0.11	2.65 ± 0.08

Table 5.3: Composition of the $\tau \to$ hadrons selection, estimated with each year's Monte Carlo

$$\frac{\mathrm{DATA}(\tau \to \mathrm{hadrons})}{\mathrm{MC}(\tau \to \mathrm{hadrons})} = 1.30 \pm 0.39 \qquad \text{for 1993 data}$$
$$\frac{\mathrm{DATA}(\tau \to \mathrm{hadrons})}{\mathrm{MC}(\tau \to \mathrm{hadrons})} = 1.34 \pm 0.28 \qquad \text{for } 1991-2 \text{ data}$$

Thus the predicted backgrounds are augmented by these factors, and the statistical error on the correction is incorporated. As before, if the statistical error of the correction is less than half the deviation of the central value from unity, then this latter quantity is taken as the error. The Monte Carlo backgrounds and data-adjusted levels can be see in table 5.2.

$e^+e^- \to \mu^+\mu^-$

A sample of mu-pairs is obtained by making a cut on the overall energy of the event, and muon identification cuts on the opposite cone (i.e. the cone in the event that is not under study). The following selections are made:

- The sum over both cones of the highest energy track, and the highest energy cluster must be greater than 0.7 E_{CM}.
- The cones must be highly collinear: $\theta_{acol} \leq 0.4^\circ$

- The opposite cone must be recognized as a muon by one of the three detectors, ECAL, HCAL or MUON, as described in section 4.3.2.

- The value of x_μ for the opposite track must exceed 0.8.

A comparison of the muon-chamber algorithm acting on each year's data and Monte carlo samples yields:

$$\frac{\mathrm{DATA}(e^+e^- \to \mu^+\mu^-)}{\mathrm{MC}(e^+e^- \to \mu^+\mu^-)} = 0.978 \pm 0.002 \qquad \text{for 1994 data}$$
$$\frac{\mathrm{DATA}(e^+e^- \to \mu^+\mu^-)}{\mathrm{MC}(e^+e^- \to \mu^+\mu^-)} = 0.999 \pm 0.008 \qquad \text{for 1993 data}$$
$$\frac{\mathrm{DATA}(e^+e^- \to \mu^+\mu^-)}{\mathrm{MC}(e^+e^- \to \mu^+\mu^-)} = 1.009 \pm 0.003 \qquad \text{for } 1991-2 \text{ data}$$

$e^+e^- \to (e^+e^-)\mu^+\mu^-$

To assess this background, the taupair preselection was removed, and lepton-pair events were antiselected using the standard tau platform cuts described in Section 4.3. In addition to this, the following requirements were made:

- Each cone has one good charged track.

- Acolinearity $\theta_{acol} > 10^\circ$.

- Both cones have $x_\mu < 0.5$

- The opposite cone satisfies muon identification (see section 5.1), with muon matching $\chi^2 \leq 3.0$

Comparing the ratio of each year's data and Monte Carlo passing the muon chamber selection, it is found that:

$$\frac{\mathrm{DATA}(e^+e^- \to (e^+e^-)\mu^+\mu^-)}{\mathrm{MC}(e^+e^- \to (e^+e^-)\mu^+\mu^-)} = 0.989 \pm 0.008 \qquad \text{for 1994 data}$$
$$\frac{\mathrm{DATA}(e^+e^- \to (e^+e^-)\mu^+\mu^-)}{\mathrm{MC}(e^+e^- \to (e^+e^-)\mu^+\mu^-)} = 1.036 \pm 0.012 \qquad \text{for 1993 data}$$
$$\frac{\mathrm{DATA}(e^+e^- \to (e^+e^-)\mu^+\mu^-)}{\mathrm{MC}(e^+e^- \to (e^+e^-)\mu^+\mu^-)} = 1.016 \pm 0.015 \qquad \text{for } 1991-2 \text{ data}$$

Having now defined a sample of tau-pairs, and from them a sample of $\tau \rightarrow \mu\nu\bar{\nu}$ decays, and having quantitatively investigated the backgrounds present in each sample, it is now necessary to examine in detail the efficiency of the Monte Carlo. This is dealt with in chapter 6.

Chapter 6

Efficiency Correction

The efficiency of the muon chamber $\tau \to \mu\nu\bar{\nu}$ selection is initially estimated from Monte Carlo, but has to be checked using control samples from the data. Since the $\tau \to \mu\nu\bar{\nu}$ selection utilises only the muon chambers and the tracking chambers, largely independent control samples of good purity and efficiency can be selected with the calorimeters and the tracking chambers to evaluate the performance of the Monte Carlo. In the previous OPAL analysis [58], the main selection relied upon most of the subdetectors, and so it was much more difficult to isolate such independent control samples to measure the selection efficiency from the data itself. The resulting error on the efficiency estimate dominated the systematic uncertainty and was the major contributor to the overall error on the final result.

6.1 E_{CAL}/H_{CAL} Selection

A largely independent sample of $\tau \to \mu\nu\bar{\nu}$ decays (E_{CAL}/H_{CAL} selection) is derived in the following manner:

- The number N_{chrg} of good charged tracks assigned to the candidate cone must satisfy:

  $$N_{chrg} = 1 \, .$$

  Figure 6.1 shows that this is a good discriminator between signal and background.

- Muons are expected to penetrate deeply into the H_{CAL}, so a hit in the outermost three active H_{CAL} layers is made a requirement:

$$N^{\mathrm{HCAL}}_{last3} \quad \geq \quad 1$$

Figure 6.2 shows that background is significantly reduced with this cut.

- The muon passes through the H_{CAL} causing only very few hits per layer. Hadrons, however, frequently interact in the H_{CAL}, so a cut on the average number of hits per hit H_{CAL} layer reduces this background. Figure 6.3 shows how quickly the muon level falls off as the number of hits per hit layer rises.

$$N^{\mathrm{HCAL}}_{\mathrm{hits/layer}} \quad < \quad 3.$$

- Muons leave little energy in the E_{CAL} and so a cut on the energy of the cluster associated to the track, E_{cls}, is also included. Candidates must satisfy:

$$E_{cls} \quad < \quad 1.5\ \mathrm{GeV}$$

See figure 6.4.

- Some residual background from hadronic τ decays including a π^0 is suppressed by requiring

$$M_{trk-Ecal} \quad < \quad 0.3\ \mathrm{GeV}$$

where $M_{trk-Ecal}$ is the invariant mass of the charged track (assuming a $\pi^{\pm}$ hypothesis) and all E_{CAL} clusters in the cone (assuming a γ hypothesis). In the calculation, 0.5 GeV is subtracted from the energy of the E_{CAL} cluster associated to the charged track, to account for the average energy deposition expected from a minimum-ionising particle. Figure 6.5 shows how this mass distribution is strongly peaked at the pion mass, but also how the hump of the $\tau \to \rho\nu$ background is well-separated.

- To ensure that the momentum spectrum of this control sample of $\tau \to \mu\nu\bar{\nu}$ decays resembles as closely as possible that produced by the main selection, the same mupair rejection cut is applied so that an event is rejected if $x_{\mu} < 0.9$ for both cones. Figure 6.6 shows the x_{μ} distribution for the nearside cone when the opposite cone has $x_{\mu} > 0.9$.

	Monte Carlo Predicted Contamination(%)		
Background	1991-92	1993	1994
$\tau \rightarrow \pi(\mathrm{K})\nu$	1.05	1.05	0.87
$\tau \rightarrow \rho\nu$	0.01	0.02	0.01
$e^+e^- \rightarrow \mu^+\mu^-$	0.17	0.13	0.13
$e^+e^- \rightarrow (e^+e^-)\mu^+\mu^-$	0.27	0.27	0.26
Total	1.50±0.09	1.47±0.07	1.28±0.05

Table 6.1: Composition of the H_{CAL}/E_{CAL} selection of $\tau \rightarrow \mu\nu\bar{\nu}$ cones, predicted by Monte Carlo.

The predicted composition of the independent $\tau \rightarrow \mu\nu\bar{\nu}$ data control sample, identified with the E_{CAL} and H_{CAL} subdetectors, is given in table 6.1.

The predicted background is somewhat lower for this sample (mainly because of the rho-rejection provided by the cut on invariant mass) and the efficiency of selection is similar to that of the muon chamber selection. Nevertheless, the muon chambers are chosen to provide the main measurement because their performance is much simpler to model, and consequently a lower associated systematic error can be achieved.

6.2 Selection Efficiency

Using Monte Carlo information, the efficiency of a selection is defined as the identified fraction of the available muonic tau decays. However, it is important to check this efficiency with control data samples to correct the Monte Carlo figure where necessary. The calculation of the error on this correction is non-trivial however, since some of the numbers used in the calculation are also used in other parts of the branching ratio formula. In the following sections the procedure for evaluating the corrected selection efficiency is described in some detail, as it is in this area that the systematic error is significantly reduced with respect to the published OPAL

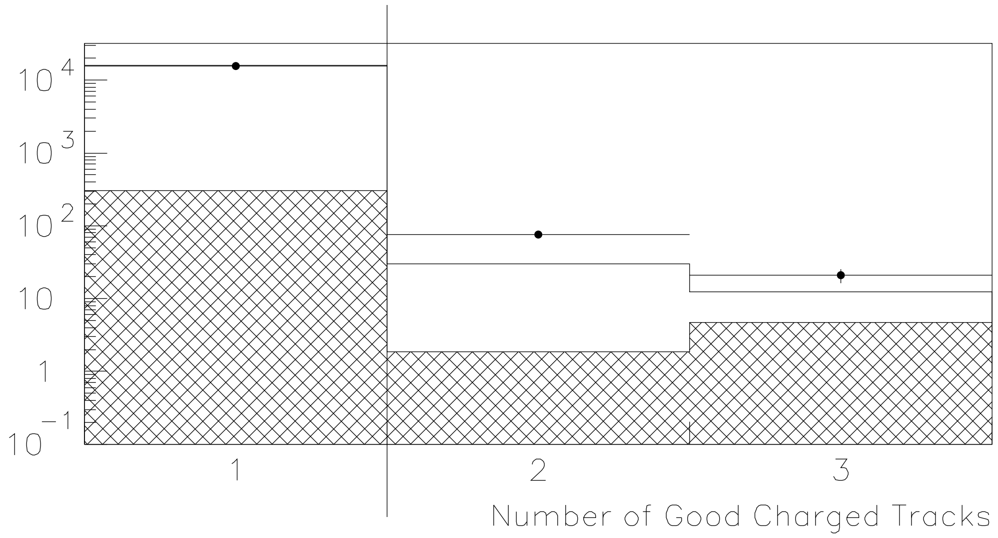

Figure 6.1: The number of tracks in cones that pass the H_{CAL} selection. The data is represented by points with error bars, the tau-pair Monte Carlo appears as the unshaded region, and the sum of the background Monte Carlos is represented by the shaded histogram.

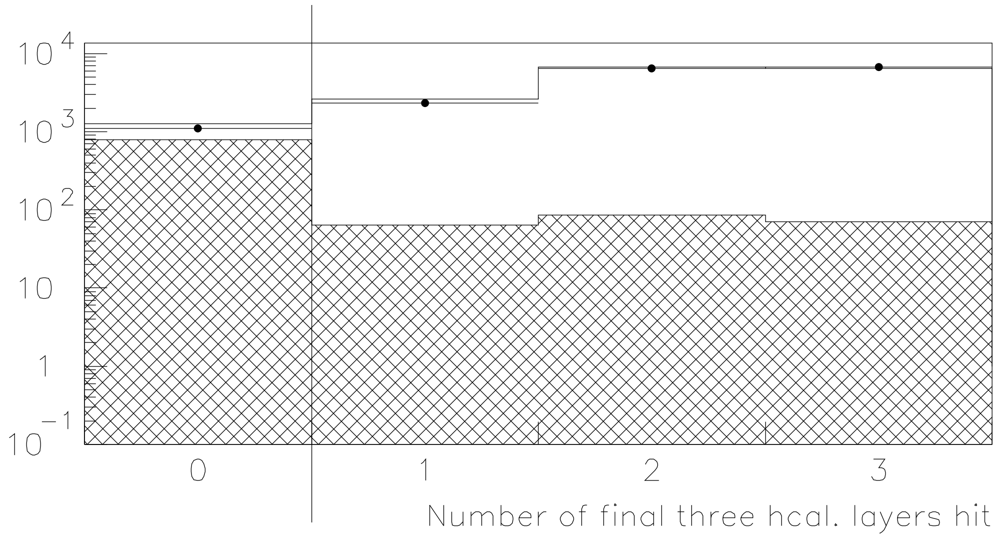

Figure 6.2: The number of hits registered in the last three active layers of the H_{CAL} in cones passing the H_{CAL} selection.

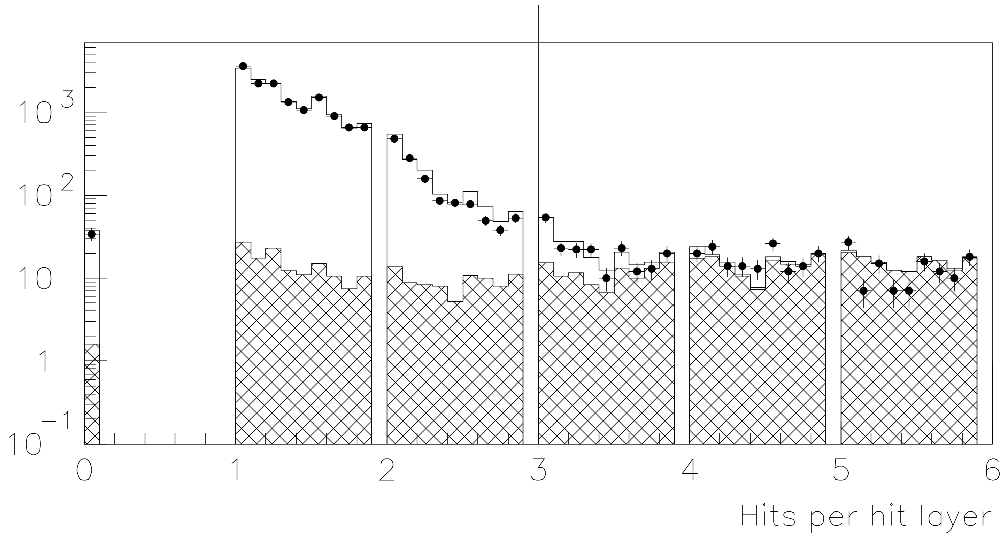

Figure 6.3: The mean number of hits per hit H_{CAL} layer for cones passing the H_{CAL} selection. The cyclic structure of the plot occurs because we are plotting a base-9 quantity (the number of H_{CAL} layers) on a base-10 scale.

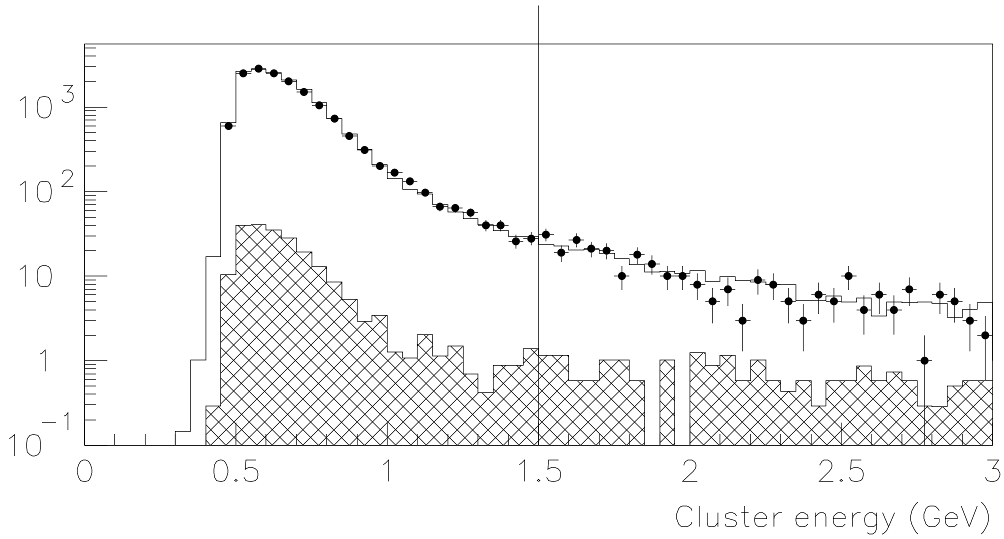

Figure 6.4: The energy (in GeV) of the E_{CAL} cluster associated to the track for cones passing the H_{CAL} selection.

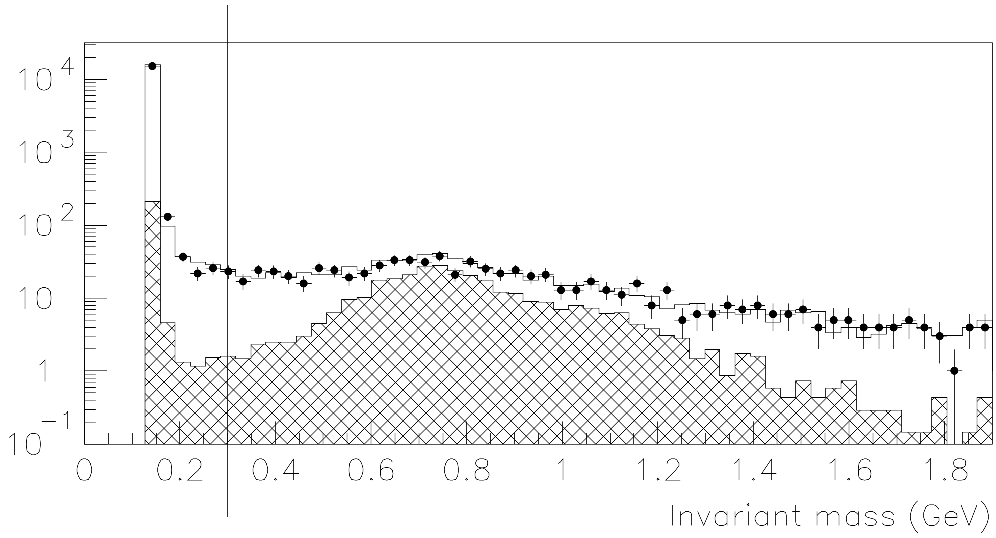

Figure 6.5: The invariant mass (in GeV) of the charged track (assuming a $\pi^{\pm}$ hypothesis) and all ECAL clusters in the cone (assuming a γ hypothesis) for cones passing the H_{CAL} selection.

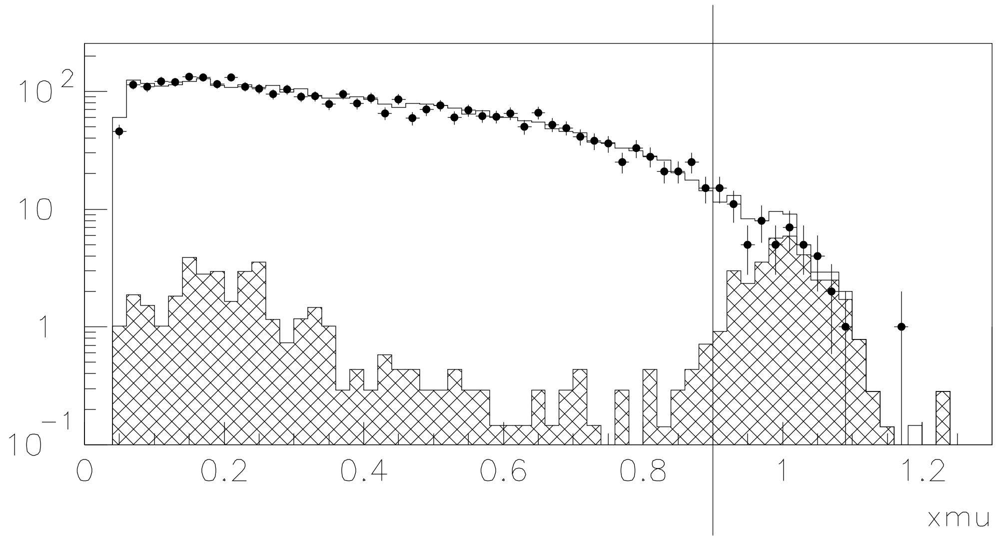

Figure 6.6: The distribution of x_{μ} for the near-side cones passing the H_{CAL} selection, given that the opposite cone has $x_{\mu} > 0.9$.

$\tau \rightarrow \mu\nu\bar{\nu}$ result [58]. The application of the correction and the calculation of its error are discussed in detail in appendix A.

6.3 Correcting The Efficiency

The correction to the efficiency is made by applying the H_{CAL} selection to data and Monte Carlo, and treating each as being an equally pure sample of $\tau \rightarrow \mu\nu\bar{\nu}$. These samples are then passed through the muon chamber selection and the resulting efficiencies in data and Monte Carlo are compared, and a correction factor is derived.

The correction factor, C_{eff}, is given by:

$$C_{\text{eff}} = \frac{\left[\frac{\text{Number of cones passing muon chamber and H}_{\text{CAL}}\text{ selections}}{\text{Number of cones passing H}_{\text{CAL}}\text{ selection}}\right]^{\text{Data}}}{\left[\frac{\text{Number of cones passing muon chamber and H}_{\text{CAL}}\text{ selections}}{\text{Number of cones passing H}_{\text{CAL}}\text{ selection}}\right]^{\text{MC}}}$$

Since the correction is made using a sample of $\tau \rightarrow \mu\nu\bar{\nu}$ decays, it automatically has the correct weighting according to momentum. A number of checks were made to ensure that this method is sound. Firstly, to check that the background in the H_{CAL}/E_{CAL} sample is sufficiently well modelled by Monte Carlo, several of the cuts were relaxed a little in order to increase the predicted background and observe the effect on the branching ratio. For the 1994 data and Monte Carlo, the H_{CAL}/E_{CAL} cuts were relaxed and the predicted background of the sample increased from 1.28% to 2.16%. This caused the branching ratio to increase slightly from (17.637)% to (17.639)%, an absolute change of 0.002. Since the cuts had to be moved considerably to allow in this extra background, and since the resulting error is much smaller than any of the other sources of (systematic) error, we assume that the Monte Carlo modelling is satisfactory and assign no further uncertainty.

In addition, the momentum distributions for each selection in data and Monte Carlo were compared, since bad agreement will not only affect the momentum weighting of the efficiency correction but might also indicate simulation problems. To be able to use a global efficiency-correction factor, it is necessary that both of the two selections used in this analysis produce a sample of $\tau \rightarrow \mu\nu\bar{\nu}$ candidates with very similar momentum distributions, since it is this that ensures the weighting

	91-92	93	94
MC efficiency (%)	86.53 ± 0.20	88.97 ± 0.18	90.92 ± 0.12
Correction factor	1.035 ± 0.015	1.020 ± 0.017	0.9834 ± 0.0110
Corrected efficiency (%)	89.54 ± 1.28	90.78 ± 1.56	89.41 ± 1.01

Table 6.2: Correction factors and selection efficiencies (%) for the selection of $\tau \to \mu\nu\bar{\nu}$.

of the correction is appropriate. This was investigated by studying the number of candidates passing the muon chamber selection divided by the number of candidates passing the H_{CAL}/E_{CAL} selection as a function of momentum. The resulting distributions are shown in figures 6.7 and 6.8. We see immediately that the muon chamber selection outperforms the E_{CAL}/H_{CAL} selection at high x_μ and that this is reversed at low momentum for both data and Monte carlo. Reasons for this are discussed further in the next section (6.3.1). We see from these plots that in the mid-range of x_μ, where the population of tau decays is the highest, the performances of the two selections are closely-matched.

Table 6.2 shows for each year of Monte Carlo the predicted efficiency, the correction factor applied, and the final corrected value of the efficiency used to calculate the branching ratio. It is reassuring to note that the efficiency is consistently corrected to a value of around 90%, the required correction factor becoming closer to unity with each year's improvements in Monte Carlo simulation.

6.3.1 Independence of the Muon Chamber and the H_{CAL}/E_{CAL} Selections.

It is expected that a sample of $\tau \to \mu\nu\bar{\nu}$ decays obtained using just the muon chambers, and a sample obtained using other subdetectors, would be largely independent. If this is the case, then the product of the efficiency of each sample should simply be equal to the efficiency obtained by applying both selections simultaneously, *i.e.*

$$\text{eff}_{both} = (\text{eff}_{m-chamb}) \times (\text{eff}_{hadcal})$$

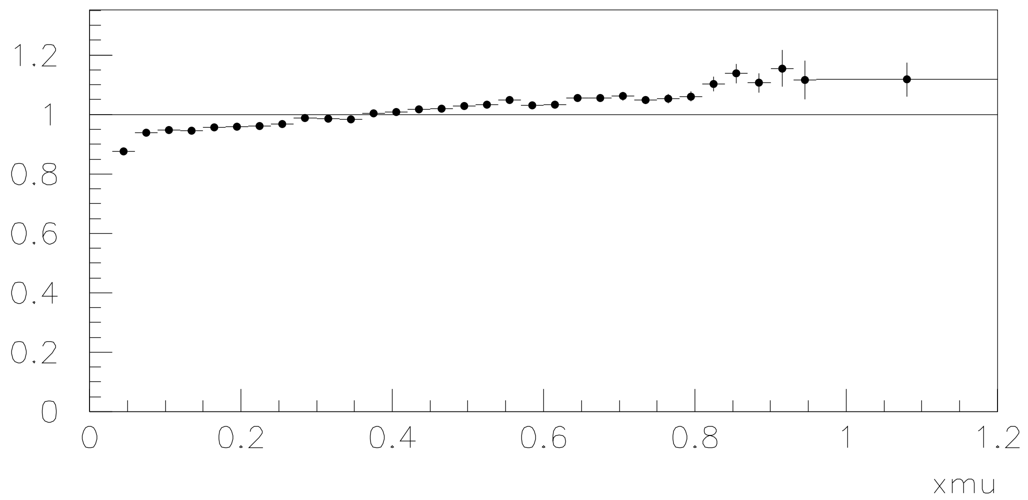

Figure 6.7: Muon chamber selection divided by H_{CAL}/E_{CAL} selection for Monte Carlo.

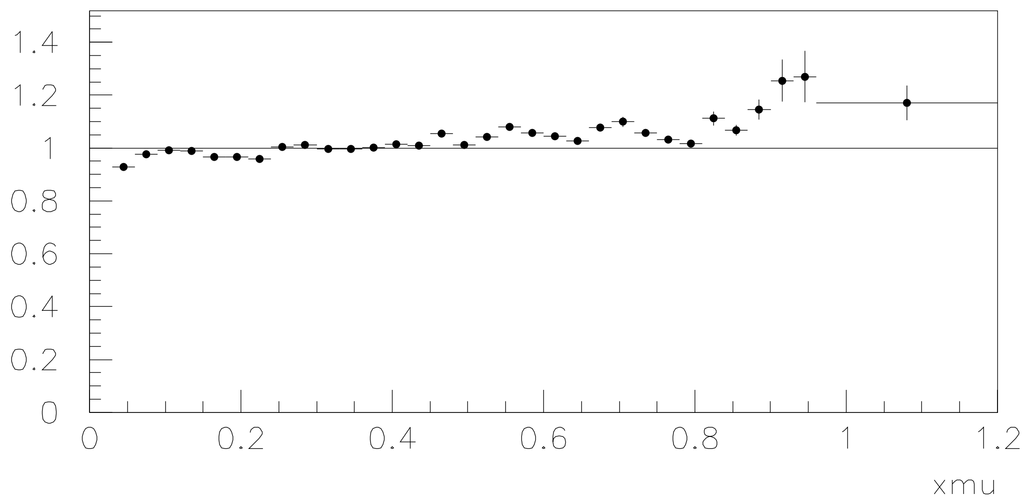

Figure 6.8: Muon chamber selection divided by H_{CAL}/E_{CAL} selection for data.

Where eff_{both} is the Monte Carlo efficiency for selecting $\tau \to \mu\nu\bar{\nu}$ using *both* algorithms; $\text{eff}_{m-chamb}$ is the MC efficiency using just the muon chamber selection; and eff_{hadcal} is the MC efficiency using the H_{CAL}/E_{CAL} selection. Any correlation is assessed by calculating a ratio, F_{corr}, defined as:

$$F_{\text{corr}} = \frac{\text{eff}_{both}}{(\text{eff}_{m-chamb}) \times (\text{eff}_{hadcal})}$$

From the equation above, we expect this to be unity if the selections are indeed independent.

Data and Monte Carlo samples of mu-pairs and two-photon muon pairs are used to study this correlation at the two extremes of the momentum spectrum, and the tau-pair Monte Carlo is used to sample the full momentum range. For the mu-pair samples, the x_μ cut (included only to remove mu-pairs from the $\tau \to \mu\nu\bar{\nu}$ sample) is removed from each selection so that statistics are greater. The results of this study are shown in table 6.3. There is good agreement between the correlation found in data and Monte Carlo, and the results show a correlation of around 1%, which is within 2σ of unity for the majority of the samples.

However, it should be noted that for both data and Monte Carlo, the muon chamber selection is more efficient at detecting mu-pairs, and the H_{CAL}/E_{CAL} selection is more efficient at detecting two-photon muons. These effects are explained as follows. The muon pairs, having high momentum, have a higher probability of radiating photons. These photons are detected in the E_{CAL} and cause the cone to fail the minimum-E_{CAL}-deposition cut. The smaller discrepancy seen at low momentum can be attributed to the thicker tail of the chi-squared distribution. An examination of the percentage of Monte Carlo $\tau \to \mu\nu\bar{\nu}$ decays that fail the chi-squared cut, for high ($x_\mu > 0.9$) and low ($x_\mu < 0.08$) momentum tracks yielded the following results:

$$\begin{aligned} (10.3 \pm 1.0)\% &\quad \text{for high momentum} \\ (13.0 \pm 0.6)\% &\quad \text{for low momentum} \;\; . \end{aligned}$$

This discrepancy between muons at either end of the momentum spectrum is of the right order to explain the observed differences in the selection efficiencies, and so the 'anomalies' are explained.

		Candidates passing (efficiency%)			
Source	Initial	Muon	H_{CAL}	Muon *and* H_{CAL}	Correlation factor
			1991-92		
τ pair MC	30399	26304 (86.5)	27498 (90.5)	24081 (79.2)	1.0121 ± 0.0052
Mu-pair data	22746	20048 (88.1)	19324 (85.0)	17224 (75.7)	1.0113 ± 0.0059
Mu-pair MC	86921	75943 (87.4)	74511 (85.7)	65533 (75.4)	1.0067 ± 0.0030
2-γ muon data	1474	1302 (88.3)	1364 (92.5)	1240 (84.1)	1.0292 ± 0.0257
2-γ muon MC	1308	1137 (86.9)	1240 (94.8)	1090 (83.3)	1.0112 ± 0.0259
			1993		
τ pair MC	29773	26490 (89.0)	26672 (89.6)	23965 (80.5)	1.0099 ± 0.0053
Mu-pair data	13125	11802 (89.9)	11291 (86.0)	10249 (78.1)	1.0095 ± 0.0079
Mu-pair MC	88650	79818 (90.0)	75873 (85.6)	68686 (77.5)	1.0055 ± 0.0030
2-γ muon data	778	709 (91.1)	721 (92.7)	672 (86.4)	1.0228 ± 0.0352
2-γ muon MC	9970	8774 (88.0)	9359 (93.9)	8305 (83.3)	1.0083 ± 0.0093
			1994		
τ pair MC	120369	107525 (89.3)	107770 (89.5)	97401 (80.9)	1.0117 ± 0.0027
Mu-pair data	33795	30324 (89.7)	28968 (85.7)	26261 (77.7)	1.0103 ± 0.0049
Mu-pair MC	259043	237581 (91.7)	220877 (85.3)	203956 (78.7)	1.0068 ± 0.0018
2-γ muon data	2189	1940 (88.6)	2012 (91.9)	1837 (83.9)	1.0302 ± 0.0211
2-γ muon MC	11578	10374 (89.6)	10876 (93.9)	9849 (85.1)	1.0107 ± 0.0088

Table 6.3: The efficiencies for and correlation factors between the two $\tau \to \mu\nu\bar{\nu}$ selections for several sources.

Despite these effects, we conclude that the efficiency correction (which would be affected by any difference in correlation factor between data and Monte Carlo) can be reliably determined, and no additional systematic is necessary. A plot of the correlation factor calculated in bins of momentum, is shown in figure 6.9, and the method employed to evaluate the error on the correlation factor is detailed in appendix A.

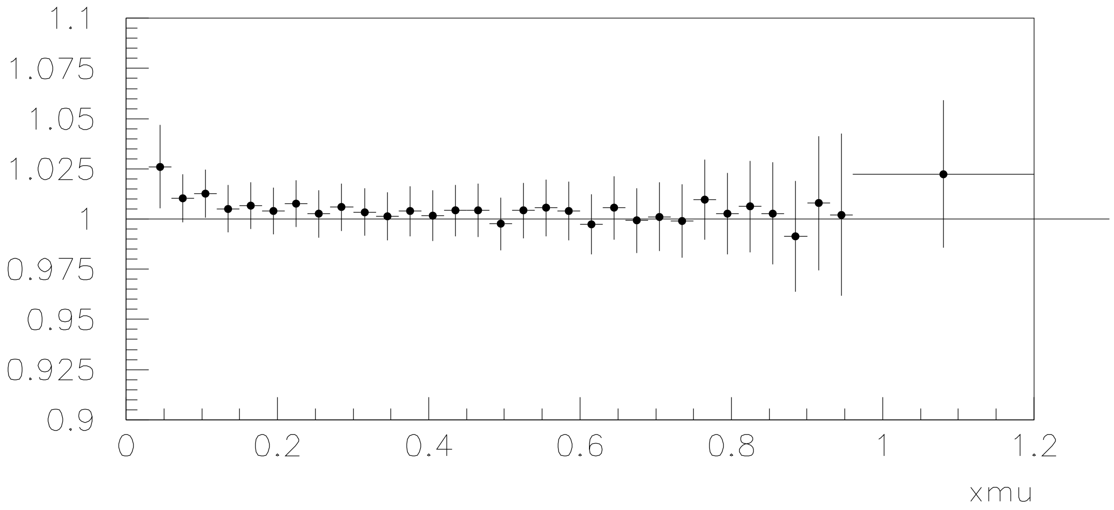

Figure 6.9: The correlation factor, F_{corr}, calculated in bins of x_{μ} for the taupair Monte Carlo.

From the studies detailed in this chapter, we can conclude that using an independently-selected sample of data to gauge the reliability of the Monte Carlo efficiency is highly feasible, particularly in light of the small systematic error that is associated with this method.

Chapter 7

The Branching Ratio.

In this chapter, the results of the selections and the corrections determined in the preceding chapters are used to calculate the muonic branching ratio of the τ. In addition, the year-to-year differences are discussed, the systematic errors are examined in more detail, and the final result is compared with those obtained from other studies.

7.1 Calculation.

The branching ratio is calculated from the following expression:

$$B(\tau \to \mu\nu\bar{\nu}) \equiv \frac{N_{Cand}^{\tau\to\mu\nu\bar{\nu}}}{N_{Cand}^{\tau}} \cdot \frac{(1 - f_{Bkgd}^{\tau\to\mu\nu\bar{\nu}})}{(1 - f_{Bkgd}^{\tau})} \cdot \frac{1}{\epsilon^{\tau\to\mu\nu\bar{\nu}}} \cdot \frac{1}{F_{Bias}^{\tau\to\mu\nu\bar{\nu}}}$$

where the symbols have the following definitions, and their values are given for each year in table 7.1.

- $N_{Cand}^{\tau\to\mu\nu\bar{\nu}}$ is the number of $\tau \to \mu\nu\bar{\nu}$ candidates. Normally the statistical error on this number would constitute the statistical error on the overall branching fraction, but this is not quite the case for this analysis. The division of the overall error between 'statistical' and 'systematic' is discussed in section 7.3.

- N_{Cand}^{τ} is the number of τ candidates. The statistical uncertainty on this large number is negligible.

- $f_{Bkgd}^{\tau\to\mu\nu\bar{\nu}}$ is the estimated background fraction in the $\tau \to \mu\nu\bar{\nu}$ sample from other τ decay modes and non-τ sources (see table 5.2).

	91-92	93	94
N^{τ}_{Cand}	31201	20759	48782
$N^{\tau\to\mu\nu\bar{\nu}}_{Cand}$	4777	3287	7647
$f^{\tau}_{Bkgd}(\%)$	0.597 ± 0.082	1.217 ± 0.176	1.088 ± 0.294
$f^{\tau\to\mu\nu\bar{\nu}}_{Bkgd}(\%)$	2.654 ± 0.144	2.315 ± 0.449	2.481 ± 0.273
$\epsilon^{\tau\to\mu\nu\bar{\nu}}(\%)$	89.54 ± 1.28	90.78 ± 1.56	89.41 ± 1.01
$F^{\tau\to\mu\nu\bar{\nu}}_{Bias}$	0.9800 ± 0.0012	0.9806 ± 0.0012	0.9800 ± 0.0009
B$(\tau \to \mu\nu\bar{\nu})$ (%)	$17.086 \pm 0.215 \pm 0.071$	$17.590 \pm 0.267 \pm 0.091$	$17.637 \pm 0.175 \pm 0.077$

Table 7.1: Number of selected τ and $\tau \to \mu\nu\bar{\nu}$ candidates, background fractions, corrected efficiencies, selection biases and final branching ratio measurements for selected $\tau \to \mu\nu\bar{\nu}$ candidate events in each year. The overall branching ratio error is divided into 'statistical' and 'systematic' contributions. This is discussed further in section 7.3.

- f^{τ}_{Bkgd} is the estimated contamination of non-τ events in the τ pair sample (see table 4.3).

- $\epsilon^{\tau\to\mu\nu\bar{\nu}}$ is the estimated efficiency for selecting $\tau \to \mu\nu\bar{\nu}$ decays within the acceptance (see table 6.2).

- $F^{\tau\to\mu\nu\bar{\nu}}_{Bias}$ is the relative enhancement for detecting $\tau \to \mu\nu\bar{\nu}$ decays with respect to other τ decay modes. The branching ratio (BR) for $\tau \to \mu\nu\bar{\nu}$ is determined from Monte Carlo before and after the $\tau\tau$ selection is made. $F^{\tau\to\mu\nu\bar{\nu}}_{Bias}$ is defined as the ratio BR(selected $\tau\tau$ sample)/BR(generated $\tau\tau$ data) (see table 7.1). $F^{\tau\to\mu\nu\bar{\nu}}_{Bias}$ is calculated for each year's Monte Carlo, and shows excellent consistency. Since the Monte Carlos have different input branching ratios, and the earlier versions have modes that are incorrectly modelled or missing, the bias is assumed to be accurately measured and so the associated error comes purely from statistics.

7.2 Systematic Checks

In order to have confidence in the obtained results and their errors, it was necessary to perform several checks. These are detailed as follows:

- All cuts in the main (muon chamber) selection were varied such that the signal-to-background ratio at the position of the cut in question was one half or twice that at the cut actually used for the analysis. In each case, the shift in measured branching ratio was well-within the systematic error and so no further uncertainty was assigned.

- As described in Section 6.3, the cuts comprising the H_{CAL}/E_{CAL} selection were adjusted to increase background, in order to assess the sensitivity of the efficiency correction to the Monte Carlo modelling. The observed change in branching ratio from doing this was found to be very small and so no extra systematic uncertainty was assigned.

- In determining the correction factors for the tau-pair background, the tails of Monte Carlo distributions were very often used, and so the sensitivity to the placement of the cut was significant. The control samples for each of the backgrounds were adjusted within reasonable limits, and the effect upon the branching ratio was examined. The two-photon acolinearity distributions (see figures 4.5 and 4.6) are very flat and were very stable to changes in the acolinearity cut, the lower bound of which was brought down from $15°$ to $12°$ with very little effect. The mu-pair control sample was adjusted by varying the 'summed energy of tracks and clusters' cut (see figure 4.4), taking ranges 0.55-0.75 and 0.6-0.85. In each case, the corrected mu-pair background was changed very little and so no increase in error was necessary. For the bhabha control sample, the range in the 'sum of clusters' distribution (see figure 4.7) was moved away from the bhabha peak, taking 0.7-0.85 instead of 0.7-0.9. This made the sample more sensitive to the tail of the distribution, which is clearly not well-modelled by Monte Carlo, and the corrected bhabha background, for 1994 data, increased from 0.2% to 0.3% a 2-σ change. However, the overall background increased from $(1.1 \pm 0.3)\%$ to $(1.2 \pm 0.3)\%$, which is well within errors and, since the branching ratio measurement depends only upon the total background, no further error was added.

- The control samples used to determine the correction factors for the $\tau \to \mu\nu\bar{\nu}$ backgrounds were adjusted by varying cuts within reasonable limits, and the correction factors obtained were found to be virtually unchanged so again no extra systematic uncertainty was deemed necessary.

- A further check on the Monte Carlo modelling of hadronic decays can be made by studying the invariant mass distribution (decribed in section 6.1) of candidates passing the muon chamber selection. By doing this, the decays into rho can be directly compared in data and in Monte Carlo, and some indication of the required $\tau \to$ hadrons correction factor can be obtained. Figure 7.1 shows the 1994 distribution, and we see that, although the statistics are low, the data does indeed appear to be above the Monte Carlo level at the 'rho hump' at around 0.8GeV, thus supporting the 30% increase required in the studies of section 5.2.1.

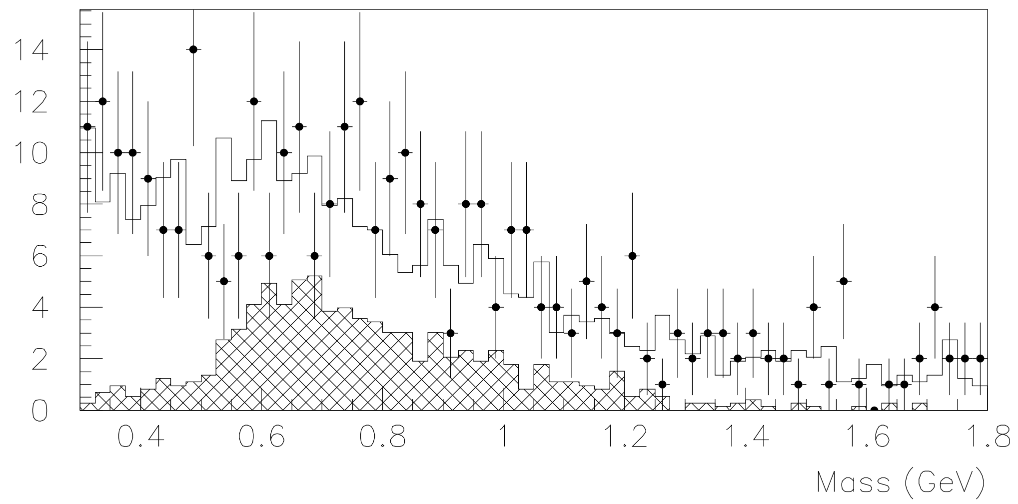

Figure 7.1: The invariant mass distribution for cones passing the muon chamber selection. The data is represented by points with error bars, the muonic tau decays are shown by the unshaded region, and the hadronic tau decays are represented by the shaded histogram.

- The year-by-year nature of this analysis is in itself a subtle test of the methods involved, as different Monte Carlo samples are used in each case. Looking at the final branching ratios (table 7.1), it is clear that the 1993 and 1994 results are in excellent agreement, but the 1992 result is 1.3σ and 1.9σ lower than the 1993 and 1994 results respectively. The main source of this difference lies in the fact that the fraction of τ cones selected as $\tau \to \mu\nu\bar{\nu}$ candidates in 1992 is $\approx 1.4\sigma$ lower than the other years. This ratio of $\tau \to \mu\nu\bar{\nu}$ candidates to τ candidates is:

  $$\begin{gathered} 0.157 \pm 0.002 \qquad \text{for } 1994 \\ 0.158 \pm 0.003 \qquad \text{for } 1993 \\ 0.153 \pm 0.002 \qquad \text{for } 1991-2 \ \ . \end{gathered}$$

  The reason for this difference in the 1991-2 data is not clear, since each year's samples were treated in exactly the same manner using exactly the same code. After considerable detailed study, the source of this discrepancy remains unidentified and so we are forced to conclude that it is simply a statistical effect.

  This 1991-2 data result may be compared directly with that obtained by the previous OPAL analysis [58], which yielded the result

  $$\begin{aligned} B(\tau \to \mu\nu\bar{\nu}) &= (17.48 \pm 0.18 \pm 0.23 \\ &= (17.48 \pm 0.29) \ \ . \end{aligned}$$

  The difference between this and the current result for the same data sample is 1.6σ if just the systematic errors are used. The systematic errors are very different on the two analyses as they are entirely different: they have different smearing applied and have very different Monte Carlo dependence. This analysis is in fact much less dependent on Monte Carlo than was the previous one.

7.3 Discussion of Errors.

Table 7.2 shows the breakdown on the error for each year's branching fraction calculation. The table clearly shows that the statistical uncertainty is now by far the dominant contribution to the final error, but the method of dividing the error deserves some attention. The efficiency correction makes use of the data in such a way that the 'statistical' error on the number of $\tau \rightarrow \mu\nu\bar{\nu}$ candidates selected, and the 'systematic' error from the efficiency correction are correlated. It was decided to define the statistical uncertainty so that it includes the errors on the data statistics used in the efficiency correction, and the efficiency correction error is then composed independently of errors from Monte Carlo statistics. This method means that the quoted errors can then be combined in quadrature to yield the correct overall uncertainty, but the distribution of the error between statistical and systematic has been altered substantially. The contribution to the error from the efficiency correction ('Eff + corr' in table 7.2) no now longer corresponds to the larger efficiency error shown in table 7.1, as the bulk of the error has been subsumed into the statistical uncertainty. Similarly (and somewhat surprisingly) the statistical uncertainty is also slightly smaller than it would have been from using a simple binomial analysis, owing to non-trivial destructive interplay between the data terms of the error expression. The error calculation is shown algebraically in Appendix A, and all the relevant numbers are provided to enable the calculation to be followed through for 1994.

7.4 Final Result

The overall result is obtained by forming a weighted mean of the branching ratios obtained from each year's analysis. To do this, each year's result is weighted by its total error (since the errors are calculated independently for each year) and combined in the usual way. The statistical/systematic split in the final error is obtained by finding the mean statistical error, and subtracting this in quadrature from the mean total error to yield the systematic error. The final result then, is:

$$BR(\tau \rightarrow \mu\nu\bar{\nu}) \quad = \quad (17.453 \pm 0.121 \pm 0.039)\%$$

	Contributions to absolute error		
	1991-2	1993	1994
Stat	0.215	0.268	0.175
Eff + corr	0.018	0.018	0.012
f^{τ}_{Bkgd}	0.014	0.031	0.052
$f^{\tau\rightarrow\mu\nu\bar{\nu}}_{Bkgd}$	0.064	0.081	0.053
$F^{\tau\rightarrow x\nu\bar{\nu}}_{Bias}$	0.021	0.022	0.016
Total	0.227	0.283	0.191

Table 7.2: Breakdown of the errors on the branching ratios for $\tau \rightarrow \mu\nu\bar{\nu}$ for the data from each year.

$$BR(\tau \rightarrow \mu\nu\bar{\nu}) = (17.453 \pm 0.127)\%$$

7.5 Results From Other Experiments.

Figure 7.2 shows how the $\tau \rightarrow \mu\nu\bar{\nu}$ branching ratio from this analysis compares with the results (published or preliminary) obtained by other experiments. The other figures were presented at the 1996 Tau Workshop in September [60] and all are consistent with each other. As can be seen, the precision of the measurement made with this analysis is comparable with the best experimental results.

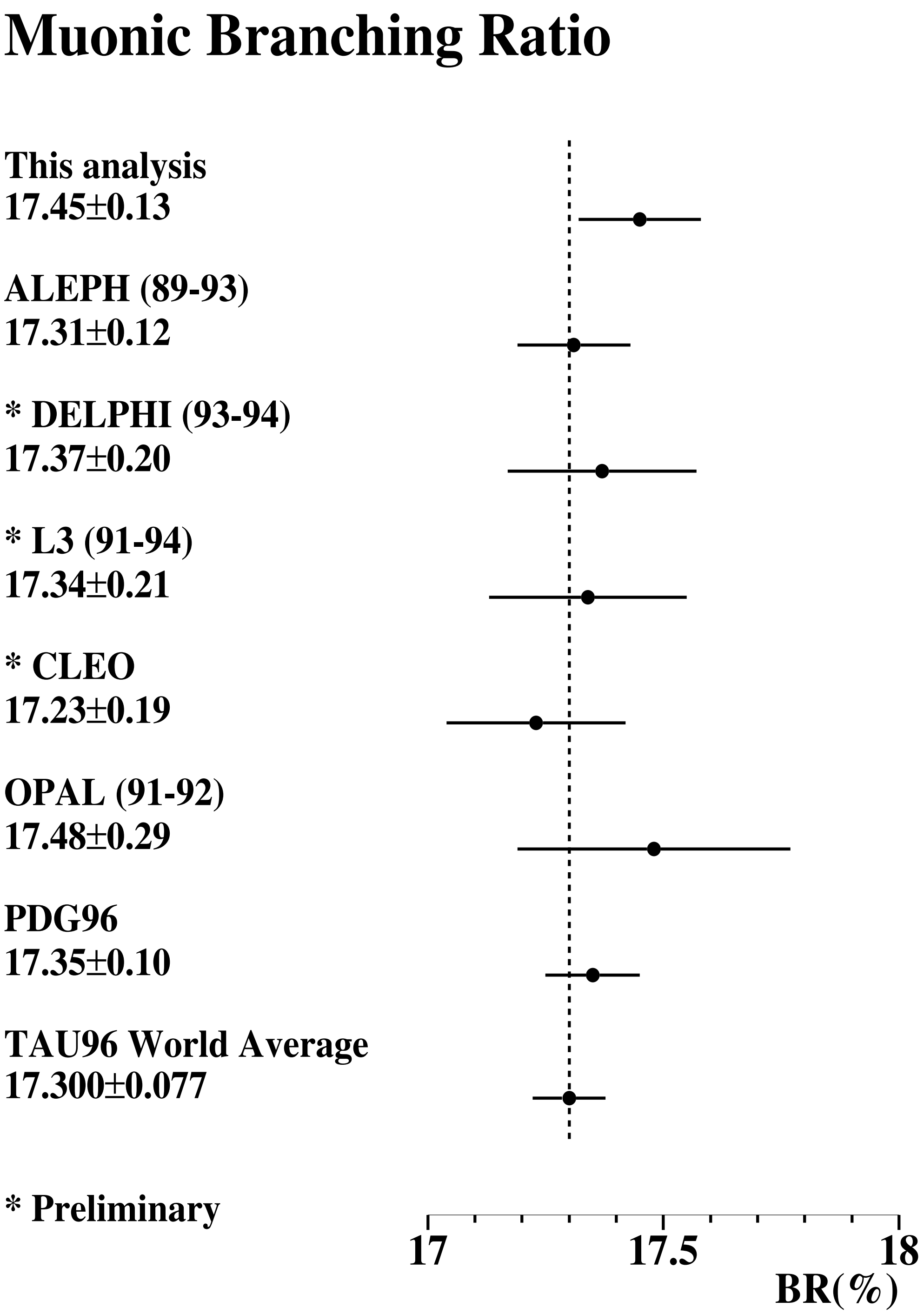

Figure 7.2: Comparison of the result from this analysis with those obtained from other experiments.

Chapter 8

Lepton Universality

In this chapter, the result obtained from the analysis in this thesis is used to perform two universality checks of the weak charged current, and to place an upper limit on the tau neutrino mass.

8.1 Universality Checks

The Standard Model assumes that the coupling strength of the W-boson is of the same magnitude for each lepton. This postulate is easily tested by comparison of the muonic and electronic decay rates of the τ. The partial width for leptonic decays was calculated in Section 1.3, and was given by:

$$\Gamma(\tau \to l\nu\bar{\nu}) = \frac{g_\tau^2 g_l^2}{(8M_W^2)^2}\frac{M_\tau^5}{96\pi^3}F_l(x)F_W F_{rad} \quad . \tag{8.1}$$

If the neutrino mass is taken to be zero, the PDG96 masses are used, and $\alpha(M_\tau)$ (the electromagnetic coupling constant at the τ mass) is taken to be 1/133.3 [61], then we can calculate that

$$\begin{aligned} F_e(x) &= 1.0000 \\ F_\mu(x) &= 0.9726 \\ F_W &= 1.0003 \\ F_{rad} &= 0.9957 \end{aligned}$$

Now, the partial width calculated above can be related to the branching fraction because

$$B(\tau \rightarrow l\nu\bar{\nu}) = \Gamma(\tau \rightarrow l\nu\bar{\nu})/\Gamma(\text{total}) \quad , \tag{8.2}$$

but the total decay width is simply the reciprocal of the tau lifetime, τ_τ, so

$$B(\tau \rightarrow l\nu\bar{\nu}) = \Gamma(\tau \rightarrow l\nu\bar{\nu})\tau_\tau \quad . \tag{8.3}$$

From equation 8.1 we can immediately write that

$$\frac{\Gamma(\tau \rightarrow \mu\nu\bar{\nu})}{\Gamma(\tau \rightarrow e\nu\bar{\nu})} = \frac{g_\mu^2}{g_e^2}\left[\frac{F_\mu(x)}{F_e(x)}\right] \quad , \tag{8.4}$$

and using 8.3 this becomes

$$\frac{B(\tau \rightarrow \mu\nu\bar{\nu})}{B(\tau \rightarrow e\nu\bar{\nu})} = \frac{g_\mu^2}{g_e^2}\left[\frac{F_\mu(x)}{F_e(x)}\right] \quad . \tag{8.5}$$

Substituting the muonic branching ratio obtained from this analysis, and the most recent world average value [60] for the tau decay into electrons, as well as the values of the correction functions calculated before, we obtain:

$$\frac{(17.453 \pm 0.127)\%}{(17.782 \pm 0.071)\%} = \frac{g_\mu^2}{g_e^2}\left[\frac{0.9726}{1.0000}\right] \quad .$$

And so:

$$\left|\frac{g_\mu}{g_e}\right| = 1.0046 \pm 0.0059 \quad ,$$

which is clearly consistent with unity, and so supports the hypothesis of universality.

8.2 Upper Mass limit for m_{ν_τ}

Since the equations in the previous section take account of the final lepton masses (via $F_\mu(x)$), it is possible to rearrange the equations and, assuming universality applies, calculate an upper limit for the tau neutrino mass.

Applying equation 8.1 in the case of muon decay, we can obtain the electronic decay width:

$$\Gamma(\mu \rightarrow e\nu\bar{\nu}) = \frac{g_\mu^2 g_e^2}{(8M_W^2)^2}\frac{M_\mu^5}{96\pi^3}F_e(x)F_W F_{rad} \quad . \tag{8.6}$$

Where all the factors are the same as for the tau decays, but have values calculated using the muon mass rather than the tau mass. Using PDG96 values and taking $\alpha(M_\mu) = 1/137.04$ we obtain:

$$\begin{aligned} F_e(x) &= 0.9998 \\ F_W &= 1.0000 \\ F_{rad} &= 0.9958 \ . \end{aligned}$$

Now, if we take the ratio of the muonic tau decay width to the electronic muon decay width, we have:

$$\frac{\Gamma(\tau \to \mu\nu\bar{\nu})}{\Gamma(\mu \to e\nu\bar{\nu})} = \frac{g_\tau^2}{g_e^2}\left[\frac{M_\tau}{M_\mu}\right]^5 \frac{[F_\mu(x)F_W F_{rad}]^\tau}{[F_e(x)F_W F_{rad}]^\mu} \tag{8.7}$$

which, as before, may be written in terms of branching ratios and lifetimes, and rearranged to give

$$F_\mu(x) = \frac{g_e^2}{g_\tau^2}\frac{\tau_\mu}{\tau_\tau}\left[\frac{M_\mu}{M_\tau}\right]^5 \frac{B(\tau \to \mu\nu\bar{\nu})}{B(\mu \to e\nu\bar{\nu})}\ \frac{[F_e(x)F_W F_{rad}]^\mu}{[F_W F_{rad}]^\tau} \quad . \tag{8.8}$$

Substituting the numbers and assuming universality, we find that

$$F_\mu(x) = 0.9789 \pm 0.0087 \ ,$$

where the error is a combination of the uncertainties on the tau mass, tau lifetime and tau branching fraction into muons, all other sources of error being much smaller. The argument 'x' is defined as M_l^2/M_τ^2 where M_l represents the mass of the *heaviest* of the leptons into which the tau decays. If we assume that the tau neutrino is the heaviest of the decay products, then the following equation can be constructed:

$$(0.9789 \pm 0.0087) = 1 - 8x + 8x^3 - x^4 - 12x^2 ln(x) \tag{8.9}$$

$$(-0.0193 \pm 0.0087) = -8x + 8x^3 - x^4 - 12x^2 ln(x) \ . \tag{8.10}$$

The highest value of x (and hence neutrino mass) is obtained by taking the lowest value of the left-hand side. If we require 95% confidence, then we allow a maximum fluctuation of 2σ, and so form an inequality thus:

$$-0.0385 > -8x + 8x^3 - x^4 - 12x^2 ln(x) \ . \tag{8.11}$$

So $x < 0.00533$ and - using the most accurate value for the tau mass - the upper limit for the tau neutrino mass is

$$m_{\nu_\tau} < 130\mathrm{MeV/c^2} \quad , \quad \text{at 95\% confidence level.}$$

This is a much weaker limit than that obtained from direct searches [62], but it is interesting to make this independent check.

We can go a little further however. By rearranging equation 8.8 we can obtain an expression for the tau lifetime in terms of (amongst other better-measured quantities) the muonic branching fraction and the τ mass:

$$\tau_\tau = \frac{g_e^2}{g_\tau^2}\tau_\mu \left[\frac{M_\mu}{M_\tau}\right]^5 \frac{B(\tau \to \mu\nu\bar{\nu})}{B(\mu \to e\nu\bar{\nu})} \frac{[F_e(x)F_W F_{rad}]^\mu}{[F_\mu(x)F_W F_{rad}]^\tau} \quad . \tag{8.12}$$

This expression may then be plotted as a function of branching ratio, with errors given by the uncertainty on the tau mass, and compared with the measured branching ratio and lifetime values. Figure 8.1 shows the muonic branching ratio found from this analysis, plotted against the lifetime 'function' using PDG96 values. Adopting the usual convention, the branching ratio is shown 'in the massless limit' which means that it is adjusted to the equivalent electronic branching ratio.

Figure 8.2 is a similar plot, presented at the Tau96 workshop [60], that shows the comparison of most recent World averages, along with some Particle Data Group figures from previous years. As we can see, the Standard Model is well-supported by these branching ratio and lifetime mesurements, the results agreeing more and more with the Standard Model as they become more accurate.

8.3 Summary.

In this analysis, a sample of $\tau \to \mu\nu\bar{\nu}$ decays was isolated, using just the tracking and muon chambers of the OPAL detector, from a selected tau-pair sample from data recorded over the period 1991-1994. The backgrounds for the $\tau \to \mu\nu\bar{\nu}$ and tau-pair samples were first estimated from Monte Carlo, and then adjusted with control samples from the data. The efficiency of the muon chamber selection was tested with an independent selection of $\tau \to \mu\nu\bar{\nu}$ decays, obtained using the hadronic

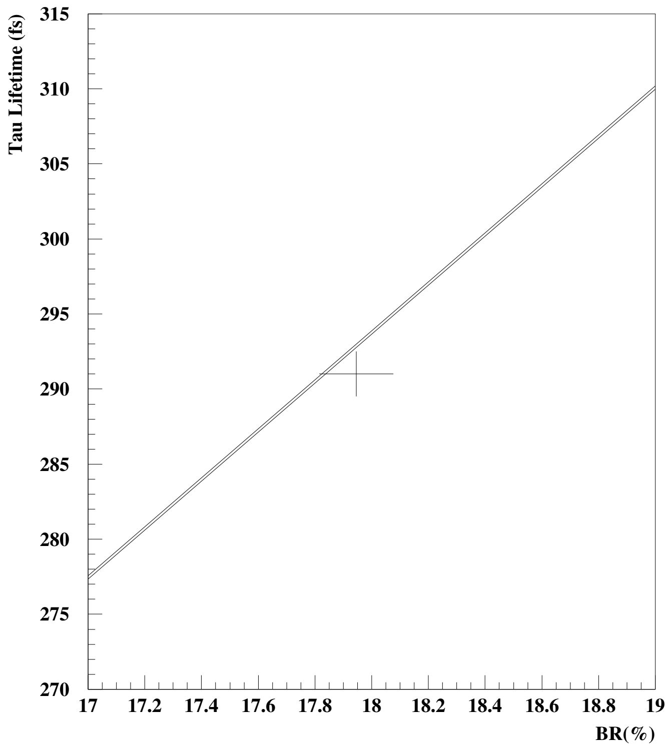

Figure 8.1: The tau lifetime plotted as a function of leptonic branching ratio, with the branching ratio (in the massless limit) from this analysis superimposed.

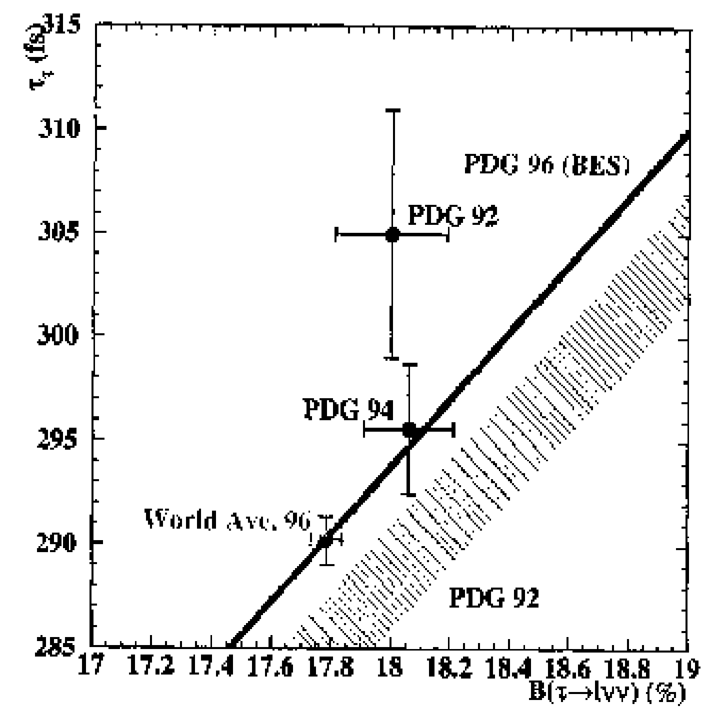

Figure 8.2: The tau lifetime plotted as a function of branching ratio, with several measured branching ratios superimposed (all at massless limit).

and electromagnetic calorimeters. The performance of the main muon selection was measured with this independent sample in data and Monte Carlo, and an efficiency correction factor was derived from the data.

The final branching ratio obtained is:

$$\begin{aligned} B(\tau \to \mu\nu\bar{\nu}) &= (17.453 \pm 0.121 \pm 0.039)\% \\ &= (17.453 \pm 0.127)\% \end{aligned}$$

where the first error derives from data-variables, and the second part of the error from all other sources. This result is consistent and very competitive with the results obtained by other collaborations, having one of the lowest systematic uncertainties. It is also in good agreement with the current World average value of $(17.300 \pm 0.077)\%$.

Various tests of lepton universality have been made. The measured ratio for g_μ/g_e, obtained by comparing the muonic and electronic tau branching fractions, was found to be:

$$\left|\frac{g_\mu}{g_e}\right| = 1.0046 \pm 0.0059 \quad ,$$

which is clearly consistent with unity. Assuming lepton universality, a further calculation was made to determine an upper limit on the mass of the τ neutrino, which was found to be:

$$m_{\nu_\tau} < 130\mathrm{MeV/c^2} \quad , \quad \text{at 95\% confidence level.}$$

Finally, the relation between the tau lifetime, tau mass, and tau branching ratio was tested by plotting the tau lifetime as a function of branching ratio and mass, and checking for consistency with the branching ratio measured in this analysis. The agreement was found to be very good.

These results serve to confirm Standard Model predictions, and are in agreement with other published results.

Appendix A

Error calculation for Efficiency Correction

Correcting the efficiency as described in chapter 6 means that the final expression for the branching ratio has a more complex dependence on the number of events in each of the selected muon samples. The subsequent evaluation of the associated errors proceeds as follows.

The Venn diagram (figure A.1) shows how the sample of taus is divided by the muon chamber selection, and by the H_{CAL} selection. The number of taus in each region is taken as a basis of independent variables, and the expression for the branching ratio is written in terms of these.

The rectangle represents the taupair sample, the solid oval represents the H_{CAL}/E_{CAL} sample, and the dashed oval represents the muon chamber sample. The number of particles in each region of the diagram is given by N_i, where 'i' is 'm' for muon chamber sample only, or 'h' for H_{CAL}/E_{CAL} sample only, or 'b' for both selections simultaneously or 'o' for neither of the selections. Within each region, the total number, N_i, is divided into n_i and b_i, where n_i is the number of Monte Carlo muonic tau decays in the region, and b_i is the number of Monte Carlo background cones. A similar diagram exists for the data, with the total contents of each region labelled N_i^{dat}.

Ignoring bias and background corrections, which are independent of this calcu-

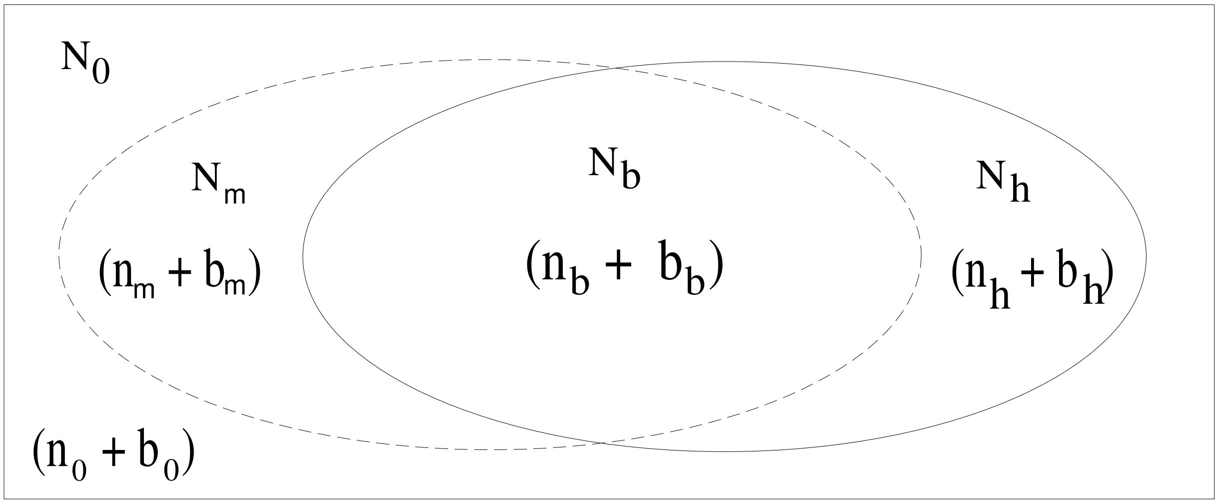

Figure A.1: Venn diagram depicting the selections within the tau sample

lation, the branching ratio is given by:

$$B(\tau \rightarrow \mu\nu\bar{\nu}) \quad \equiv \quad \frac{N_{Cand}^{\tau\rightarrow\mu\nu\bar{\nu}}}{N_{Cand}^{\tau}} \cdot \frac{1}{\epsilon^{\tau\rightarrow\mu\nu\bar{\nu}}} \cdot \frac{1}{C_{eff}}$$

Which, in terms of the independent variables in the Venn diagram is:

$$\begin{aligned}
B(\tau \rightarrow \mu\nu\bar{\nu}) \quad &\equiv \quad \left(\frac{N_m^{dat} + N_b^{dat}}{N_m^{dat} + N_b^{dat} + N_h^{dat} + N_o^{dat}}\right) \cdot \left(\frac{n_m + n_b + n_h + n_o}{n_m + n_b}\right) \cdot \frac{\left[\frac{N_b}{N_b + N_h}\right]}{\left[\frac{N_b^{dat}}{N_b^{dat} + N_h^{dat}}\right]} \\
&\equiv \quad \left[\left(\frac{N_m^{dat} + N_b^{dat}}{N_m^{dat} + N_b^{dat} + N_h^{dat} + N_o^{dat}}\right) \cdot \left(\frac{N_b^{dat} + N_h^{dat}}{N_b^{dat}}\right)\right] \\
&\qquad \times \left[\left(\frac{n_m + n_b + n_h + n_o}{n_m + n_b}\right) \cdot \left(\frac{n_b + b_b}{n_b + b_b + n_h + b_h}\right)\right] \\
&\equiv \quad [D] \times [M]
\end{aligned}$$

where 'D' and 'M' are the data-variable-dependent and Monte Carlo-variable-dependent parts of the expression. The variables comprising 'M' must be split into their component Monte Carlo sources with their corresponding scaling factors:

$$M \quad \equiv \quad \left[\left(\frac{n_m + n_b + n_h + n_o}{n_m + n_b}\right) \cdot \left(\frac{n_b + b_b^t + \alpha b_b^m + \beta b_b^g}{n_b + b_b^t + \alpha b_b^m + \beta b_b^g + n_h + b_h^t + \alpha b_h^m + \beta b_h^g}\right)\right]$$

where b_i^j represents the background from the tau-pair Monte Carlo (j$\equiv$t), or the mu-pair Monte Carlo (j$\equiv$m), or the two-photon muon Monte Carlo (j$\equiv$g). The mu-pairs and the two-photon muons are each scaled to the tau-pair Monte Carlo, and the scaling factors are α and β respectively.

Now, using partial differentiation, the error associated with each of these variables can be calculated and then summed in quadrature to obtain the overall error. Basic calculus tells us that for a general function, F, of *independent* variables, x_i, the total differential [63] is:

$$dF^2 = \sum_i \left(\frac{\delta F}{\delta x_i}\right)^2 \cdot (\delta x_i)^2$$

So, for example, the error associated with the number of Monte Carlo muonic tau decays recognized by the muon selection, n_m, is:

$$\begin{aligned}
\text{squared error associated with } n_m \quad &= \left(\frac{\delta(BR)}{\delta n_m}\right)^2 \cdot (\sqrt{n_m})^2 \\
&= \left(\frac{\delta M}{\delta n_m}\right)^2 \cdot D^2 \cdot n_m \\
&= \left(\frac{M}{n_m + n_b + n_h + n_o} - \frac{M}{n_m + n_b}\right)^2 \cdot D^2 \cdot n_m
\end{aligned}$$

and so on for each of the variables. The value of the variables, differentials and errors for the 1994 data and Monte Carlo are given in tables A.1 and A.2.

The calculation of the error on the correlation factor, F_{corr}, follows a similar pattern, where the expression in terms of the Venn diagram quantities is:

$$F_{corr} = \frac{N_b \cdot (N_m + N_b + N_h + N_o)}{(N_m + N_b) \cdot (N_h + N_b)}$$

and the partial differentials are found and combined in the same way.

Variable	Value
D	0.1741
N_m^{dat}	819
N_h^{dat}	755
N_b^{dat}	6828
N_o^{dat}	40380
M	1.0072
n_m	5376
n_h	4245
n_b	49355
n_o	1221
b_b^t	168
b_b^m	0
b_b^g	0
b_h^t	479
b_h^m	0
b_h^g	0

Table A.1: The variables and their (1994) values used in the calculation of the efficiency correction error.

Variable	Differential of D wrt variable	Squared associated absolute error
N_m^{dat}	1.92×10^{-5}	3.02×10^{-7}
N_h^{dat}	1.94×10^{-5}	2.84×10^{-7}
N_b^{dat}	1.67×10^{-5}	1.89×10^{-6}
N_o^{dat}	3.57×10^{-6}	5.14×10^{-7}
	Sum of squared absolute errors for 'D' =	2.99×10^{-6}
	Fractional error on 'D' =	9.94×10^{-3}
Variable	Differential of M wrt variable	Squared associated absolute error
n_m	-1.67×10^{-6}	1.50×10^{-8}
n_h	-1.89×10^{-6}	1.52×10^{-8}
n_b	4.24×10^{-8}	8.88×10^{-11}
n_o	1.67×10^{-5}	3.42×10^{-7}
b_b^t	1.71×10^{-6}	5.10×10^{-10}
b_b^m	1.66×10^{-6}	0
b_b^g	1.51×10^{-6}	0
b_h^t	1.86×10^{-5}	1.08×10^{-7}
b_h^m	1.81×10^{-5}	0
b_h^g	1.64×10^{-5}	0
	Sum of squared absolute errors for 'M' =	4.81×10^{-7}
	Fractional error on 'M' =	6.88×10^{-4}
	Overall fractional error (D and M) =	9.96×10^{-3}

Table A.2: The variables and their (1994) derivative values used in the calculation of the efficiency correction error.

Appendix B

Control Sample Compositions Used For Checking Tau-pair Background Levels.

Event sample	Number of events
	1991-92
MC $e^+e^- \to \mu^+\mu^-$	48.6 $\pm$ 3.6
MC $e^+e^- \to \tau^+\tau^-$	104.8 $\pm$ 5.3
All Data	150 $\pm$ 12.2
DATA $e^+e^- \to \mu^+\mu^-$	45.2 $\pm$ 13.3
Ratio $\frac{DATA(e^+e^-\to\mu^+\mu^-)}{MC(e^+e^-\to\mu^+\mu^-)}$	0.930$\pm$0.283
Event sample	Number of events
	1993
MC $e^+e^- \to \mu^+\mu^-$	23.8 $\pm$ 2.0
MC $e^+e^- \to (e^+e^-)\mu^+\mu^-$	0.2 $\pm$ 0.1
MC $e^+e^- \to \tau^+\tau^-$	48.5 $\pm$ 2.4
All Data	111 $\pm$ 10.5
DATA $e^+e^- \to \mu^+\mu^-$	62.3 $\pm$ 10.8
Ratio $\frac{DATA(e^+e^-\to\mu^+\mu^-)}{MC(e^+e^-\to\mu^+\mu^-)}$	2.615$\pm$0.505
Event sample	Number of events
	1994
MC $e^+e^- \to \mu^+\mu^-$	69.7 $\pm$ 3.1
MC $e^+e^- \to (e^+e^-)\mu^+\mu^-$	0.4 $\pm$ 0.2
MC $e^+e^- \to \tau^+\tau^-$	119.5 $\pm$ 4.0
All Data	235 $\pm$ 15.3
DATA $e^+e^- \to \mu^+\mu^-$	115.1 $\pm$ 15.9
Ratio $\frac{DATA(e^+e^-\to\mu^+\mu^-)}{MC(e^+e^-\to\mu^+\mu^-)}$	1.651$\pm$0.239

Table B.1: Shown for each year is the mupair control sample in data and in Monte Carlo.

Event sample	Number of events
	1991-92
MC $e^+e^- \rightarrow q\bar{q}$	64.9 $\pm$ 6.1
MC $e^+e^- \rightarrow \tau^+\tau^-$	78.3 $\pm$ 4.6
All Data	168 $\pm$ 13.0
DATA $e^+e^- \rightarrow q\bar{q}$	89.7 $\pm$ 13.7
Ratio $\frac{DATA(e^+e^- \rightarrow q\bar{q})}{MC(e^+e^- \rightarrow q\bar{q})}$	1.381$\pm$0.248
	1993
MC $e^+e^- \rightarrow q\bar{q}$	45.6 $\pm$ 5.7
MC $e^+e^- \rightarrow e^+e^-$	0.3 $\pm$ 0.3
MC $e^+e^- \rightarrow \tau^+\tau^-$	39.8 $\pm$ 2.1
All Data	112 $\pm$ 10.6
DATA $e^+e^- \rightarrow q\bar{q}$	71.9 $\pm$ 10.8
Ratio $\frac{DATA(e^+e^- \rightarrow q\bar{q})}{MC(e^+e^- \rightarrow q\bar{q})}$	1.579$\pm$0.309
	1994
MC $e^+e^- \rightarrow q\bar{q}$	420.3 $\pm$ 18.7
MC $e^+e^- \rightarrow e^+e^-$	0.3 $\pm$ 0.3
MC $e^+e^- \rightarrow \tau^+\tau^-$	97.3 $\pm$ 3.6
All Data	303 $\pm$ 17.4
DATA $e^+e^- \rightarrow q\bar{q}$	205.4 $\pm$ 17.8
Ratio $\frac{DATA(e^+e^- \rightarrow q\bar{q})}{MC(e^+e^- \rightarrow q\bar{q})}$	0.489$\pm$0.048

Table B.2: Shown for each year is the multihadron control sample in data and in Monte Carlo.

Event sample	Number of events
	1991-92
MC $e^+e^- \rightarrow (e^+e^-)\mu^+\mu^-$	135.6 ± 9.4
DATA $e^+e^- \rightarrow (e^+e^-)\mu^+\mu^-$	157 ± 12.5
Ratio $\frac{DATA(e^+e^- \rightarrow (e^+e^-)\mu^+\mu^-)}{MC(e^+e^- \rightarrow (e^+e^-)\mu^+\mu^-)}$	1.158 ± 0.122
	1993
MC $e^+e^- \rightarrow (e^+e^-)\mu^+\mu^-$	61.8 ± 1.7
DATA $e^+e^- \rightarrow (e^+e^-)\mu^+\mu^-$	80 ± 8.9
Ratio $\frac{DATA(e^+e^- \rightarrow (e^+e^-)\mu^+\mu^-)}{MC(e^+e^- \rightarrow (e^+e^-)\mu^+\mu^-)}$	1.294 ± 0.149
	1994
MC $e^+e^- \rightarrow (e^+e^-)\mu^+\mu^-$	177.4 ± 4.7
DATA $e^+e^- \rightarrow (e^+e^-)\mu^+\mu^-$	222 ± 14.9
Ratio $\frac{DATA(e^+e^- \rightarrow (e^+e^-)\mu^+\mu^-)}{MC(e^+e^- \rightarrow (e^+e^-)\mu^+\mu^-)}$	1.251 ± 0.090

Table B.3: Shown for each year is the two-photon muon control sample in data and in Monte Carlo.

Event sample	Number of events
	1991-92
MC $e^+e^- \rightarrow (e^+e^-)e^+e^-$	195.0 ± 12.1
All Data	218 ± 14.8
DATA $e^+e^- \rightarrow (e^+e^-)e^+e^-$	218 ± 14.8
Ratio $\frac{DATA(e^+e^- \rightarrow (e^+e^-)e^+e^-)}{MC(e^+e^- \rightarrow (e^+e^-)e^+e^-)}$	1.118 ± 0.103
	1993
MC $e^+e^- \rightarrow (e^+e^-)e^+e^-$	116.0 ± 2.5
MC $e^+e^- \rightarrow (e^+e^-)\mu^+\mu^-$	0.1 ± 0.1
All Data	155 ± 12.4
DATA $e^+e^- \rightarrow (e^+e^-)e^+e^-$	154.9 ± 12.5
Ratio $\frac{DATA(e^+e^- \rightarrow (e^+e^-)e^+e^-)}{MC(e^+e^- \rightarrow (e^+e^-)e^+e^-)}$	1.335 ± 0.168
	1994
MC $e^+e^- \rightarrow (e^+e^-)e^+e^-$	370.7 ± 7.1
All Data	344 ± 18.5
DATA $e^+e^- \rightarrow (e^+e^-)e^+e^-$	344 ± 18.5
Ratio $\frac{DATA(e^+e^- \rightarrow (e^+e^-)e^+e^-)}{MC(e^+e^- \rightarrow (e^+e^-)e^+e^-)}$	0.928 ± 0.053

Table B.4: Shown for each year is the two-photon electron control sample in data and in Monte Carlo.

Event sample	Number of events
	1991-92
MC $e^+e^- \to e^+e^-$	407.4 $\pm$ 24.7
MC $e^+e^- \to \tau^+\tau^-$	17.9 $\pm$ 2.2
All Data	670 $\pm$ 25.9
DATA $e^+e^- \to e^+e^-$	652.1 $\pm$ 26.0
Ratio $\frac{DATA(e^+e^- \to e^+e^-)}{MC(e^+e^- \to e^+e^-)}$	1.600$\pm$0.116
Event sample	Number of events
	1993
MC $e^+e^- \to e^+e^-$	248.7 $\pm$ 7.8
MC $e^+e^- \to \tau^+\tau^-$	9.3 $\pm$ 1.0
All Data	525 $\pm$ 22.9
DATA $e^+e^- \to e^+e^-$	515.7 $\pm$ 22.9
Ratio $\frac{DATA(e^+e^- \to e^+e^-)}{MC(e^+e^- \to e^+e^-)}$	2.074$\pm$0.537
Event sample	Number of events
	1994
MC $e^+e^- \to e^+e^-$	1441.97 $\pm$ 19.8
MC $e^+e^- \to (e^+e^-)e^+e^-$	0.5 $\pm$ 0.3
MC $e^+e^- \to \tau^+\tau^-$	16.1 $\pm$ 1.5
All Data	1313 $\pm$ 36.2
DATA $e^+e^- \to e^+e^-$	1296.5 $\pm$ 36.3
Ratio $\frac{DATA(e^+e^- \to e^+e^-)}{MC(e^+e^- \to e^+e^-)}$	0.899$\pm$0.051

Table B.5: Shown for each year is the bhabha control sample in data and in Monte Carlo.

Bibliography

[1] D. Rigby, *'Measurement of the Muonic Branching Ratio of the tau'*, OPAL Technical Note, TN-431 (1996).

[2] F. Halzen and A.D. Martin, *Quarks and Leptons: An Introductory Course in Modern Particle Physics*, John Wiley and Sons, 1984.
D.H. Perkins, *Introduction to High Energy Physics*, Addison-Wesley Publishing Company, Third Edition 1987.
I.J.R. Aitchison and A.J.G. Hey, *'Gauge Theories in Particle Physics'* Second Edition, Cambridge University Press (1991).

[3] CDF Collaboration, F. Abe et all, Phys. Rev. Lett. **74** (1995), 2626.
D0 Collaboration, S. Abachi et al., Phys. Rev. Lett. **74** (1995), 2632.

[4] L. Wolfenstein, Phys. Rev. Lett.**51** (1984), 1945.

[5] R.P. Feynman, *'The Feynman Lectures on Physics, Volume 2'*, Addison Wesley (1966).

[6] G. 't Hooft, Nucl. Phys. **B33** (1971), 173;
Nucl. Phys. **B35** (1971), 167;
Utrecht preprint THU-92/25 (1992).

[7] R.P. Feynman, *'Quantum Electrodynamics'*, Benjamin (1961).

[8] S.L. Glashow, Nucl. Phys. **22** (1961), 579;

[9] See *'Elementary Particle Theory'*, ed. N. Svartholm, Almqvist and Wikel (1968), 361.
S. Weinberg, Phys. Rev. Lett. **19** (1967), 1264.

[10] T.D. Lee and C.N. Yang, Phys. Rev. **98** (1955), 1501.
C.S. Wu et al, Phys. Rev. **105** (1957), 1413.

[11] P.W. Higgs, Phys. Lett. **12** (1964), 132;
Phys. Rev. Lett. **13** (1964), 508;
Phys. Rev. **145** (1966), 1156;

[12] LEP Electroweak Working Group, P. Antilogus et al, LEPEWWG/95-02 (1995); OPAL Technical Note TN-312.

[13] ATLAS Collaboration, Letter of Intent CERN-LHCC/92-4 (1992);
Technical Proposal CERN-LHCC/94-43 (1994).
CMS Collaboration, Letter of Intent CERN-LHCC/92-3 (1992);
Technical Proposal CERN-LHCC/94-38 (1994).

[14] M.L. Perl, *The Discovery of the Tau Lepton*, **SLAC-PUB-6584** (1994).

[15] M.L. Perl *et al.* (MARK I), Phys. Rev. Lett. **35** (1975) 1489.

[16] E531 Collaboration, Ushida N, et al. Phys. Rev. Lett. **57** (1986) 2897

[17] Y. Tsai, Phys. Rev. **D4** (1971) 2821.

[18] BES Collaboration, J.Z. Bai et al., Phys. Rev. Lett. **69** (1992) 3021
BES Collaboration, *'Final Result on the Mass of the τ lepton'* presented at the 27^{th} International Conference on High-Energy Physics in Glasgow, 1994.
BES Collaboration, *'Tau Lepton Experiment at BES Detector.'* presented at the Tau Workshop, Montreux, 1994.

[19] ARGUS Collaboration, H. Albrecht et al., Phys. Lett. **B 292** (1992) 221.

[20] CLEO Collaboration, R. Balest et al., Phys. Rev. **D 47** (1993) R3671.

[21] J.A. Jaros et al., MARK II Collaboration, Phys. Rev. Lett. **51** (1983) 955.

[22] Particle Data Group, *Review of Particle Physics*, **Phys. Rev. D54** (1996), 1.

[23] OPAL Collaboration, P. Acton et al. *'Measurement of the Tau Lifetime'* CERN-PPE/93-09 Zeit. fuer Physik C59 (1993) 183-194

[24] K. Abe et al., SLD Collaboration, *'Measurement of the Tau Lifetime'*, SLAC-PUB-95-6767 (1995)

[25] OPAL Collaboration, R. Akers *et al.* *'Updated Measurement of the Tau Lifetime'*, CERN-PPE/94-129 Physics Letters B338 (1994) 497-506

[26] S. Myers and E. Picasso, *The design, construction and commissioning of the CERN Large Electron-Positron collider*, Contempory Physics, volume 31, number 6, (1990).

[27] The LEP Collaborations, ALEPH, DELPHI, L3, OPAL and the LEP Electroweak Working Group, **CERN-PPE/94-187**, (1994).

[28] G. Altarelli et al., *'Interim Report on the Physics Motivations for an Energy Upgrade of LEP2'*, CERN-TH/95-151 (1995);
CERN-PPE/95-78 (1995)

[29] D. Decamp *et al.* (ALEPH), Nucl. Instr. and Meth. **A294** (1990) 121.

[30] P. Aarnio *et al.* (DELPHI), Nucl. Instr. and Meth. **A303** (1991) 233.

[31] B. Adeva *et al.* (L3), Nucl. Instr. and Meth. **A289** (1990) 35.

[32] K. Ahmet *et al.* (OPAL), Nucl. Instr. and Meth. **A305** (1991) 275.

[33] P.P. Allport *et al.* (OPAL), Nucl. Instr. and Meth. **A324** (1993) 34.

[34] J.R. Carter et al., Nucl. Instr. and Meth. **A286** (1990) 99.
J.M. Roney et al., Nucl. Instr. and Meth. **A279** (1989) 236.

[35] R.D. Heuer and A. Wagner, Nucl. Instr. and Meth. **A265** (1988) 11.
H.M. Fischer et al., Nucl. Instr. and Meth. **A252** (1986) 492.

[36] H. Mes et al., Nucl. Instr. and Meth. **A265** (1988) 445.

[37] A. Ji-Gang et al., Nucl. Instr. and Meth. **A267** (1988) 386.

[38] P. Mattig, *'Photon Energy Resolution in the Lead Glass Calorimeters'*, OPAL Technical Note, TN-324 (1995).

[39] A. H. Ball et al., IEEE Trans. Nucl. Sci. **37** (1990).

[40] J. Allison et al., Nucl. Instr. and Meth. **A236** (1985) 284.

[41] G.T.J. Arnison et al., Nucl. Instr. and Meth. **A294** (1990) 431.

[42] OPAL Collaboration, K. Ahmet et al., Nucl. Instr. and Meth. **A305** (1991) 275.

[43] D.C. Imrie et. al., Nucl. Instr. and Meth. **A238** (1989) 515.

[44] M. Mannelli, OPAL Physics Note **PN142** (1994)

[45] M. Arignon *et al.* (OPAL), Nucl. Instr. and Meth. **A313** (1992) 103.

[46] M. Arignon *et al.* (OPAL), Nucl. Instr. and Meth. **A333** (1993) 330.

[47] J. Baines et. al., Nucl. Instr. and Meth. **A325** (1993) 271.

[48] D. Charlton, et al., Nucl. Instr. and Meth. **A325** (1993) 129.

[49] C. Hawkes et al., *'ROPE User Guide (version 4.09)'*, OPAL Offline Note OFFL-0487 (1995).

[50] D. Ward and J. Banks, *'A GROPE Primer (latest revisions for GR202)'*, OPAL Offline Note (1995)

[51] J. Allison *et al.*, Nucl. Instr. and Meth. **A317** (1992) 47.

[52] J. Allison *et al.*, Nucl. Instr. and Meth. **A294** (1990) 431.

[53] T. Sjostrand, Comp. Phys. Comm. **39** (1986) 347; JETSET

[54] S. Jadach, B.F.L. Ward, and Z. Was, Comp. Phys. Comm. **66** (1991) 276;KO-RALZ

[55] S. Jadach, J.H. Kuhn, and Z. Was, **CERN-TH-5856/90** (1990) ;TAUOLA

[56] The Tau Platform (TP1.02), OPAL writeup.

[57] OPAL Collaboration, R. Akers *et al.* Physics Note **PN142** (1995).

[58] OPAL Collaboration, R. Akers *et al.* Physics Note **PN154** (1994).

[59] OPAL Collaboration, R. Akers *et al.* Physics Note **PN172** (1995).

[60] The Tau 1996 Workshop in Colorado.

[61] W. Marciano, Ann. Rev. Nucl. Part. Sci. **41** (1991) 469.

[62] ARGUS Collaboration, H. Albrecht et al., Phys. Lett. *B 202* (1988) 149.
CLEO Collaboration, D. Cinabro et al., Phys. Rev. Lett. *70* (1993) R3700.
OPAL Collaboration, R. Akers *et al.* Z. Phys. **C 65** (1995) 183.
ALEPH Collaboration, D. Buskulic *et al.* *'An Upper Limit for the τ Neutrino mass.'*, CERN-PPE/95-03.

[63] R. J. Barlow, *'A Guide to the Use of Statistical Methods in the Physical Sciences'*, Wiley, 1989.